

# Ionogel Electrolytes through Sol-Gel Processing

A dissertation submitted by

Ariel I. Horowitz

in partial fulfillment of the requirements for the degree of

Doctor of Philosophy

in

Chemical and Biological Engineering

Tufts University

May 2015

Adviser: Matthew J. Panzer

Copyright (2015) by Ariel I. Horowitz

## Abstract

Electrical energy needs have intensified due to the ubiquity of personal electronics, the decarbonization of energy services through electrification, and the use of intermittent renewable energy sources. Despite developments in mechanical and thermal methods, electrochemical technologies are the most convenient and effective means of storing electrical energy. These technologies include both electrochemical cells, commonly called batteries, and electrochemical double-layer capacitors, or “supercapacitors”, which store energy electrostatically.

Both device types require an ion-conducting electrolyte. Current devices use solutions of complex salts in organic solvents, leading to both toxicity and flammability concerns. These drawbacks can be avoided by replacing conventional electrolytes with room-temperature molten salts, known as ionic liquids (ILs). ILs are non-volatile, non-flammable, and offer high conductivity and good electrochemical stability. Device mass can be reduced by combining ILs with a solid scaffold material to form an “ionogel,” further improving performance metrics.

In this work, sol-gel chemistry is explored as a means of forming ionogel electrolytes. Sol-gel chemistry is a solution-based, industrially-relevant, well-studied technique by which solids such as silica can be formed *in situ*. Previous works used a simple acid-catalyzed sol-gel reaction to create brittle, glassy ionogels. Here, both the range of products that can be accomplished through sol-

gel processing and the understanding of interactions between ILs and the sol-gel reaction network are greatly expanded.

This work introduces novel ionogel materials, including soft and compliant silica-supported ionogels and PDMS-supported ionogels. The impacts of the reactive formulation, IL identity, and casting time are detailed. It is demonstrated that variations in formulation can lead to rapid gelation and open pore structures in the silica scaffold or slow gelation and more dense silica morphologies. The IL identity is shown to have an impact on the apparent strength of the acid catalyst, leading to significant shifts in gelation time. Delayed casting is proven to be an optimal technique for avoiding pore blockage when combining ionogels with high surface area electrodes for supercapacitor applications. Finally, a simple recycling process is proposed, establishing that ILs can be easily reclaimed from silica-supported ionogels and reused, thereby validating the reputation of ILs as “green” materials.

## **Acknowledgements**

I am extremely grateful that I had the good fortune to work with Professor Matthew J. Panzer, one of the most generous mentors I have ever heard of or personally encountered. The creative freedom allowed to me, supportive guidance provided to me, and unwavering enthusiasm shown to me by Professor Panzer were invaluable. I will be forever proud to have been a member of GENE Lab, and thankful for the experience.

As my thesis committee, Professor Daniel Ryder, Dr. David Ofer, and Professor William Moomaw have all provided kind and constructive feedback, which I greatly appreciated throughout my thesis work. In particular, Professor Moomaw has served as a second adviser to me, and has truly expanded my intellectual horizons. I consider my opportunity to work with him as one of the most fortuitous events of my life.

My colleagues in GENE (Green Energy and Nanostructured Electronics) Lab have been a wonderful source of inspiration and companionship. I am very thankful to be able to call Anna Osherov, Changqiong Zhu, and Adam Visentin friends. I have also worked with a number of exceptional undergraduates over the course of my research. Although all showed growth and dedication during their tenures in GENE Lab, I am particularly proud to have been given the opportunity to mentor Yushi Wang, Kenny Westerman, Nick Larew, and Paola Arias, all of whom made important and impressive contributions to this research.

Coming from a nontraditional background, I am grateful to have been welcomed in the Department of Chemical and Biological Engineering. The

department faculty has been extremely supportive. I am especially grateful to Professors Stephanopoulos and Asatekin for their interest in my progress and helping hands along the way. I must also express my immense appreciation for Erin Quigley Piazza, Emily Edwards, Margaret DeChiaro, and Beth Ann Frasso, without whose assistance and friendship my thesis would have been a much bleaker experience.

Without the support of my family, and without their dreams for me, I would have never considered such an undertaking, let alone been able to complete it. I am more proud than I can say to become the fourth Dr. Horowitz.

My feelings of gratitude for the love, patience, steadfast companionship, unshakeable belief, ready smile, musical stylings, and unparalleled comic-drawing skills of my fiancé Garth Griffin are overwhelming and indescribable. I wake up every day lucky to be building a life together with him.

Thank you,

Ariel

April 2015

Tufts University

## Table of Contents

Abstract .....	ii
Acknowledgements .....	iv
Table of Contents .....	vi
List of Figures .....	x
List of Tables .....	xiii
 <b>Chapter 1: Introduction</b> .....	 1
1.1 Opening thoughts .....	1
1.2 Supercapacitors as a Solution to Technological Limitations in Electrochemical Energy Storage .....	2
1.3 Ionogels as a Solution to Materials Challenges for Electrochemical Energy Storage .....	8
1.4 Preview of Things to Come .....	14
1.5 References .....	17
 <b>Chapter 2: Major Experimental Tools and Techniques</b> .....	 27
2.1 Introduction .....	27
2.2 Chemical Characterization .....	27
2.2.1 Thermogravimetric Analysis .....	28
2.2.2 Differential Scanning Calorimetry .....	35
2.2.3 Fourier Transform Infrared Spectroscopy .....	35
2.2.4 Karl Fischer Titration .....	37
2.3 Mechanical Characterization .....	38
2.3.1 Stress/Strain Testing .....	38
2.3.2 Dynamic Mechanical Analysis .....	43
2.4 Electrical Testing .....	43
2.4.1 Electrical Impedance Spectroscopy .....	44
2.4.2 Cyclic Voltammetry .....	48
2.4.3 Charge-Discharge .....	51
2.5 References .....	54
 <b>Chapter 3: High-performance, mechanically compliant silica-based ionogels for electrical energy storage applications</b> .....	 56
3.1 Introduction .....	56
3.2 Results and Discussion .....	58
3.2.1 Ionogel Physical Properties .....	58
3.2.2 Ionogel Electrical Properties .....	69
3.3 Conclusion .....	77
3.4 Experimental Materials and Methods .....	78

3.4.1 Ionogel Preparation.....	78
3.4.2 Physical Characterization.....	79
3.4.3 Electrical Characterization.....	79
3.5 References.....	81
 <b>Chapter 4: The Variation of Silica-Supported Ionogel Properties with</b>	
Reactive Formulation.....	86
4.1 Introduction.....	86
4.2 Results and Discussion.....	87
4.2.1 Variations in Gelation Time and Scaffold Content with Formulation.....	87
4.2.2 Variations in Mechanical Characteristics and Scaffold Morphology with Gelation Time.....	92
4.3 Conclusion.....	96
4.4 Experimental Materials and Methods.....	97
4.4.1 Materials.....	97
4.4.2 Gelation Time Determination.....	97
4.4.3 Thermogravimetric Analysis.....	97
4.4.4 Mechanical Analysis.....	98
4.5 References.....	99
 <b>Chapter 5: Spectroscopic Determination of Relative Brønsted Acidity as</b>	
a Predictor of Reactivity in Aprotic Ionic Liquids.....	100
5.1 Introduction.....	100
5.2 Results and Discussion.....	102
5.2.1 FTIR Titration Approach.....	102
5.2.2 Reaction Results.....	108
5.3 Conclusion.....	114
5.4 Experimental Materials and Methods.....	115
5.4.1 Materials.....	115
5.4.2 FTIR-enabled Acid Titration of Pyridine-in-IL Solutions.....	115
5.4.3 Ionogel Preparation and Determination of Gel Times.....	116
5.4.4 Copper Etching.....	117
5.5 References.....	118
 <b>Chapter 6: The Impact of Ionogel Casting Time on Silica Morphology</b>	
and Supercapacitor Device Performance.....	123
6.1 Introduction.....	123
6.2 Results and Discussion.....	126

6.2.1 The Influence of Casting Time and Atmosphere on Silica Morphology.....	126
6.2.2 The Impact of Casting Time on Device Performance.....	130
6.3 Conclusion.....	144
6.4 Experimental Materials and Methods.....	145
6.4.1 Materials.....	145
6.4.2 Casting of Ionogel Films.....	145
6.4.3 Thermogravimetric Analysis.....	146
6.4.4 Preparation of Graphene Electrodes.....	146
6.4.5 Device Fabrication.....	147
6.4.6 Device Testing.....	148
6.5 References.....	149

## **Chapter 7: Reclamation and Reuse of Ionic Liquids from Silica-Based**

Ionogels Using Spontaneous Water-Driven Separation.....	154
7.1 Introduction.....	154
7.2 Results and Discussion.....	158
7.2.1 Process Considerations.....	158
7.2.2 Reclamation Effectiveness.....	165
7.3.3 Properties of Reclaimed ILs.....	171
7.3 Conclusion.....	174
7.4 Experimental Materials and Methods.....	175
7.4.1 Ionogel Preparation.....	175
7.4.2 IL Reclamation.....	176
7.4.3 Analysis.....	177
7.5 References.....	178

## **Chapter 8: Poly(dimethylsiloxane)-Supported Ionogels with High Ionic**

Liquid Loading.....	186
8.1 Introduction.....	186
8.2 Results and Discussion.....	188
8.2.1 Synthetic Approach and Ionogel Structure.....	188
8.2.2 Properties of PDMS-Supported Ionogels.....	191
8.3 Conclusion.....	197
8.4 Experimental Materials and Methods.....	198
8.4.1 Chemicals.....	198
8.4.2 Ionogel Preparation.....	198
8.4.3 Lithium-Bearing Ionogel Preparation.....	199
8.4.4 Preparation of Pure PDMS.....	199
8.4.5 Thermal Testing.....	200



8.4.6 Mechanical Testing.....	200
8.4.7 Electrical Testing.....	201
8.4.8 FTIR Testing.....	202
8.4.9 Water Stability Testing.....	202
8.4.10 Gel Permeation Chromatography.....	202
8.4.11 Hexane Absorption.....	203
8.5 References.....	204
<b>Chapter 9: Conclusions and Future Directions.....</b>	<b>209</b>
9.1 Future Directions.....	209
9.1.1 Hybrid Chemistries.....	209
9.1.2 Recycling in Other Ionogel Systems.....	210
9.1.3 High-Performance Devices with Ionogels.....	212
9.1.4 High-Performance Supercapacitors.....	212
9.1.5 Batteries.....	217
9.2 Final Conclusions.....	218
9.3 References.....	221
<b>Appendix A: Supplementary Information Concerning Chapter 3.....</b>	<b>227</b>
<b>Appendix B: Supplementary Information Concerning Chapter 5.....</b>	<b>231</b>
B1 Supplementary Discussion Regarding Acids in Non-Aqueous Media.....	231
B2 References.....	239
<b>Appendix C: Supplementary Information Concerning Chapter 7.....</b>	<b>241</b>
<b>Appendix D: Supplementary Information Concerning Chapter 8.....</b>	<b>246</b>
D1 Determination of the Extent of PDMS Scaffold Crosslinking.....	246
D2 Influence of Formulation Changes on PDMS Ionogels.....	252
D3 Lithium-Containing Ionogels.....	256
D3 References.....	257
<b>Appendix E: How to Capture Stress/Strain Data with the DMA.....</b>	<b>259</b>

## List of Figures

1.1	Ragone plot.....	4
1.2	Capacitor and supercapacitor schematics.....	6
1.3	Ionic liquid structures.....	10
2.1	Photo of thermogravimetric analysis instrumentation.....	29
2.2	Example thermogravimetric data.....	31
2.3	Photo of dynamic mechanical analysis instrumentation.....	40
2.4	Example dynamic mechanical analysis data.....	42
2.5	Example electrical impedance spectroscopy data.....	47
2.6	Example cyclic voltammetry data.....	50
2.7	Example charge-discharge data.....	52
3.1	Ternary diagram of FA/TMOS/IL system.....	59
3.2	Photos of brittle and compliant ionogels.....	64
3.3	Thermogravimetric data for brittle and compliant ionogels, as well as for ionogels made with intermediate formulations.....	66
3.4	SEM images of scaffold morphologies for brittle and compliant ionogels.....	68
3.5	Impedance data for brittle and compliant ionogels as compared with the neat IL.....	74
3.6	Cyclic voltammograms for compliant ionogels over a range of scan rates and as compared to the neat IL.....	76
4.1	Scatter plot of all tested formulations and their scaffold contents.....	89
4.2	Scatter plot of all formulations which gel under 12 hours and their gelation times.....	91
4.3	SEM images of scaffold morphology for two ionogels with different gelation times and similar scaffold contents.....	95
5.1	Overview of relevant FTIR region and position of free pyridine peak.....	104
5.2	Example titration data.....	107
5.3	Photos showing differences in ionogels and copper etching using different ILs.....	109
6.1	SEMs comparing the morphologies of films cast at different times and the bulk ionogel, prepared both in ambient and dry nitrogen atmospheres.....	129
6.2	Schematic of supercapacitor devices with laser-scribed graphene electrodes.....	132
6.3	SEMs of surface and edge morphologies of laser-scribed graphene.....	133

6.4	SEMs of scaffold morphologies for immediate- and delayed-casting ionogels in films and devices.....	135
6.5	Impedance data for immediate- and delayed-casting devices compared with data from a device using the neat IL.....	137
6.6	Cyclic voltammetry data for immediate- and delayed-casting devices.....	141
6.7	Charge-discharge data for immediate- and delayed-casting devices.....	143
7.1	Process flow diagram for ionic liquid use and reclamation.....	160
7.2	IL structures and demonstration of immiscibility of IL with water.....	164
7.3	Thermogravimetric data for neat IL, ionogel, reclaimed IL, and scaffold residue.....	167
7.4	Cyclic voltammograms for virgin and reclaimed IL.....	173
8.1	Process diagram for creation of as well as photo and SEM of PDMS-supported ionogels.....	190
8.2	Stress-strain data and modulus versus frequency data for PDMS-supported ionogel.....	192
8.3	Differential scanning calorimetry data for PDMS-supported ionogel, neat IL, and pure PDMS.....	194
8.4	Arrhenius plot of conductivity for neat IL and PDMS-supported ionogel.....	196
9.1	Schematics of possible devices with current collectors.....	215
A1	Determination of setup resistance.....	228
A2	Capacitance versus frequency for compliant ionogel and the neat IL.....	229
A3	Mass loss profiles for compliant and brittle ionogels.....	230
B1	Titration spectra for acid/IL combinations other than BMP TFSI/FA.....	235
B2	Derivatives of titration spectra for acid/IL combinations other than BMP TFSI/FA.....	236
B3	Demonstration of the appearance of pyridinium-associated peaks with increasing acid concentrations.....	237
B4	SEM images of scaffold morphologies for ionogels made with three different IL and both high- and low-FA formulations.....	238
D1	Gel permeation chromatograph for a THF-extracted PDMS-supported ionogel.....	247
D2	PDMS-supported ionogel fatigue testing.....	248
D3	PDMS-supported ionogel elastic modulus versus temperature.....	249
D4	FTIR spectra of a PDMS-supported ionogel, pure PDMS, neat EMI TCB, and the reactive oligomer.....	250

D5	Cyclic voltammograms of a PDMS-supported ionogel and neat EMI TCB .....	251
D6	SEM images of PDMS-supported ionogels prepared using various formulations .....	254
E1	The Gap/Instrument Control window .....	260
E2	The Edit/Start Instrument Test window .....	262
E3	The multiple extension mode test options window .....	265

## List of Tables

2.1 Fraction of IL remaining as carbonaceous residue after thermogravimetric analysis.....	34
3.1 Summary of ionogel physical properties.....	62
3.2 Summary of ionogel electrical properties as compared to the neat IL.....	71
4.1 Properties of selected ionogels.....	93
5.1 Variation of threshold molarities, gelation time, and percentage of copper etched in different ILs.....	112
6.1 Supercapacitor device performance metrics.....	139
7.1 IL properties.....	163
7.2 Effectiveness of IL reclamation process for different ionogels.....	170
B1 Selected IL properties.....	234
C1 Results of IL extraction using volatile organic solvents.....	242
C2 Silica mass percentages pre- and post-IL liberation.....	243

## **Chapter 1**

### **Introduction**

#### **1.1 Opening Thoughts**

The question of how to store and control energy has been one of the central technological challenges facing humanity for millennia. Far from the days of sun-warmed stones and banked fires, humanity has developed complex mechanical and chemical systems that allow us to efficiently store energy in a variety of forms, and with previously-unimaginable convenience.<sup>1</sup> The advent of ubiquitous energy storage has enabled us to find more ways and places to use energy, especially electrical energy, and this in turn feeds our demand for ever increasing storage capacity.<sup>2</sup> Every additional device with which we bedeck ourselves, from smartphones to smart watches to augmented-reality glasses, comes with its own battery.<sup>3,4</sup> The sensors with which we envision “spraying” the world each require their own source of power.<sup>5</sup> In order to build an internet of things, we must also deploy a silent army of storage devices.

In addition to adding new energy services which require the support of energy storage, extant energy services are increasingly being electrified as a path towards decarbonization.<sup>6–8</sup> This trend is most important and most pronounced in the case of transportation, where electric and hybrid vehicles have made significant gains in market share.<sup>9,10</sup> Energy storage is a crucial component of such shifts. Indeed, the need for energy storage as an enabler of transition is amplified as it comes in conjunction with the deployment of “clean” energy generation technologies, such

as solar and wind power, which have inherent intermittency challenges associated with them.<sup>11–16</sup> As such, energy storage is needed as a new component of the electricity transmission and distribution system in order to maintain a balanced grid whether the wind is strong or still, or the day is cloudy or bright.

## **1.2 Supercapacitors as a Solution to Technological Limitations in Electrochemical Energy Storage**

Although energy storage in general, and electrochemical energy storage in particular, have progressed sufficiently as to become enabling technologies, the limitations presented by the current state-of-the-art remain onerous.<sup>17</sup> In part, this is due to the ever-increasing demand for energy. For example, as smartphone battery capacity has increased, so have the energy requirements of the display and processing components, increasing the demand on the batteries and leading to smaller overall gains in battery life.<sup>18,19</sup> However, even without these challenges, most energy storage methods have thus far had some considerable drawbacks. Most mechanical types of energy storage, such as flywheels and pumped hydropower, necessitate major installations and as such are not portable, nor are they economically feasible for the storage of small (sub-grid) amounts of energy or for use in distributed-storage models.<sup>14–16</sup>

The most convenient forms of energy storage at a variety of scales and considering the desirability of portable capabilities are electrochemical in nature. Unfortunately, as compared to liquid fuels used in conjunction with an engine, electrochemical energy storage has been able to deliver only comparable energy

densities or comparable power densities -- not both (Figure 1.1).<sup>20</sup> Conventional capacitors, wherein a layer of electrostatic charge is stored on planar electrodes separated by an insulating dielectric material, offer extremely rapid (fraction of a second) charge and discharge times but are unable to store enough energy to power devices such as smartphones or electric vehicles.<sup>21</sup> The electrochemical cells popularly known as batteries, which allow a chemical reaction to proceed such that electrical current flows through a load, can store useful amounts of energy but are very sensitive to rapid charging or discharging. Rapid power draws from batteries can irreversibly damage cells due to entropic effects.<sup>22</sup> Moreover, while conventional capacitors have essentially unlimited cycle lives when operated within their design parameters, batteries can often withstand only several hundred charge-discharge cycles before undergoing significant capacity losses.<sup>22</sup>



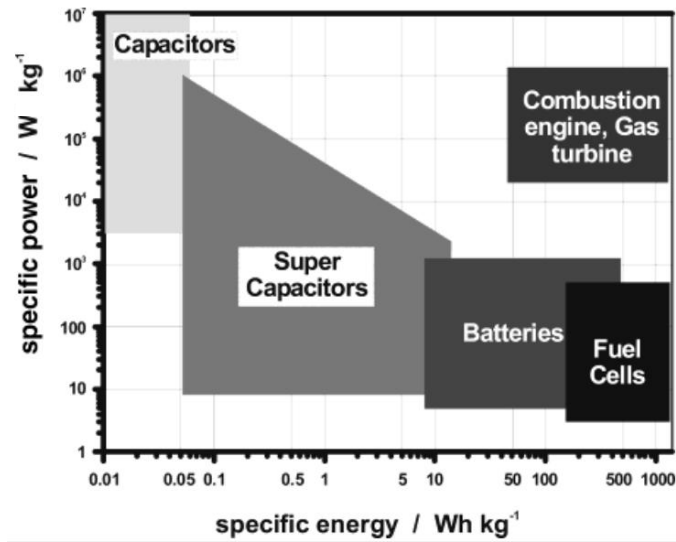


**Figure 1.1.** Ragone plot showing the high power densities of conventional capacitors and high energy densities of batteries. Electrical double-layer capacitors (supercapacitors) have the potential to bridge the gap between these two technologies. Reproduced from Winter & Brodd.<sup>20</sup>

Electrical double-layer capacitors (EDLCs) have the potential to bridge the gap between these two technologies, offering a combination of high energy density and high power density.<sup>20–23</sup> The significant amount of energy that can be stored by EDLCs has earned them monikers such as “ultracapacitors” or “supercapacitors”. EDLCs operate on a similar principle as conventional capacitors (Figure 1.2): energy is stored electrostatically by building up layers of charge but preventing any charge transfer. As mentioned above, the structure of a conventional capacitor is an insulating dielectric material sandwiched between two electrodes (Figure 1.2a). When a voltage is applied to capacitive devices, no current is able to flow between the electrodes. As a result, skins of charge accumulate on the electrodes. When the device is disconnected from the voltage source, the skins of charge remain, storing potential energy. The energy stored in a capacitor is described as follows:

$$(1.1) \quad E = \frac{1}{2} CV^2$$

where  $V$  is the voltage difference across the electrodes and  $C$  is a parameter of the device known as the capacitance, which is defined as the amount of charge stored for a given voltage. Capacitance is normally calculated as:

$$(1.2) \quad C = \epsilon A/d$$

In this equation,  $A$  is the surface area over which charge is stored,  $d$  is the distance which separates the layers of charge, and  $\epsilon$  is the dielectric constant of the insulating layer (a material property).

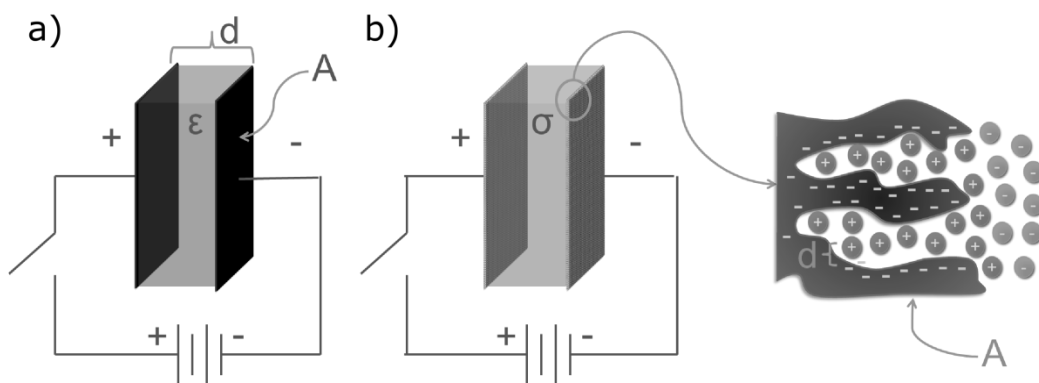


**Figure 1.2.** Schematics of conventional capacitors and supercapacitors. a) A conventional capacitor, consisting of two planar electrodes separated by an insulating dielectric. The energy stored is directly proportional to the dielectric constant of the insulator ( $\epsilon$ ) and the surface area of the electrodes ( $A$ ), and inversely proportional to the distance separating the electrodes ( $d$ ). b) A supercapacitor, consisting of two high-surface area electrodes separated by an ion-conducting electrolyte with some conductivity ( $\sigma$ ). Here, the area is the true surface area of the porous electrode ( $A$ ) and the distance separating layers of charge ( $d$ ) is on the order of nanometers.

EDLCs are able to store significantly more energy than conventional capacitors by replacing the insulating dielectric layer with an electrolyte, a substance that is able to conduct ions but does not conduct electrons (Figure 1.2b).<sup>23</sup> When a layer of charge is built up on one of the electrodes, the ions in the electrolyte respond to form a corresponding layer of charge next to the electrode surface. As a result, instead of the single layer of charge at each electrode/dielectric interface of a conventional capacitor, there exists a double-layer of charge at each electrode/electrolyte interface.<sup>23</sup> Moreover, the distance separating these layers of charge is extremely small, on the nanoscale, which is orders of magnitude smaller than is achievable with insulating materials due to the extremely high field strengths that result.<sup>21</sup> Generally, EDLCs also use high surface area electrodes, such as activated carbons with surface areas of hundreds of meters square per gram.<sup>24</sup> These two material substitutions increase  $A$  and decrease  $d$  by orders of magnitude as compared to conventional capacitors, leading to very high capacitance values and therefore to much higher amounts of energy stored in such devices.

The current state-of-the-art supercapacitors have not been able to live up to the promise of such devices. They generally do not meet or exceed the energy density of batteries and have not shown the excellent power densities at low enough costs to complement batteries in applications such as electric vehicles.<sup>25</sup> In addition, they generally incorporate hazardous materials as discussed below, compounding the safety challenges presented by batteries.<sup>26</sup> As a result, there is significant room for improvement in EDLC technology.

### 1.3 Ionogels as a Solution to Materials Challenges for Electrochemical Energy Storage

Although high-performance supercapacitors may be able to bridge the power/energy gap among current electrochemical energy storage technologies,<sup>21</sup> further materials challenges remain. The materials used in present-day supercapacitors and batteries present significant drawbacks. The conventional electrolytes used in such devices are salt solutions consisting of a complex salt (such as  $\text{LiPF}_6$ ) dissolved in an organic solvent like acetonitrile.<sup>17,25–27</sup> The use of organic solvents allows for wider voltage windows than are tolerable by water. However, these liquids are volatile, flammable, and often toxic.<sup>26</sup>

A possible solution to these challenges is to replace conventional electrolytes with ionic liquids. Ionic liquids (ILs) are salts with very low melting temperatures; generally, a salt is considered an ionic liquid if it is molten at room temperature.<sup>28,29</sup> Most ILs of interest are comprised of an organic cation, often with a ring structure, combined with a fluorinated anion (Figure 1.3). ILs are a unique class of chemicals with a compelling set of properties. They have negligible vapor pressures at ambient conditions.<sup>30</sup> As a result, they pose no inhalation risk and they are not flammable, thereby avoiding two of the major safety drawbacks presented by organic solvents. ILs offer reasonable conductivities (in the range of 10 mS/cm) and are stable to relatively large voltages, sometimes in the range of 4 or more volts.<sup>28,31</sup> This is a significant benefit for EDLCs as the energy stored in such devices is proportional to the square of the charging voltage.<sup>25,27</sup> In addition, ILs are thermally stable to

relatively high temperatures, often at or above 300 °C, and many ILs are hydrophobic, minimizing concerns regarding contamination by water that might limit the voltage window or promote undesirable side reactions. Finally, ILs have been shown to be recyclable in many applications.<sup>30,32–38</sup> ILs are often considered to be “green” chemicals due to this particular combination of properties.

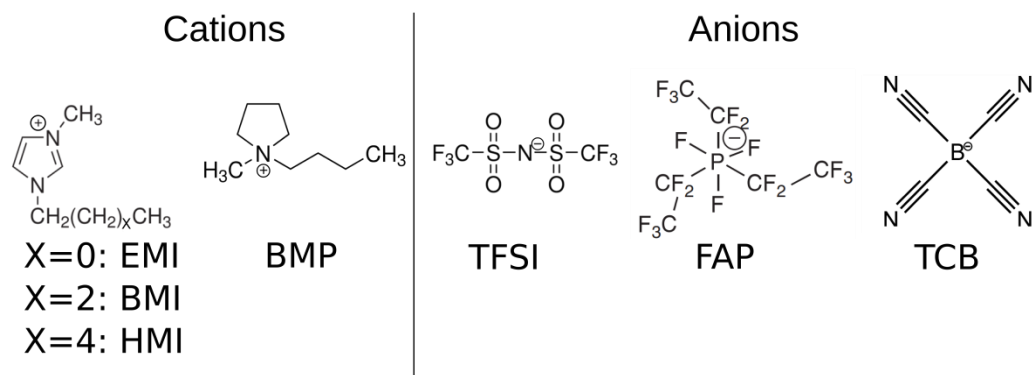


**Figure 1.3.** Structures of ILs used in this study. Cations included:

- 1-ethyl-3-methylimidazolium (EMI)
- 1-butyl-3-methylimidazolium (BMI)
- 1-hexyl-3-methylimidazolium (HMI)
- 1-butyl-1-methylpyrrolidinium (BMP)

Anions included:

- Bis(trifluoromethylsulfonyl)imide (TFSI)
- Tris(perfluoroethyl)trifluorophosphate (FAP)
- Tetracyanoborate (TCB)

ILs are strong candidates for use in electrochemical energy storage devices, and may address many problems with current generations of devices.<sup>31</sup> However, by themselves, they do not optimally improve device energy and power densities. The toxicity profile of ILs is not fully understood, but it is known that some ILs do pose health and environmental hazards.<sup>39–43</sup> As liquids, they are prone to flowing behavior, meaning that any rupture in a device may lead to environmental contamination. To avoid such an episode, containment layers would be required to encase devices with IL electrolytes. In current devices, which use conventional electrolytes, inactive containment layers add weight without improving performance, decreasing energy and power densities.<sup>44</sup> In addition, they preclude the possibility of thin-film and/or flexible device form factors, which is desirable for next-generation technologies.<sup>4</sup>

The necessity of heavy containment layers can be avoided by using a solid electrolyte instead of a liquid, thereby eliminating the possibility of electrolyte leakage.<sup>45–47</sup> ILs are amenable to this schema, as they can easily be immobilized in a solid or solid-like form.<sup>48</sup> Ionic liquid-based gel electrolytes, also known as ionogels, are hybrid materials which combine an IL with a solid scaffold material to prevent flowing behavior. The ideal ionogel offers a variety of benefits, including: a robust but flexible mechanical character; electrical properties that are as close as possible to the neat IL; rapid and *in situ* or solution-based processability; and stability at elevated temperatures.

A variety of processes and scaffold materials have been explored for the purposes of ionogel fabrication.<sup>48–67</sup> The most straightforward methods simply



mix an IL with a pre-formed solid material, such as a polymer, large organic molecule, or inorganic nanoparticles.<sup>49–52</sup> In some cases, such as the common method of mixing an IL with the polymer PVDF-HFP, a cosolvent is required to obtain a single phase which combines both IL and scaffold.<sup>52–54</sup> This cosolvent is then removed through drying to obtain the final ionogel. For other scaffold materials, including fumed silica nanoparticles, the IL can be mixed directly with the solid component to form an ionogel with no solvent needed.<sup>49–51</sup>

In general, these methods do not allow for *in situ* processing of the ionogel, which may complicate device manufacturing. *In situ* processing may be accomplished by synthesizing the scaffold from reagents dissolved in the IL, taking advantage of the IL as a reaction medium as well as in its capacity as an ionic conductor. Such reactions may be conducted with the reactive solution in intimate contact with the electrodes of the device. A significant body of literature has been published concerning polymer-supported ionogels using *in situ* polymerizations, through such routes as UV- or thermally-activated radical polymerizations.<sup>61–64</sup> However, polymer-supported ionogels tend to lack thermal stability.<sup>61</sup> In addition, the requirement of a light path or the ability to add heat to the system may be limiting in terms of device architectures.<sup>65</sup>

Instead, this work focuses on sol-gel processing of ionogels. The term “sol-gel” refers to a class of chemistries that are used to produce complex structures of inorganic oxides, which first are nucleated as small particles (sols) and then condense into a larger gel network.<sup>68</sup> Silica, titania, alumina, and others have been produced using this method.<sup>69–71</sup> A wide variety of sol-gel chemistries have been

characterized, including a range of acid-catalyzed systems.<sup>72,73</sup> Sol-gel syntheses are able to produce very different oxide structures with relatively minor changes in chemistry and processing conditions. All products, however, have the benefits of inorganic oxides in general, including good thermal stability.

Sol-gel chemistry is an industrially-relevant field, which offers several benefits. The behavior of sol-gel systems is very well-characterized. A large body of work describing the stages of sol-gel reactions, the rates thereof and the factors which affect the rates, and the final products has been compiled over the course of several decades.<sup>69–76</sup> This serves as an important resource in understanding how sol-gel chemistry functions in an IL medium.<sup>77</sup> In addition, sol-gel chemistry has been shown to be feasible on an industrial scale, especially for the creation of thin films and coatings.<sup>78</sup> This serves as an important proof of concept that such methods are amenable to scale-up and, moreover, ensures that another body of knowledge exists that may be used as a resource in pursuing the creation of ionogels in an industrial setting.

Ionic liquids were first used in conjunction with sol-gel chemistry as a templating agent and reaction medium with the goal of producing porous silica structures.<sup>79</sup> This method was quickly adapted to make ionogels.<sup>55–57</sup> The particular sol-gel chemistry most commonly used with ILs is an acid-catalyzed, non-hydrolytic route that uses only two reagents, formic acid (FA) and a silicon alkoxide (either tetramethoxysilane, TMOS, or tetraethoxysilane, TEOS).<sup>74</sup> This method is extremely simple and straightforward, and, as the following chapters will show, also incredibly versatile.

## **1.4 Preview of Things to Come**

While the first reports of sol-gel chemistry used to create silica-supported ionogels described brittle, glassy monoliths, this work has demonstrated that the sol-gel method can be used to fabricate a wide variety of products as well as offering important insights into other aspects of ILs, ionogels, and their use.

In Chapter 2, the major experimental methods used in the investigations to follow are described. This includes methods of chemical and physical characterization, as well as electrical testing methods that are used to describe the behavior of ionogels as electrolytes and to evaluate devices made with ionogels.

Chapter 3 describes the innovation of compliant ionogels. By adjusting the reactive formulation used for the sol-gel process, an ionogel with a lower silica content and therefore a soft, compliant mechanical character can be produced. In this chapter, compliant ionogels made using one particular reactive formulation are characterized and compared both to the previously-reported brittle ionogels and to the neat IL.

In Chapter 4, the TMOS/FA/IL phase space is further explored. The conditions under which compliant ionogels may be obtained are described. In addition, the relationship between gelation time, silica morphology, and mechanical character is illuminated using mechanical testing and electron microscopy.

Chapter 5 explores the influence of changing the identity of the IL rather than changing the formulation. A novel titration method based on the use of pyridine

as an FTIR-sensitive probe is introduced. This method is used to determine the relative acidity of solutions of FA in different ILs, and it is demonstrated that the results have predictive value for the relative reaction rates of the sol-gel reaction.

Chapter 6 examines silica-supported ionogels in combination with laser-scribed graphene electrodes. First, it is demonstrated that silica morphology can be altered by casting ionogel films at different points throughout the expected bulk gel time. Then, devices are made and tested with electrolyte films cast at different times, showing that pore blockage can be avoided by using delayed casting.

In Chapter 7, the end-of-service destiny of silica-supported ionogels is pondered. A process is introduced by which the IL can be easily reclaimed and recycled from silica-supported ionogels simply by exposing the ionogels to water. The mechanism underlying this process is discussed, and its efficacy is demonstrated for ionogels made with different ILs, as well as for fumed silica-supported ionogels.

Chapter 8 describes the adaptation of the sol-gel process to create PDMS-supported ionogels. Instead of using a TMOS precursor, PDMS-supported ionogels can be created by applying the sol-gel method to a mixture of IL, FA, and a specially-terminated PDMS oligomer. These novel materials are characterized. In addition, it is demonstrated that lithium can be incorporated into PDMS-supported ionogels, opening the door to further studies on batteries using ionogel electrolytes.

Finally, in Chapter 9, some conclusions are offered and several possible future directions are identified.

## 1.5 References

1. Whittingham, M. S. History, Evolution, and Future Status of Energy Storage. *Proc. IEEE* **100**, 1518–1534 (2012).
2. Foote, C. E. T., Roscoe, A. J., Currie, R. A. F., Ault, G. W. & McDonald, J. R. Ubiquitous energy storage. in 6 (IEEE, 2005). doi:10.1109/FPS.2005.204265
3. Hahn, R. & Reichl, H. Batteries and power supplies for wearable and ubiquitous computing. in 168–169 (IEEE Comput. Soc, 1999). doi:10.1109/ISWC.1999.806705
4. Li, L., Wu, Z., Yuan, S. & Zhang, X.-B. Advances and challenges for flexible energy storage and conversion devices and systems. *Energy Environ. Sci.* **7**, 2101 (2014).
5. Puccinelli, D. & Haenggi, M. Wireless sensor networks: applications and challenges of ubiquitous sensing. *IEEE Circuits Syst. Mag.* **5**, 19–31 (2005).
6. Loftus, P. J., Cohen, A. M., Long, J. C. S. & Jenkins, J. D. A critical review of global decarbonization scenarios: what do they tell us about feasibility?: A critical review of global decarbonization scenarios. *Wiley Interdiscip. Rev. Clim. Change* **6**, 93–112 (2015).
7. Richels, R. G. & Blanford, G. J. The value of technological advance in decarbonizing the U.S. economy. *Energy Econ.* **30**, 2930–2946 (2008).
8. Grübler, A., Nakićenović, N. & Victor, D. G. Dynamics of energy technologies and global change. *Energy Policy* **27**, 247–280 (1999).

9. Shao, S., Pipattanasomporn, M. & Rahman, S. Grid Integration of Electric Vehicles and Demand Response With Customer Choice. *IEEE Trans. Smart Grid* **3**, 543–550 (2012).
10. Green, R. C., Wang, L. & Alam, M. The impact of plug-in hybrid electric vehicles on distribution networks: A review and outlook. *Renew. Sustain. Energy Rev.* **15**, 544–553 (2011).
11. Mossoba, J., Ilic, M. & Casey, L. PV plant intermittency mitigation using constant DC voltage PV and EV battery storage. in 297–301 (IEEE, 2010). doi:10.1109/CITRES.2010.5619791
12. Kempton, W. & Tomić, J. Vehicle-to-grid power implementation: From stabilizing the grid to supporting large-scale renewable energy. *J. Power Sources* **144**, 280–294 (2005).
13. Barton, J. P. & Infield, D. G. Energy Storage and Its Use With Intermittent Renewable Energy. *IEEE Trans. Energy Convers.* **19**, 441–448 (2004).
14. Dunn, B., Kamath, H. & Tarascon, J.-M. Electrical Energy Storage for the Grid: A Battery of Choices. *Science* **334**, 928–935 (2011).
15. Roberts, B. P. & Sandberg, C. The Role of Energy Storage in Development of Smart Grids. *Proc. IEEE* **99**, 1139–1144 (2011).
16. Fertig, E. & Apt, J. Economics of compressed air energy storage to integrate wind power: A case study in ERCOT. *Energy Policy* **39**, 2330–2342 (2011).
17. Kousksou, T., Bruel, P., Jamil, A., El Rhafiki, T. & Zeraouli, Y. Energy storage: Applications and challenges. *Sol. Energy Mater. Sol. Cells* **120**, 59–80 (2014).

18. Perrucci, G. P., Fitzek, F. H. P. & Widmer, J. Survey on Energy Consumption Entities on the Smartphone Platform. in 1–6 (IEEE, 2011). doi:10.1109/VETECS.2011.5956528
19. Chen, X., Chen, Y., Ma, Z. & Fernandes, F. C. A. How is energy consumed in smartphone display applications? in 1 (ACM Press, 2013). doi:10.1145/2444776.2444781
20. Winter, M. & Brodd, R. J. What Are Batteries, Fuel Cells, and Supercapacitors? *Chem. Rev.* **104**, 4245–4270 (2004).
21. Burke, A. Ultracapacitors: why, how, and where is the technology. *J. Power Sources* **91**, 37–50 (2000).
22. Miller, J. R. & Simon, P. Electrochemical Capacitors for Energy Management. *Science* **321**, 651–652 (2008).
23. Conway, B. E. *Electrochemical Supercapacitors Scientific Fundamentals and Technological Applications*. (Springer US, 1999).
24. Zhang, L. L. & Zhao, X. S. Carbon-based materials as supercapacitor electrodes. *Chem. Soc. Rev.* **38**, 2520 (2009).
25. Hall, P. J. *et al.* Energy storage in electrochemical capacitors: designing functional materials to improve performance. *Energy Environ. Sci.* **3**, 1238 (2010).
26. Walden, G., Stepan, J. & Mikolajczak, C. Safety considerations when designing portable electronics with Electric Double-Layer Capacitors (Supercapacitors). in 1–5 (IEEE, 2011). doi:10.1109/PSES.2011.6088259



27. Béguin, F., Presser, V., Balducci, A. & Frackowiak, E. Supercapacitors: Carbons and Electrolytes for Advanced Supercapacitors. *Adv. Mater.* **26**, 2283–2283 (2014).
28. Armand, M., Endres, F., MacFarlane, D. R., Ohno, H. & Scrosati, B. Ionic-liquid materials for the electrochemical challenges of the future. *Nat. Mater.* **8**, 621–629 (2009).
29. Earle, M. J. & Seddon, K. R. Ionic liquids. Green solvents for the future. *Pure Appl. Chem.* **72**, 1391–1398 (2000).
30. Earle, M. J., McCormac, P. B. & Seddon, K. R. Diels–Alder reactions in ionic liquids. A safe recyclable alternative to lithium perchlorate–diethyl ether mixtures. *Green Chem.* **1**, 23–25 (1999).
31. Fericola, A., Scrosati, B. & Ohno, H. Potentialities of ionic liquids as new electrolyte media in advanced electrochemical devices. *Ionics* **12**, 95–102 (2006).
32. Aprile, C. *et al.* New ionic liquid-modified silica gels as recyclable materials for l-proline- or H-Pro–Pro–Asp–NH<sub>2</sub>-catalyzed aldol reaction. *Green Chem.* **9**, 1328–1334 (2007).
33. Shill, K. *et al.* Ionic liquid pretreatment of cellulosic biomass: Enzymatic hydrolysis and ionic liquid recycle. *Biotechnol. Bioeng.* **108**, 511–520 (2011).
34. Wu, B., Liu, W., Zhang, Y. & Wang, H. Do We Understand the Recyclability of Ionic Liquids? *Chem. - Eur. J.* **15**, 1804–1810 (2009).

35. Yadav, J., Reddy, B., Basak, A. & Venkat Narsaiah, A. Recyclable 2nd generation ionic liquids as green solvents for the oxidation of alcohols with hypervalent iodine reagents. *Tetrahedron* **60**, 2131–2135 (2004).
36. Zhang, X., Fan, X., Niu, H. & Wang, J. An ionic liquid as a recyclable medium for the green preparation of  $\alpha,\alpha'$ -bis (substituted benzyldiene)cycloalkanones catalyzed by  $\text{FeCl}_3 \cdot 6\text{H}_2\text{O}$ . *Green Chem.* **5**, 267–269 (2003).
37. Zhu, H.-P., Yang, F., Tang, J. & He, M.-Y. Brønsted acidic ionic liquid 1-methylimidazolium tetrafluoroborate: a green catalyst and recyclable medium for esterification. *Green Chem.* **5**, 38 (2003).
38. Horowitz, A. I., Wang, Y. & Panzer, M. J. Reclamation and reuse of ionic liquids from silica-based ionogels using spontaneous water-driven separation. *Green Chem.* **15**, 3414–3420 (2013).
39. Kulacki, K. J. & Lamberti, G. A. Toxicity of imidazolium ionic liquids to freshwater algae. *Green Chem.* **10**, 104–110 (2008).
40. Ranke, J. *et al.* Lipophilicity parameters for ionic liquid cations and their correlation to in vitro cytotoxicity. *Ecotoxicol. Environ. Saf.* **67**, 430–438 (2007).
41. Ventura, S. P. M. *et al.* Designing ionic liquids: the chemical structure role in the toxicity. *Ecotoxicology* **22**, 1–12 (2012).
42. Zhao, D., Liao, Y. & Zhang, Z. Toxicity of Ionic Liquids. *CLEAN – Soil Air Water* **35**, 42–48 (2007).

43. Ranke, J., Stolte, S., Störmann, R., Arning, J. & Jastorff, B. Design of Sustainable Chemical Products The Example of Ionic Liquids. *Chem. Rev.* **107**, 2183–2206 (2007).
44. Liu, L. *et al.* Nanostructured Graphene Composite Papers for Highly Flexible and Foldable Supercapacitors. *Adv. Mater.* **26**, 4855–4862 (2014).
45. Ho, C. *et al.* Dispenser printed electrochemical capacitors for power management of millimeter scale lithium ion polymer microbatteries for wireless sensors. in *6th international workshop on micro and nanotechnology for power generation and energy conversion applications (PowerMEMS 2006)*, Berkeley, CA 219–222 (2006).
46. Fergus, J. W. Ceramic and polymeric solid electrolytes for lithium-ion batteries. *J. Power Sources* **195**, 4554–4569 (2010).
47. Morford, R., Welna, D., Kellamiii, C., Hofmann, M. & Allcock, H. A phosphate additive for poly(ethylene oxide)-based gel polymer electrolytes. *Solid State Ion.* **177**, 721–726 (2006).
48. Le Bideau, J., Viau, L. & Vioux, A. Ionogels, ionic liquid based hybrid materials. *Chem. Soc. Rev.* **40**, 907–925 (2011).
49. Ueno, K., Hata, K., Katakabe, T., Kondoh, M. & Watanabe, M. Nanocomposite Ion Gels Based on Silica Nanoparticles and an Ionic Liquid: Ionic Transport, Viscoelastic Properties, and Microstructure. *J. Phys. Chem. B* **112**, 9013–9019 (2008).

50. Ueno, K., Imaizumi, S., Hata, K. & Watanabe, M. Colloidal interaction in ionic liquids: Effects of ionic structures and surface chemistry on rheology of silica colloidal dispersions. *Langmuir* **25**, 825–831 (2008).
51. Ueno, K. & Watanabe, M. From Colloidal Stability in Ionic Liquids to Advanced Soft Materials Using Unique Media. *Langmuir* **27**, 9105–9115 (2011).
52. Yeon, S.-H., Kim, K.-S., Choi, S., Cha, J.-H. & Lee, H. Characterization of PVdF(HFP) Gel Electrolytes Based on 1-(2-Hydroxyethyl)-3-methyl Imidazolium Ionic Liquids. *J. Phys. Chem. B* **109**, 17928–17935 (2005).
53. Lee, K. H., Zhang, S., Lodge, T. P. & Frisbie, C. D. Electrical Impedance of Spin-Coatable Ion Gel Films. *J. Phys. Chem. B* **115**, 3315–3321 (2011).
54. Gu, Y. *et al.* High Toughness, High Conductivity Ion Gels by Sequential Triblock Copolymer Self-Assembly and Chemical Cross-Linking. *J. Am. Chem. Soc.* **135**, 9652–9655 (2013).
55. Néouze, M.-A., Bideau, J. L., Gaveau, P., Bellayer, S. & Vioux, A. Ionogels, New Materials Arising from the Confinement of Ionic Liquids within Silica-Derived Networks. *Chem. Mater.* **18**, 3931–3936 (2006).
56. Néouze, M.-A., Le Bideau, J. & Vioux, A. Versatile heat resistant solid electrolytes with performances of liquid electrolytes. *Prog. Solid State Chem.* **33**, 217–222 (2005).
57. Néouze, M.-A., Bideau, J. L., Leroux, F. & Vioux, A. A route to heat resistant solid membranes with performances of liquid electrolytes. *Chem. Commun.* 1082–1084 (2005). doi:10.1039/b416267f

58. Gayet, F. *et al.* Polymer nanocomposite ionogels, high-performance electrolyte membranes. *J. Mater. Chem.* **20**, 9456–9462 (2010).
59. Kavanagh, A. *et al.* Photo-patternable hybrid ionogels for electrochromic applications. *J. Mater. Chem.* **21**, 8687 (2011).
60. Patel, M., Gnanavel, M. & Bhattacharyya, A. J. Utilizing an ionic liquid for synthesizing a soft matter polymer ‘gel’ electrolyte for high rate capability lithium-ion batteries. *J. Mater. Chem.* **21**, 17419–17424 (2011).
61. Susan, M. A. B. H., Kaneko, T., Noda, A. & Watanabe, M. Ion Gels Prepared by in Situ Radical Polymerization of Vinyl Monomers in an Ionic Liquid and Their Characterization as Polymer Electrolytes. *J. Am. Chem. Soc.* **127**, 4976–4983 (2005).
62. Visentin, A. F. & Panzer, M. J. Poly(Ethylene Glycol) Diacrylate-Supported Ionogels with Consistent Capacitive Behavior and Tunable Elastic Response. *ACS Appl. Mater. Interfaces* **4**, 2836–2839 (2012).
63. Visentin, A. F., Alimena, S. & Panzer, M. J. Influence of Ionic Liquid Selection on the Properties of Poly(Ethylene Glycol) Diacrylate-Supported Ionogels as Solid Electrolytes. *ChemElectroChem* **1**, 718–721 (2014).
64. Visentin, A. F., Dong, T., Poli, J. & Panzer, M. J. Rapid, microwave-assisted thermal polymerization of poly(ethylene glycol) diacrylate-supported ionogels. *J. Mater. Chem. A* **2**, 7723 (2014).
65. Flores Zopf, S. & Panzer, M. Integration of UV-cured Ionogel Electrolyte with Carbon Paper Electrodes. *AIMS Mater. Sci.* **1**, 59–69 (2014).

66. Horowitz, A. I. & Panzer, M. J. High-performance, mechanically compliant silica-based ionogels for electrical energy storage applications. *J. Mater. Chem.* **22**, 16534–16539 (2012).
67. Horowitz, A. I. & Panzer, M. J. Poly(dimethylsiloxane)-Supported Ionogels with a High Ionic Liquid Loading. *Angew. Chem.* **126**, 9938–9941 (2014).
68. Brinker, C. J. & Scherer, G. W. *Sol-gel science the physics and chemistry of sol-gel processing*. (Academic Press, 1990).
69. Hench, L. L. & West, J. K. The sol-gel process. *Chem. Rev.* **90**, 33–72 (1990).
70. Hench, L. L. & Ulrich, D. R. *Ultrastructure processing of ceramics, glasses, and composites*. (Wiley, 1984).
71. Mackenzie, J. D. & Ulrich, D. R. *Ultrastructure processing of advanced ceramics*. (Wiley, 1988).
72. Klein, L. C. Sol-Gel Processing of Silicates. *Annu. Rev. Mater. Sci.* **15**, 227–248 (1985).
73. Vioux, A. Nonhydrolytic Sol–Gel Routes to Oxides. *Chem. Mater.* **9**, 2292–2299 (1997).
74. Sharp, K. G. A two-component, non-aqueous route to silica gel. *J. Sol-Gel Sci. Technol.* **2**, 35–41 (1994).
75. Mackenzie, J. D. Structures and properties of Ormosils. *J. Sol-Gel Sci. Technol.* **2**, 81–86 (1994).
76. Philipp, G. & Schmidt, H. New materials for contact lenses prepared from Si- and Ti-alkoxides by the sol-gel process. *J. Non-Cryst. Solids* **63**, 283–292 (1984).

77. Vioux, A., Viau, L., Volland, S. & Le Bideau, J. Use of ionic liquids in sol-gel; ionogels and applications. *Comptes Rendus Chim.* **13**, 242–255 (2010).
78. Zarzycki, J. Past and present of sol-gel science and technology. *J. Sol-Gel Sci. Technol.* **8**, 17–22 (1997).
79. Dai, S. *et al.* Preparation of silica aerogel using ionic liquids as solvents. *Chem. Commun.* **3**, 243–244 (2000).

## **Chapter 2**

### **Major Experimental Tools and Techniques**

#### **2.1 Introduction**

The majority of the work described in this thesis concerns the development and use of new materials. As a result, one of the most important endeavors undertaken in during this work was materials characterization. Several major methods were used to characterize the ionogels developed in the course of this work, many of which were used during multiple investigations. This chapter presents an overview of the major analytical techniques used in this thesis. These techniques can be broadly classified into three groups: chemical characterization, mechanical characterization, and electrochemical testing.

#### **2.2 Chemical Characterization**

Chemical characterization techniques were used to determine the chemical composition of ionogels or IL-based solutions, as well as their thermal properties. As the sol-gel reaction used to form ionogels in these studies is relatively well-understood, detailed characterization of the scaffold molecular structure using nuclear magnetic resonance spectroscopy was not undertaken. Instead, two methods based on measuring a sample's response to temperature changes were employed: thermogravimetric analysis and differential scanning calorimetry. In addition, Fourier transform infrared spectroscopy was used to detect the presence



of certain bonds or compounds in ionogel samples. Finally, Karl-Fischer titration was used to determine the water content of the ILs in their as-stored state.

### 2.2.1 Thermogravimetric Analysis (TGA)

Although the initial composition of the ionogel reaction mixture is known, the production of volatile byproducts means that not all of the reagent mass is incorporated into the final ionogel. Moreover, the TMOS conversion rate is often less than 100% and the composition of the resultant silica can range from  $\text{SiO}$  to  $\text{SiO}_4$ ,<sup>1,2</sup> meaning that it is difficult to analytically predict the final silica mass in an ionogel. However, knowledge of the percentage of the ionogel mass that is comprised of IL or scaffold is crucial in order to properly contextualize the ionogel's properties and to compare ionogels created through sol-gel to other ionogel types.

TGA was the main tool employed to determine the composition of ionogels. The principle of operation of TGA is as follows: a small amount of sample is loaded directly into a platinum basket, which is suspended from the hook of an extremely sensitive balance. This assemblage is then sealed into an oven, and a temperature program is run under an inert nitrogen atmosphere. As the temperature rises, various components of the sample vaporize and the vapors are entrained and removed by the flow of nitrogen throughout the oven chamber.

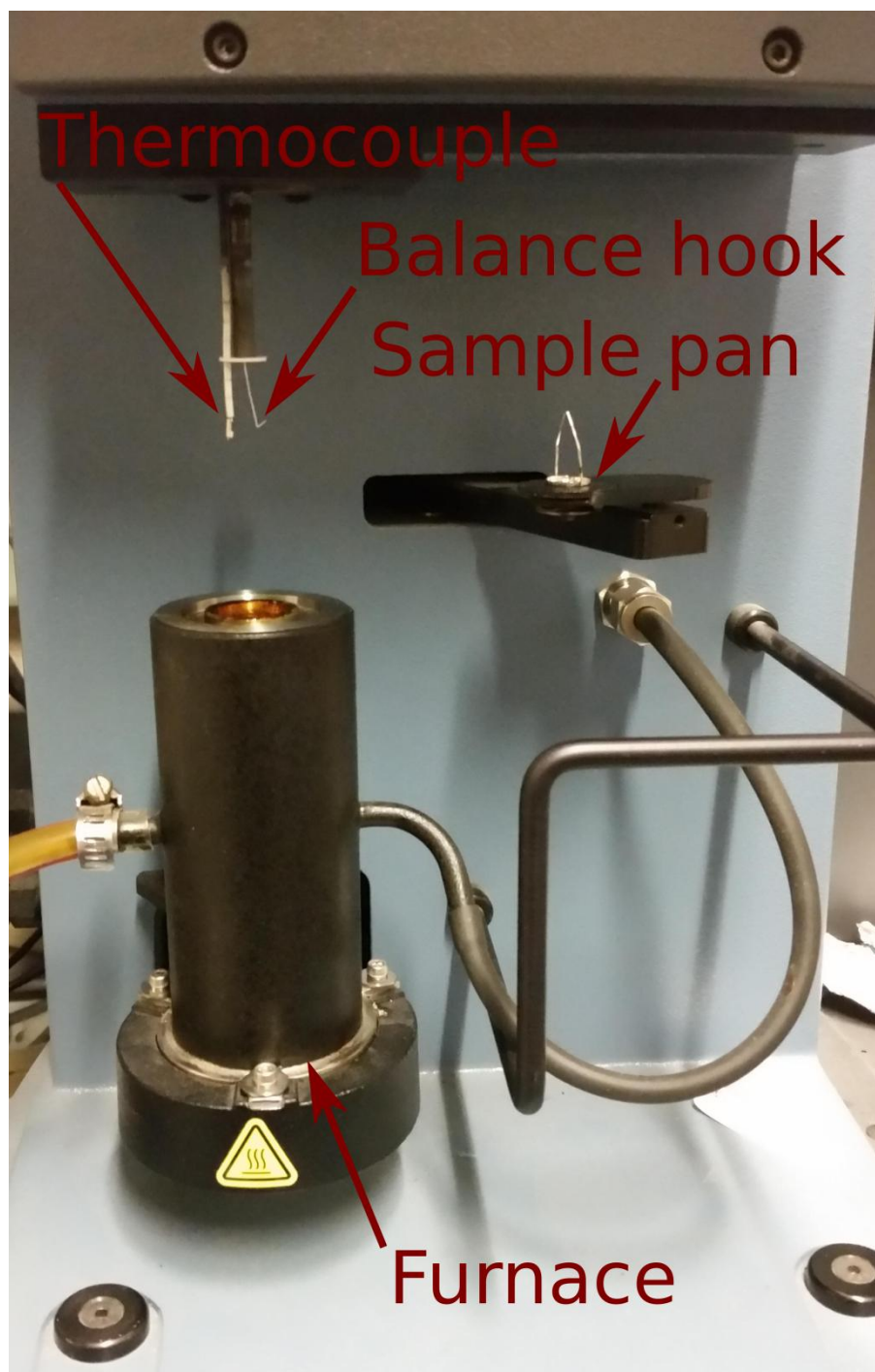


**Figure 2.1.** Photo of the thermogravimetric analysis instrumentation. Samples are placed in the platinum sample pan, which is then lifted by the balance hook. The furnace rises to enclose the sample during test runs.

The use of TGA to determine the composition of ionogels is based on the fact that the temperature at which ILs decompose is generally much lower than the temperature at which silica decomposes (Figure 2.2). Indeed, silica is thermally stable until well over 1000 °C,<sup>3</sup> whereas ILs generally decompose in the range 300-400 °C. As a result, the composition of a silica-supported ionogel can be calculated by gradually raising the sample's temperature from ambient to significantly above the IL's decomposition temperature (trials generally end in the range 600-800 °C).

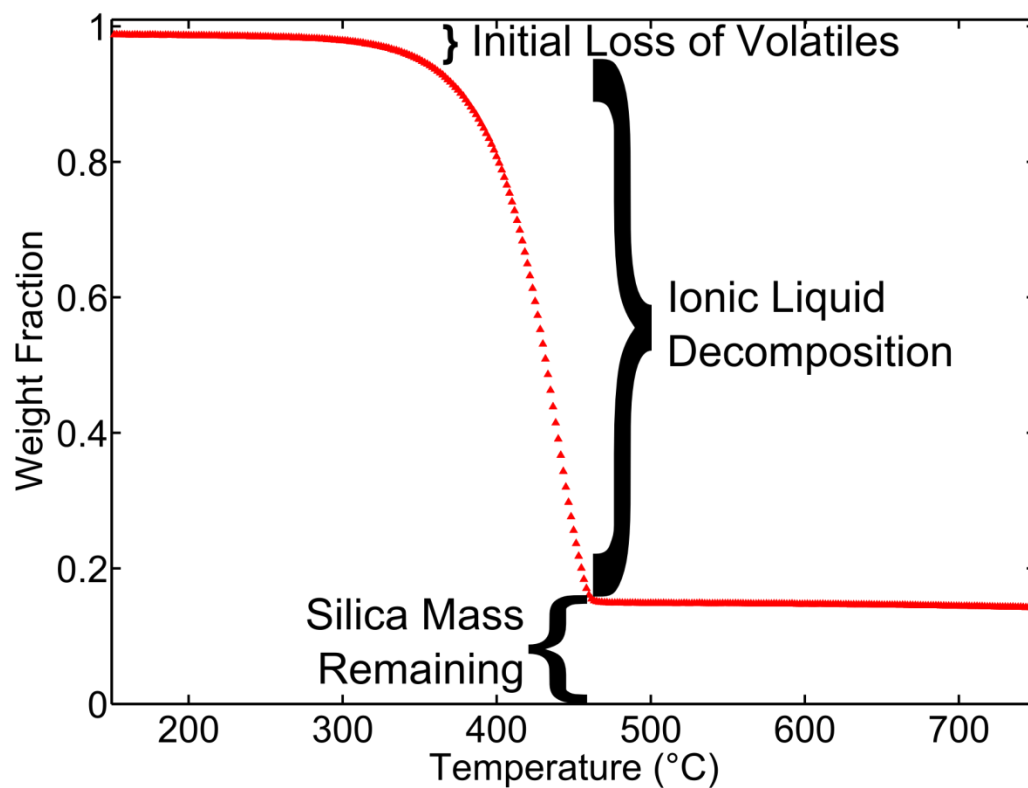


**Figure 2.2.** Example TGA trace of a silica-supported ionogel made with EMI TFSI. Data shows the initial loss of volatile material at mild temperatures, the decomposition of the IL at ~400 °C, and the residual mass representing the silica scaffold.

The mass fraction of silica mass in the sample (on a dry basis) can be calculated as the mass left after the IL decomposition ( $m_S$ ) divided by the total sample mass ( $m_T$ ) after correcting for the initial loss of water and leftover volatile compounds ( $m_V$ ):

$$(2.1) \quad F_S = m_S / (m_T - m_V)$$

The fraction of IL can then be simply calculated as:

$$(2.2) \quad F_{IL} = 1 - F_S = 1 - m_S / (m_T - m_V)$$

A simple continuous ramp temperature program was used for analytical trials, in which the temperature was raised from ambient at a rate of 10 °C/min. Since program was not paused to allow for total IL decomposition, the decomposition temperature of a given IL may appear to differ from sample to sample. These apparent differences arise due to variations in sample size, shape, and composition, which lead to different heat transfer rates. However, this factor does not affect the calculation of ionogel composition as the IL decomposition remains a single well-defined transition that ends before 500 °C.

For some ILs, a significant amount of carbonaceous residue was leftover after thermal decomposition. This was corrected for by running a TGA program on a sample of pure IL, calculating what amount of the IL mass is left as residue ( $m_R$ ) and the corresponding mass fraction ( $F_R$ ), and incorporating this into the percentage scaffold calculation above:

$$(2.3) \quad F_{IL} = 1 - (m_S - m_R) / (m_T - m_V)$$

$$m_R = m_{IL} * F_R = F_{IL} * (m_T - m_V) * F_R$$

$$F_{IL} = 1 - (m_S - F_{IL} * [m_T - m_V] * F_R) / (m_T - m_V)$$

$$F_{IL} = 1 - m_S/(m_T - m_V) + F_{IL} * F_R$$

$$F_{IL}(1-F_R) = 1 - m_S/(m_T - m_V)$$

$$(2.4) \quad F_{IL} = 1/(1-F_R) - m_S/[(m_T - m_V)(1-F_R)]$$

In the case of a small  $F_R$ , equation 2.4 reduces to equation 2.2.

**Table 2.1.** The fraction of IL that remains as carbonaceous residue after thermal decomposition ( $F_R$ ) for various ILs as measured using TGA. Generally, an  $F_R$  value of less than 10% has a within-error effect on the calculation of scaffold or IL content. The value for EMI TCB is notably larger than those of the other ILs.

<b>Ionic Liquid</b>	<b><math>F_R</math></b>
EMI TFSI	0.014
BMI TFSI	0.11
HMI TFSI	0.11
BMP TFSI	0.004
EMI FAP	0.054
EMI TCB	0.308

Similar techniques were used to calculate the compositions of samples of different types, including PDMS-supported ionogels and post-recovery samples of IL and silica (see Appendix C). As PDMS is less thermally-stable than silica, a stepped program was used for PDMS-supported ionogels to isolate the IL decomposition. Since silica is stable to extremely high temperatures, TGA was also used to prepare samples for SEM imaging by selectively burning out the IL component and leaving only the silica scaffold. A ramp program with a heating rate of 10 °C and a terminal temperature of 800 °C was used to prepare samples for SEM imaging.

#### 2.2.2 Differential Scanning Calorimetry (DSC)

Similarly to TGA, DSC subjects a sample to a pre-set temperature program. However, instead of measuring changes in mass, DSC measures changes in heat flow as compared to a blank reference sample (an empty sample pan). This allows the detection of transitions such as the onset of chemical reactions, glass transitions, or phase transitions. DSC was used to confirm that the scaffold of PDMS-supported ionogels contained negligible unreacted end groups (see Chapter 8).

#### 2.2.3 Fourier Transform Infrared Spectroscopy (FTIR)

FTIR is a technique which uses the interaction of a sample with infrared light to detect the presence of chemical bonds, as the vibrational energies of these bonds are often of the same order as light in the infrared range.<sup>4</sup> FTIR

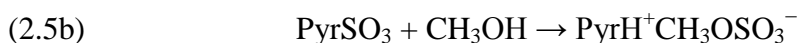
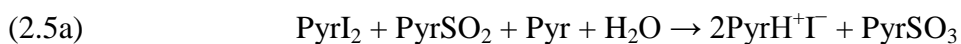


spectroscopy returns a spectrum of absorption vs. wavenumber (inverse wavelength) in which individual bonds appear as peaks. These peaks can range between sharp and broad, with varying intensities. Some may appear as doublets. Thermodynamic calculations can be used to attribute some peaks to certain motions of particular bonds, such as stretching, bending, or twisting vibrational modes. In the “fingerprint region”, between 600 and 1400  $\text{cm}^{-1}$ , it is impossible to assign peaks to vibrational modes due to the complexity of the spectra.<sup>5</sup> Instead, correlational assignments are developed to relate certain patterns to compounds or structures. FTIR data is very susceptible to signal occlusion or interference in the case of complex, multi-component samples.

FTIR spectroscopy was used in two main ways during the course of this thesis. First, it was used as the basis of a titration technique that employed pyridine as an IR-sensitive reporter. This technique was designed as a simple way to ascertain the strength of acids in different ILs. Pyridine has two particularly useful IR-active vibrational modes that undergo significant shifts as pyridine is protonated into pyridinium, making it a useful “indicator” molecule. This technique is described further in Chapter 5. Second, FTIR was used to detect the presence of the reactive end groups of the functionalized PDMS oligomer that is the precursor to the creation of PDMS-supposed ionogels. For ionogel samples, the reactive end group signals are impossible to detect or much decreased in intensity as compared to the oligomer, as discussed in Chapter 8.

#### 2.2.4 Karl Fischer Titration

Karl Fischer titration is a specialized technique that is used to very precisely determine the amount of water in a very dry sample. It is a voltammetric technique that detects the reaction of iodine and sulfur dioxide that occurs in the presence of both water and excess of a suitable base (normally pyridine), as carried out in an alcohol medium (typically methanol). This reaction<sup>6</sup> can be expressed simply as:



The reaction is monitored by applying a voltage to two electrodes. When  $\text{I}_2$  is present in the system (i.e., when there is no water present), current flows between these two electrodes due to the reduction of  $\text{I}_2$  to  $2\text{I}^-$  at the cathode and the oxidation of  $2\text{I}^-$  to  $\text{I}_2$  at the anode.<sup>6</sup> As such, the onset of a significant current is the point at which all of the water in the system has been consumed. Automatic Karl Fischer titrators precisely measure the amount of reagent (a dry mixture of  $\text{I}_2$  and  $\text{SO}_2$ ) added to the system during a given titration, allowing the water concentration or mass percentage can be calculated by simply inputting the sample mass.

Karl Fischer titrations were only carried out in one investigation in this work (see Chapter 7) in order to determine the water contents of ILs stored in general chemical storage and of as-prepared ionogels. However, these results are an important component of the context of the work as a whole. As the presence of water can greatly affect the course of the sol-gel reaction, it was important to

demonstrate that the ILs contain only very small amounts of water in their as-stored state.

## **2.3 Mechanical Characterization**

### **2.3.1 Stress/Strain Testing**

Stress/strain testing is a class of methods in which a mechanical force is applied to a sample. Two elements of the sample's response are measured: the amount of force with which the sample "pushes back" or resists the applied force (the stress) and the amount by which the sample deforms in response to the applied force (the strain). The quotient of these two quantities is a modulus that expresses the relative stiffness of a given material. A soft material undergoes significant deformation as a response to a relatively small stress, while a stiff material deforms very little under even large stresses. The applied force can be compressive, tensile, or shear in nature. The first two modes allow the calculation of an elastic modulus, while the application of a shear force enables the determination of a shear modulus.

As all of the ionogels made during the course of this thesis were solid materials, they were tested using simple compressive parallel-plate testing rather than rheometry (as is appropriate for more liquid-like samples). Compressive testing was used instead of tensile testing as many samples were too soft to allow for the use of clamps, which is necessary for the application of tensile stress. Parallel-plate stress/strain testing is quite straightforward: a sample is loaded onto

a plate, and a second plate is brought into contact with the top of the sample (Figure 2.3). Then, the top plate is lowered at a controlled, slow rate (normally 0.015 mm/s in these investigations) to apply a compressive force. A relatively slow rate is used to ensure that the sample has time to respond to the applied force.

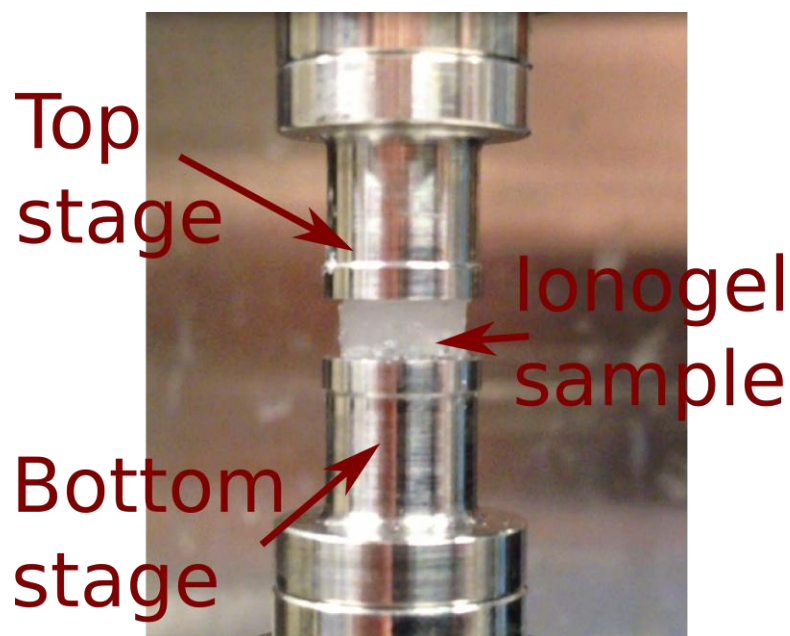


**Figure 2.3.** The DMA experimental setup as shown with a sample of PDMS-supported ionogel. The top stage moves up and down to apply and remove compressive stress, while the gap between the two stages is measured to enable calculation of the strain experienced by the sample. The diameter of the ionogel sample shown is approximately 0.625 cm.

The calculation of an elastic modulus is performed by conducting a linear regression on the stress/strain data from a region in which the data is close to linear (suggesting that the sample was undergoing elastic, or reversible, deformation) and taking the slope of the resulting line (Figure 2.4). In most tested ionogel samples, a region between 15% and 25% strain was used as this was after the initial loading stage and before the point of sample yielding (after the sample undergoes plastic, or irreversible, deformation). Samples were subjected to one or two stress cycles, consisting of a loading step and an unloading step, to measure the elastic modulus, find the yield stress, and qualitatively determine the extent of hysteresis experienced by the samples. A set of directions for conducting stress/strain tests can be found in Appendix E.

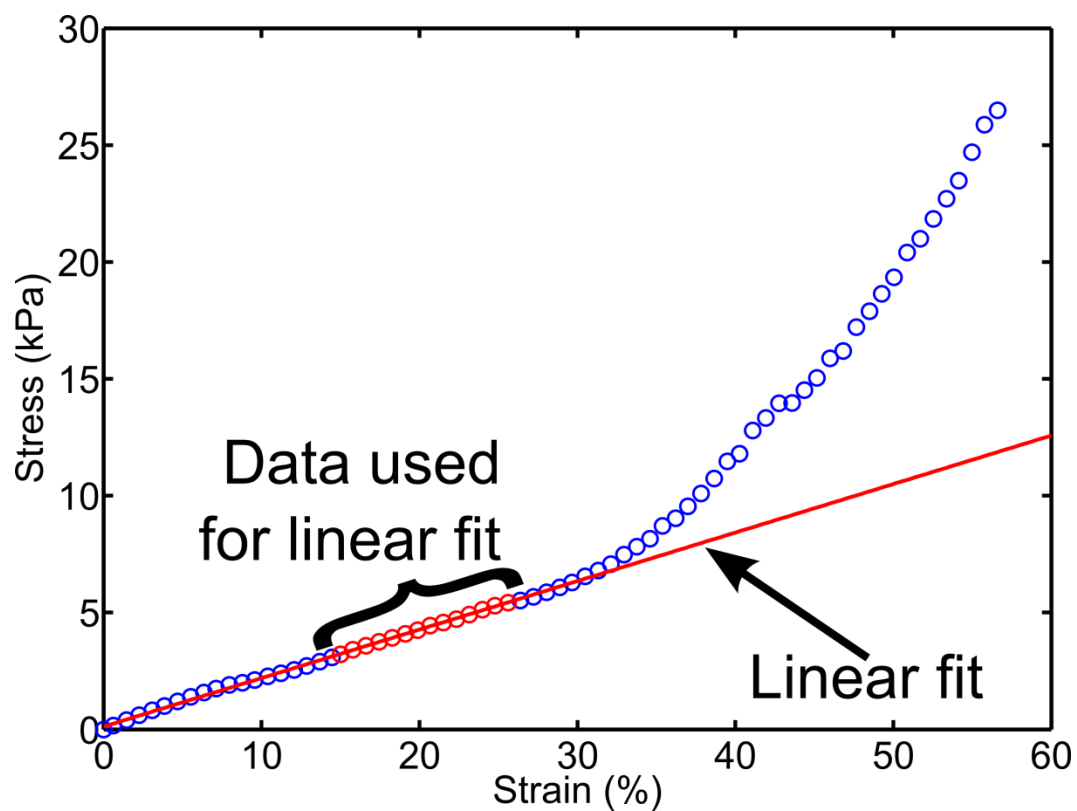


**Figure 2.4.** Example stress/strain data for a silica-supported ionogel subjected to a single loading. The data between 15 and 25% strain (highlighted in red) was used to calculate a linear fit. The slope of the calculated line is the elastic modulus of the ionogel.

### 2.3.2 Dynamic Mechanical Analysis

In addition to single stress/strain trials, a testing regime that uses repeated, rapid application of loading/unloading cycles was used to further explore the mechanical characteristics of PDMS-supported ionogels. During these trials, samples were pre-loaded with several grams of force to ensure contact of the top plate at all times, and then a small deformation was repeatedly applied and removed at a frequency of 1 Hz. This approach allows for relatively rapid data collection for several applications. In this investigation, it was used to demonstrate that sample behavior was primarily elastic (as opposed to primarily viscous, or time-dependent) as well as to measure the endurance of ionogel samples to thousands of stress cycles and to test the mechanical properties at elevated temperatures. This data can be found in Chapter 8.

## 2.4 Electrical Testing

As discussed in Chapter 1, ionogels are electrolytes, or ionic conductors, as opposed either to insulating dielectric materials or to materials that conduct electrons. Electrical testing is crucial to ascertain an ionogel's usefulness as a possible component in electrochemical energy storage devices. In order to conduct electrical investigations, the ionogel must be tested in conjunction with a pair of electrodes, thereby allowing the application and measuring of electrical signals. Ionogels were tested against two kinds of electrodes in this work. First, novel materials were tested with planar electrodes of an inert material such as glassy carbon. The use of non-porous, low-resistance electrodes allows the



determination of inherent material properties of the ionogel. Second, silica-supported ionogels were tested against high surface area graphene electrodes. These tests demonstrate the ionogel in an actual supercapacitor device, and the results arise from a combination of the ionogels' properties and the properties of the electrode material.

A range of electrical properties are of interest, including ionic conductivity, capacitance, switching frequency, and voltammetric stability window.<sup>7</sup> These metrics characterize how quickly the ions of the IL can move past one another to form electrical double-layers (EDLs) against an electrode surface (be it porous or planar) when a voltage is applied, how much charge can be stored in the double-layers, and how strong of an electrical field the ionogel can withstand before undesirable side reactions occur. Generally, ionic conductivity, switching frequency, and capacitance values were gleaned from electrical impedance spectroscopy data. Cyclic voltammetry was used to confirm capacitance values and demonstrate stability windows. For devices made with graphene electrodes, charge-discharge testing was conducted to determine the amount of energy stored in these prototypical devices.

#### 2.4.1 Electrical Impedance Spectroscopy (EIS)

EIS is a technique in which a very small (RMS = 10 mV in these investigations) AC voltage signal is applied to a test cell consisting of an ionogel in contact with two electrodes as described above. The frequency of the signal is varied from values as high as 1 MHz to minimum frequencies of 10 or even 1

mHz. The return signal is recorded at each frequency and analyzed to determine the voltage drop across the test cell and the phase shift as compared to the source signal.<sup>8</sup> These two measurements, taken together, are then used by the spectrometer to calculate the impedance of the test cell, which is the complex equivalent of resistance in the time-dependent phrasing of Ohm's law:

$$(2.6) \quad V(t) = I(t) * Z$$

where  $Z$  is the complex impedance. In the case of planar electrodes, impedance behavior can essentially be attributed solely to the ionogel.

If ionogels were lossless ionic conductors, the return signal of a capacitor made with an ionogel electrolyte would be at a  $-90^\circ$  phase shift relative to the source signal at all frequencies. In other words, at the maximum voltage, no current would flow (as the capacitor would be fully charged and therefore act like an open circuit), while when the voltage was zero, the current flow would be at its maximum (as the capacitor discharged). Moreover, there would be no voltage drop across the test cell as the ionogel would present no real resistance to current flow (as opposed to the “imaginary”, or time-dependent, signal shifting effect). As such, the complex impedance would have only an imaginary component, with the real component being zero.

In reality, however, ionogels are lossy materials. Several real resistances operate in an ionogel-based capacitor, including the resistance of the electrodes and system setup, the “resistance” represented by any areas of poor physical contact between the ionogel and the electrode, and the resistance of the signal travelling through the bulk of the ionogel itself.<sup>9</sup> At high frequencies, the polarity

of the voltage switches too quickly for the relatively large and bulky ions of the IL to form a complete EDL.<sup>10</sup> As a result, the phase shift of the return signal is close to zero, the impedance appears to be frequency-independent, and the measured behavior is primarily resistive in nature (Figure 2.5). This allows the calculation of the ionic conductivity (or inverse resistivity) of the ionogel material as:

$$(2.7) \quad \sigma = (Z_{\text{Real}})^{-1} * (t/A)$$

where  $Z_{\text{Real}}$  is the value of the real component of impedance at a high frequency (typically ~100 kHz),  $t$  is the thickness of the ionogel layer and  $A$  is the contact area between the ionogel and one of the electrodes. This equation is valid for parallel-plate configurations.

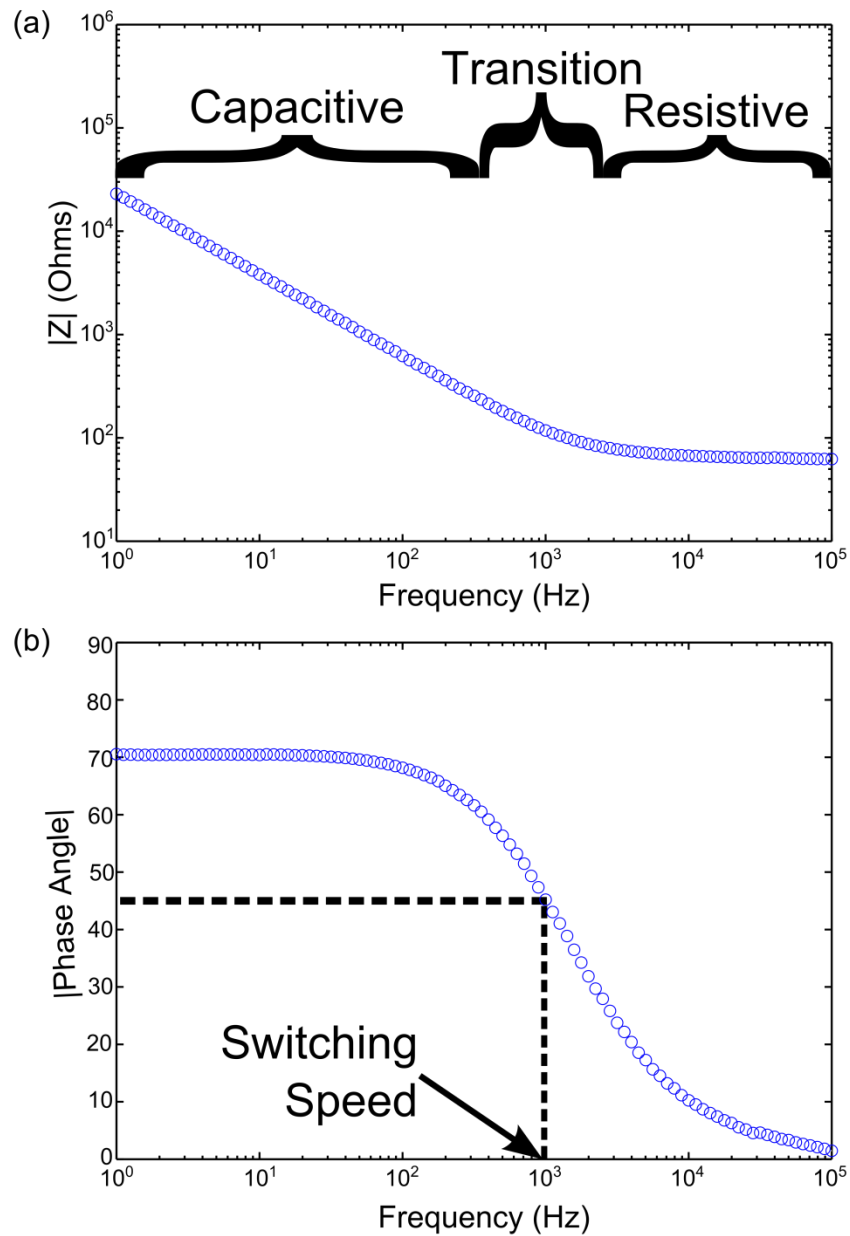


**Figure 2.5.** Example EIS spectra of a silica-supported ionogel, showing the locations of the capacitive and resistive regimes, as well as the transition between the two and the location of the switching speed. Panel (a) shows the magnitude of complex impedance, while panel (b) shows the absolute value of the phase angle. The x-axis, showing the frequency of the AC voltage signal, is the same for both panels.

At low frequencies, the ions have sufficient time to form full EDLs, and capacitive behavior dominates.<sup>10</sup> The phase angle approaches  $-90^\circ$  and the impedance becomes strongly frequency-dependent. The capacitance can be calculated as:

$$(2.8) \quad C = (2\pi f Z_{\text{Imaginary}} A)^{-1}$$

where  $Z_{\text{Imaginary}}$  is the value of the imaginary component of impedance at frequency  $f$  (in Hz).

There exists an intermediate frequency where the behavior of the test cell switches from being primarily resistive to being primarily capacitive. This point is defined as the frequency at which the phase angle has a value of  $-45^\circ$ , and is called the switching speed or turning frequency.<sup>10</sup> The inverse of the switching speed is a heuristic value that suggests the fastest possible cycling speed for the device to operate as a capacitor.

#### 2.4.2 Cyclic Voltammetry (CV)

During CV testing, a triangle wave voltage signal is applied to a test cell. The voltage sweeps at a specified rate ( $dV/dt$ ) from a minimum voltage to a maximum voltage and back. The absolute value of the scan rate is held constant for both sweep directions but the sign is changed. The current is measured and plotted versus the voltage. For an ideal capacitor, a CV test returns a rectangular pattern according to the formula:

$$(2.9) \quad I = C \cdot dV/dt$$

As such, the capacitance can be calculated as the quotient of the current and the scan rate.<sup>11</sup> For real ionogel systems, the current varies somewhat with the voltage; in particular, the shape of the scan tends to have a slight tilt and sawtooth tips tend to appear at the turnaround points due to the ionogel's resistance (Figure 2.6).

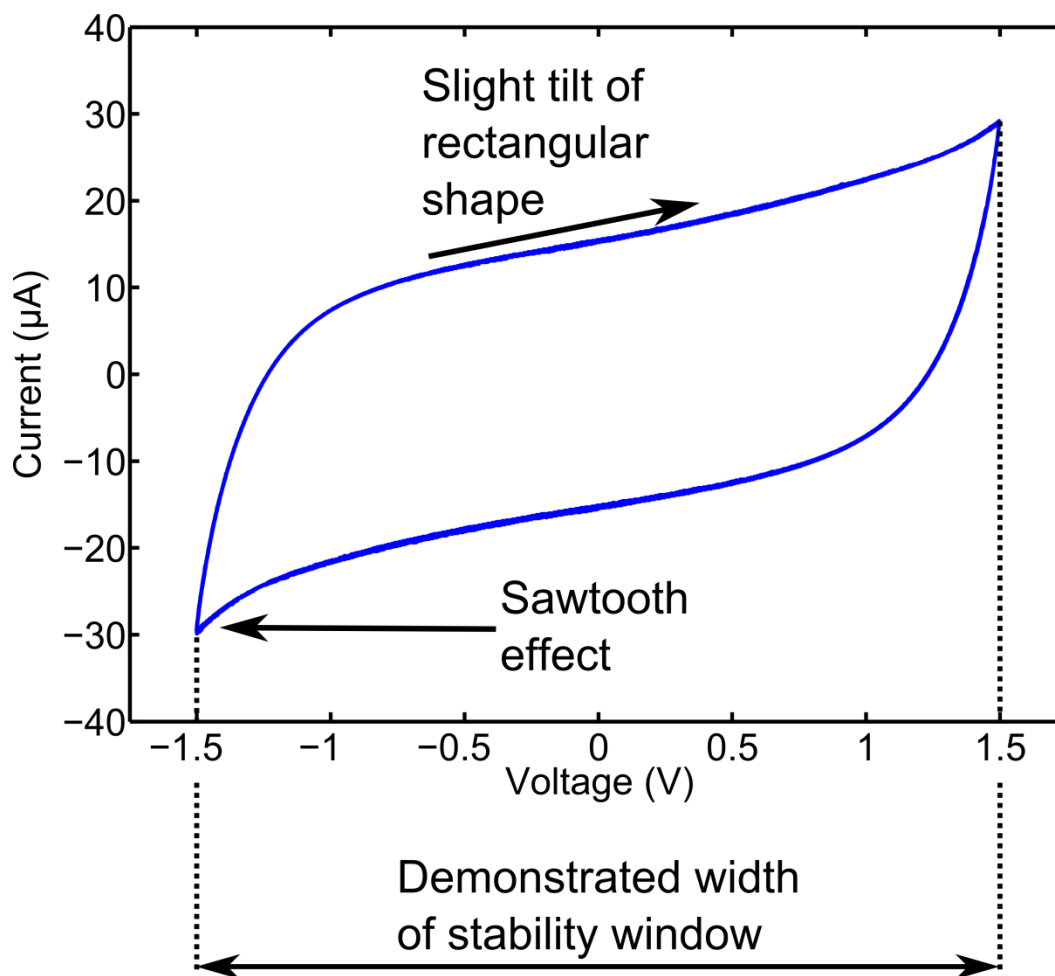


**Figure 2.6.** Cyclic voltammogram of EMI TFSI measured using graphene electrodes with a 0.1 V/s scan rate. The data has the characteristic rectangular shape of a capacitor but with some tilt and peaks at turnaround points due to the resistances of the device. A 3 V window of stability is demonstrated.

Voltammetric stability windows cannot be accurately ascertained with CV; this requires linear sweep voltammetry in a three-electrode system. However, CV can be used to demonstrate that the stability window of a material is at least as large as the difference between the minimum and maximum voltage if there are no peaks in the current that would indicate the presence of chemical reactions.

#### 2.4.3 Charge-Discharge

Charge-discharge testing is the means by which real-world usage of a device may be most closely approximated,<sup>12</sup> and as such is only appropriate for devices made with high surface area electrodes. In charge-discharge testing, a set current rather than a set voltage is supplied to the test cell, in contrast to EIS and CV. A positive current is supplied to the cell for a set amount of time, and the voltage measured as the device charges. The inverse current is then applied and the discharge voltage is monitored. The voltage signal takes the form of a triangle wave, often with a slight sawtooth effect in which there is a vertical drop in voltage upon the commencement of the discharge phase (Figure 2.7). The value of this “IR drop” divided by the current yields one measurement of the series resistance of the device. By taking the derivative of the discharge voltage, a value of  $dV/dt$  can be found, with which the capacitance of the device can be calculated using Eq. 2.9 above.



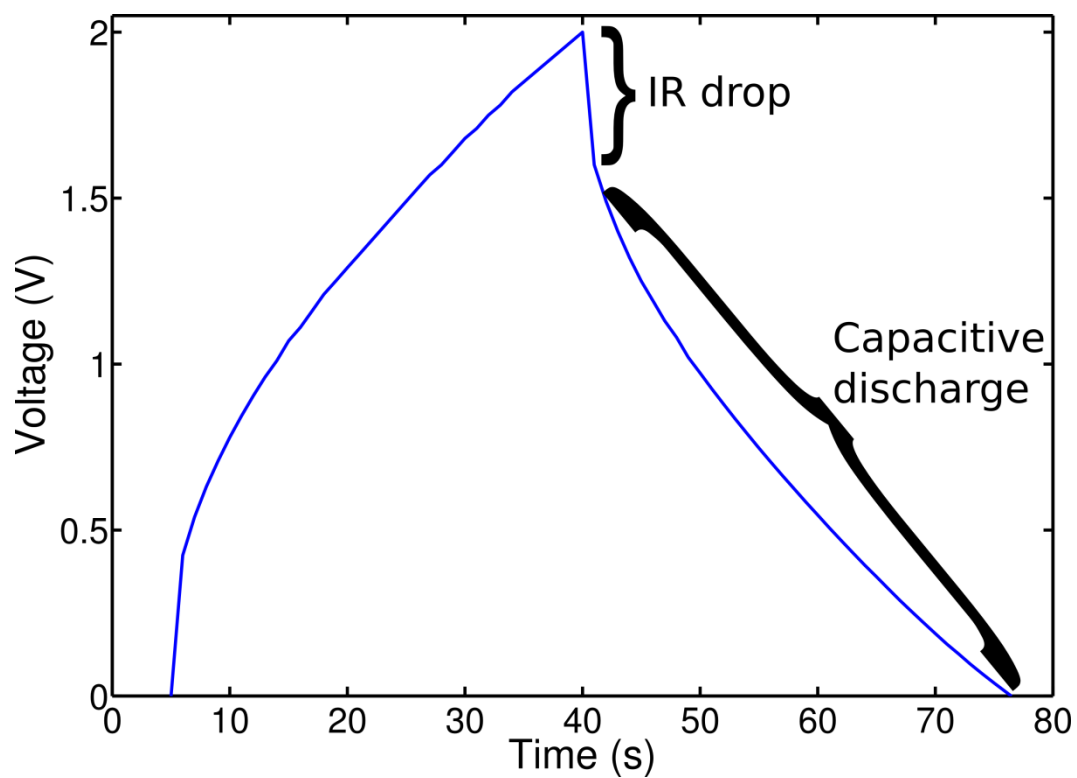


**Figure 2.7.** Example charge-discharge data for a silica-supported ionogel tested with laser-scribed graphene electrodes. During discharge, the immediate vertical drop in voltage (the IR drop) represents the series resistance of the device. Capacitive energy storage is discharged thereafter. Ideally, discharge is linear, whereas deviations from linearity indicate non-purely capacitive behavior.

Charge-discharge testing can also be used to determine the amount of energy and power stored in the device. The energy density of the device can be calculated as:

$$(2.10) \quad E = (CV^2)(2X)^{-1}$$

where  $X$  is some normalizing variable such as the electrode surface area, or the volume or mass of the device. The power can be calculated as:

$$(2.11) \quad P = (V^2)(4RX)^{-1}$$

where  $R$  is the series resistance as calculated from the IR drop. Charge-discharge data can be found in Chapter 6, which discusses devices made with silica-supported ionogels and laser-scribed graphene electrodes.

## 2.5 References

1. Martinelli, A. & Nordstierna, L. An investigation of the sol–gel process in ionic liquid–silica gels by time resolved Raman and  $^1\text{H}$  NMR spectroscopy. *Phys. Chem. Chem. Phys.* **14**, 13216 (2012).
2. Viau, L. *et al.* Ionic Liquid Mediated Sol-Gel Synthesis in the Presence of Water or Formic Acid: Which Synthesis for Which Material? *Chem. Mater.* **24**, 3128–3134 (2012).
3. Schick, H. L. A Thermodynamic Analysis of the High-temperature Vaporization Properties of Silica. *Chem. Rev.* **60**, 331–362 (1960).
4. Smith, B. C. *Fundamentals of Fourier transform infrared spectroscopy*. (CRC Press, 2011).
5. Robinson, J. W. *Undergraduate instrumental analysis*. (CRC Press, Taylor & Francis Group, 2014).
6. Bruttel, P. & Schlink, R. Water Determination by Karl Fischer Titration. *Metrohm Monogr.* **8.026.5013**, (2006).
7. Simon, P. & Gogotsi, Y. Materials for electrochemical capacitors. *Nat. Mater.* **7**, 845–854 (2008).
8. Barsoukov, E. & Macdonald, J. R. *Impedance spectroscopy: theory, experiment, and applications*. (2005).
9. Membreno, D., Smith, L., Shin, K.-S., Chui, C. O. & Dunn, B. A high-energy-density quasi-solid-state carbon nanotube electrochemical double-layer capacitor with ionogel electrolyte. *Transl. Mater. Res.* **2**, 015001 (2015).

10. Conway, B. E. *Electrochemical Supercapacitors Scientific Fundamentals and Technological Applications*. (Springer US, 1999).
11. Conway, B. E. Transition from ‘Supercapacitor’ to ‘Battery’ Behavior in Electrochemical Energy Storage. *J. Electrochem. Soc.* **138**, 1539 (1991).
12. Burke, A. Ultracapacitors: why, how, and where is the technology. *J. Power Sources* **91**, 37–50 (2000).

## **Chapter 3**

### **High-performance, mechanically compliant silica-based ionogels for electrical energy storage applications**

#### **3.1 Introduction**

Electrochemical double layer capacitors, known colloquially as supercapacitors, have attracted interest for their potential applications in the increasingly important field of energy storage.<sup>1-8</sup> Supercapacitors employing carbon-based, high surface area electrodes and liquid electrolytes represent the state of technologies currently on the market. However, the use of a liquid electrolyte leads to a number of practical and environmental drawbacks. The rigid metal casing required for containment adds weight and restricts possible device geometries. The possibility of leakage is also a concern, as such electrolytes often employ materials that may be toxic and/or flammable.<sup>1</sup> The development of ionogels (ion gels), solid or semi-solid electrolytes based on the room temperature molten salts known as ionic liquids (ILs), may offer a way to avoid these problems.<sup>9-27</sup> Ionic liquids are nonflammable, and the gel scaffold serves both to constrain the liquid in a solid form, as well as to provide a physical barrier between the electrodes, thereby preventing short circuits. As a result, ionogel-based energy storage devices are expected to be safer, lighter, and more amenable to future flexible applications.

Ionogels can be fabricated using a variety of structural support materials, including polymers, colloidal particles, carbon nanotubes, and small organic

gelators.<sup>9</sup> To date, many efforts have focused on polymer-based systems that employ either self-assembly of block copolymers or *in situ* thermally- or UV-initiated radical polymerization.<sup>4,19–23</sup> Although these systems have the benefit of reliably producing free-standing and flexible gels, they often display lower thermal stability compared to the neat IL<sup>20</sup> and can present processing challenges. An alternative method of producing ionogels that relies on the room-temperature, one-pot sol-gel synthesis of a silica scaffold to immobilize the IL *in situ* was proposed by Néouze and colleagues.<sup>28–30</sup> This process exploits the reaction between a silica precursor, tetramethoxysilane (TMOS), and formic acid (FA) to generate the scaffold.<sup>31,32</sup> Although the ability of the sol-gel process to form novel silica structures has been explored,<sup>18,33,34</sup> the potential for silica-based ionogels to serve as high-performance solid electrolytes merits further investigation. The simplicity of the sol-gel approach and the mild conditions under which it takes place suggest that silica-based ionogels may be suitable for application in a wide variety of systems where *in situ* self-assembly is preferable to mechanical mixing of the IL with a structural support material.<sup>24–27</sup>

The present work describes the creation of a new class of silica-based ionogels, proceeding from novel reagent formulations with high IL content. The ionogels described herein offer numerous advantages, including high ionic liquid content, good electrical performance and stability, and mechanical pliability. In addition, their synthesis and processing are straightforward and can easily be applied to electrochemical double layer capacitor fabrication *in situ*.

## 3.2 Results and Discussion

### 3.2.1 Ionogel Physical Properties

An exploration of the ternary TMOS/FA/IL reactant system phase space was undertaken, with a particular emphasis on maximizing IL content in a silica-supported ionogel, as shown in Figure 3.1. In addition, the most IL-rich formulation reported to date in the literature (with reactant molar ratio 1:7.8:1 TMOS:FA:IL) was replicated.<sup>30</sup> Although several different ILs have been previously used to fabricate ionogels,<sup>29</sup> EMI TFSI was employed in this investigation for its high ionic conductivity and relative hydrophobicity. A range of gelation times were observed; lower IL-content ionogels no longer exhibited flowing behavior after 1-2 hours. Some “unsuccessful” gels were observed to no longer flow after being allowed to sit undisturbed for a week or more. Gelation time was observed to be a function both of TMOS:FA molar ratio, as previously reported,<sup>31</sup> and of overall IL content. There appears to be a limit of roughly 50 mole percent IL in the reactant mixture, above which all formulations were deemed unsuccessful (Figure 3.1a).

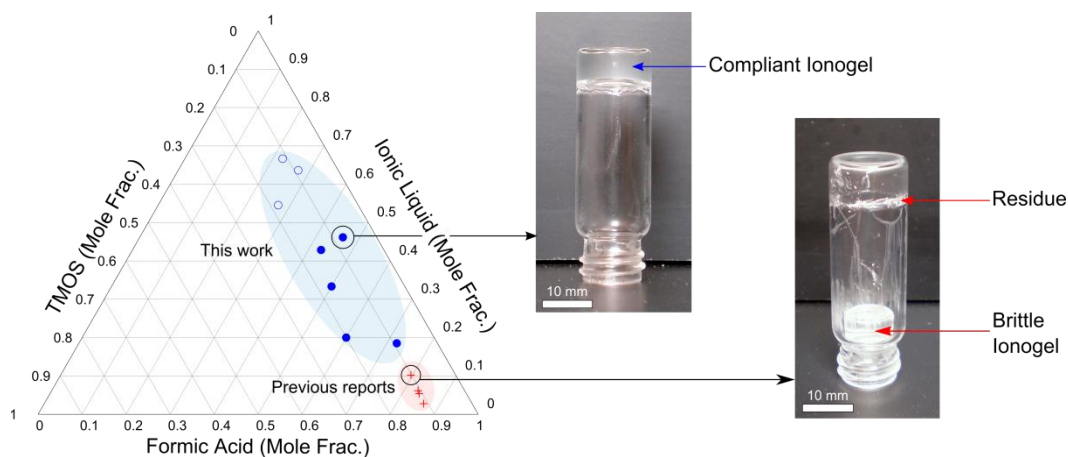


**Figure 3.1.** Overview of created ionogels. (a) Ternary phase diagram showing initial exploration of the tetramethoxysilane (TMOS)/formic acid/ionic liquid reactant mixture phase space by mole fraction. Formulations previously prepared in the literature<sup>28–30,32</sup> are shown as crosses. Circles represent formulations prepared by the authors in this work. Filled circles denote successful ionogels (gelation occurred within 24 hours); open circles designate formulations that failed to gel within 24 hours. Photographs display the two distinct types of ionogels created: (b) mechanically soft, IL-rich ionogel; (c) brittle, higher silica content ionogel, which has experienced significant volumetric shrinkage upon drying.



Formulations within a heretofore unexplored area of the TMOS/FA/IL phase space yielded a new class of ionic liquid-rich, mechanically-compliant silica-supported ionogels. One exemplar with high electrical performance (upper circled point in Figure 3.1a) was chosen for detailed investigation and comparison to the brittle, puck-like ionogels produced from the highest IL-content formulation reported previously (lower circled point in Figure 3.1a). These two specific ionogels are hereafter referred to as “compliant” and “brittle,” respectively. Silica scaffold contents for the brittle and compliant ionogels (which have the highest and lowest silica contents, respectively, of all formulations explored in this investigation) are displayed in Table 3.1.

As seen in Figure 3.1a, previous work has concentrated on silica-supported ionogel formulations with low ionic liquid content in the reactant mixture. Accordingly, the resultant ionic conductivity of these ionogels is uniformly lower than that of the neat ionic liquid.<sup>29</sup> Moreover, the large amounts of TMOS and FA initially present in such formulations lead to a significant drying period, as the sol-gel reaction produces numerous volatile side products, including water, methanol, and methyl formate.<sup>28,31</sup> The loss of these volatiles requires a drying period of several days in ambient laboratory conditions. The ionogel drying process leads to changes in ionogel composition over time. Under acidic conditions, the initial hydrolysis series of reactions is rapid, allowing the fast formation of the scaffold.<sup>35,36</sup> The condensation series of reactions, which strengthens the scaffold, is slow, leading to the observed drying period. These condensation reactions produce water and methanol that then evaporate

gradually.<sup>31</sup> Thermogravimetric analysis (TGA) was used to confirm that mass lost during the drying period was due to an evaporation of volatiles as opposed to loss of silica or IL content. When completed, the drying process reduced total volatiles content to less than 2% by mass.

Brittle ionogels lose almost half of their initial mass during drying, and roughly the same proportion of volume (Table 3.1). This severe volume loss, as shown in Figure 3.1c, can lead to a loss of contact with the reaction vessel. For *in situ* device formation, the electrode surfaces provide containment for the reagents as the ionogel forms. Ionogels that suffer significant shrinkage as they dry are unsuitable for these devices, because the retreat from the electrodes causes a loss of electrical contact, leading to significant degradation of device electrical properties as discussed below.

**Table 3.1.** Summary of ionogel physical properties. Silica scaffold content was determined using TGA; reported silica content is on a dry basis (calculated based on the mass remaining after the evaporation of volatiles below 200° C).

Ionogel Type:	Compliant	Brittle
Molar reactant ratio (TMOS:FA:IL)	1:6:6	1:7.8:1
Initial Mass% IL	84.6 ± 0.5	43.4 ± 0.5
Drying Process Losses:		
• Mass%	-11%	-48%
• Volume%	(negligible)	-53%
Final Mass% Silica Scaffold, Dry Basis	6.0 ± 0.9	15 ± 1
Young's Modulus	4.9 ± 0.2 kPa	1.0 ± 0.1 MPa

With substantially increased IL content, the new reactant combinations lead to easily-deformable, mechanically compliant ionogels. These IL-rich, compliant ionogels do not flow (Figure 3.1b), but deform readily in response to slight pressure. The Young's modulus of brittle ionogels is approximately two hundred times greater than that of compliant ionogels, leading to the difference in mechanical character between the two ionogels seen clearly in Figure 3.2. Both compliant and brittle ionogels are capable of being free-standing, and thus do not require rigid confinement. However, the soft and compliant behavior of IL-rich gels means that they may be suitable for a wider variety of device geometries, including flexible and/or stretchable devices. Moreover, compliant ionogels have the notable advantage of undergoing a shorter drying period (Appendix A, Figure A3).

The difference in percentage mass loss suffered by brittle ionogels as compared to compliant gels is dramatic (Table 3.1). Most notably, compliant ionogels have the considerable advantage of undergoing negligible volume change during drying. This volumetric stability makes them especially well-suited for *in situ* device formation, as the electrical contact between electrode and electrolyte is not damaged by gel shrinkage during drying.



**Figure 3.2.** Ionogel response to mechanical probing with a steel spatula. Brittle ionogels (right) are puck-like and fracture readily upon probing, while compliant ionogels (left) show softer, resilient behavior reminiscent of a jelly.

Final silica content is tunable to some degree (Figure 3.3), and multiple formulations leading to ionogels with compliant mechanical character have been identified. Based on our observations, ionogels start to transition from compliant to brittle character at approximately 8% scaffold content, although shrinkage into a brittle puck during drying is not observed until the ionogel contains greater than 9% silica by mass.

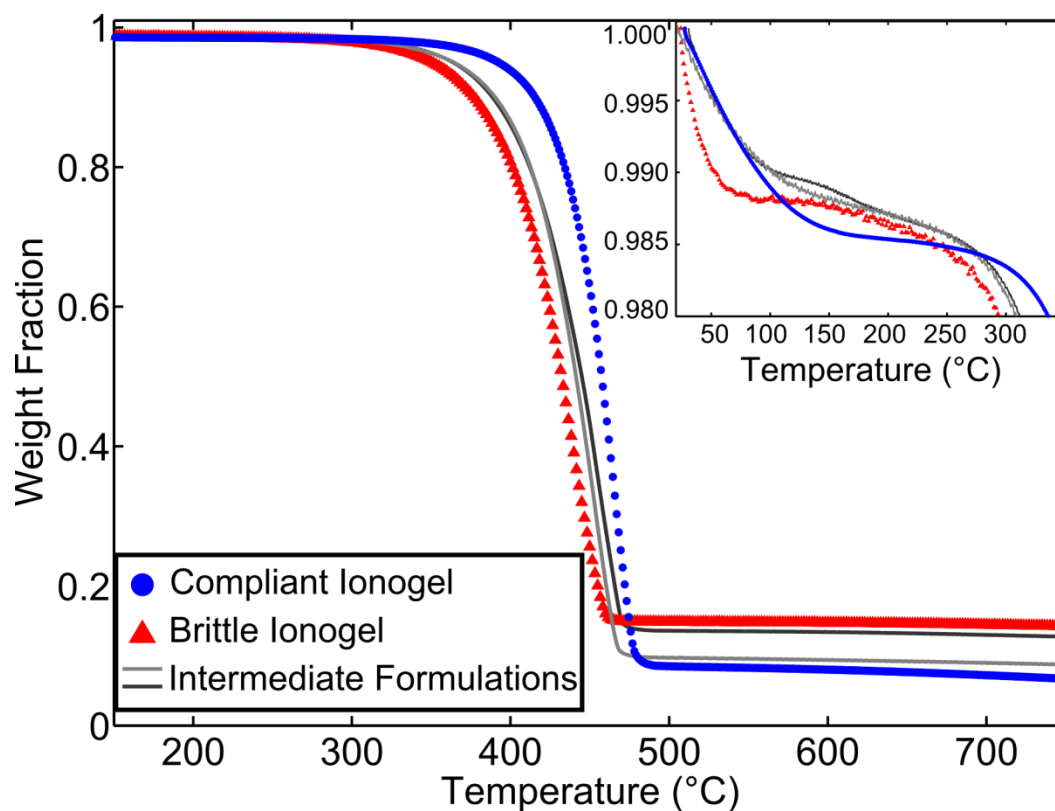


**Figure 3.3.** Thermogravimetric traces for several ionogels prepared using different reactant formulations. Inset shows an expanded view of the initial mass loss (of volatiles) at low temperatures. The intermediate formulations shown have silica contents of 8.2 and 10.6 percent by mass.

TGA was used to quantify the amount of silica scaffold material formed within in various ionogel formulations following gelation. Representative TGA spectra (Figure 3.3) show a slow loss of volatiles upon heating at low temperatures (less than 200° C) followed by a single major transition representing the decomposition of the IL beginning at approximately 300° C. The silica scaffold is left intact even after this transition. As such, a major advantage of silica-based ionogels is that the thermal stability of the gel electrolyte is limited only by that of the ionic liquid itself, as compared to polymer-based systems, where the thermal stability can be limited by degradation of the polymer.<sup>20</sup>

Notably, formulations leading to dramatically different mechanical and electrical characters do not possess drastically different silica contents. Successful formulations contained between approximately 6-15 mass percent silica scaffold. Final silica content alone was not predictive of whether or not a formulation would gel successfully; “failed” ionogel formulations were composed of between 3% and 7% silica by mass, a range that overlaps with that of the successful gels. This suggests that through slight reactant molar ratio changes, fine control may be exerted on final silica content and/or structure within the ionogel.



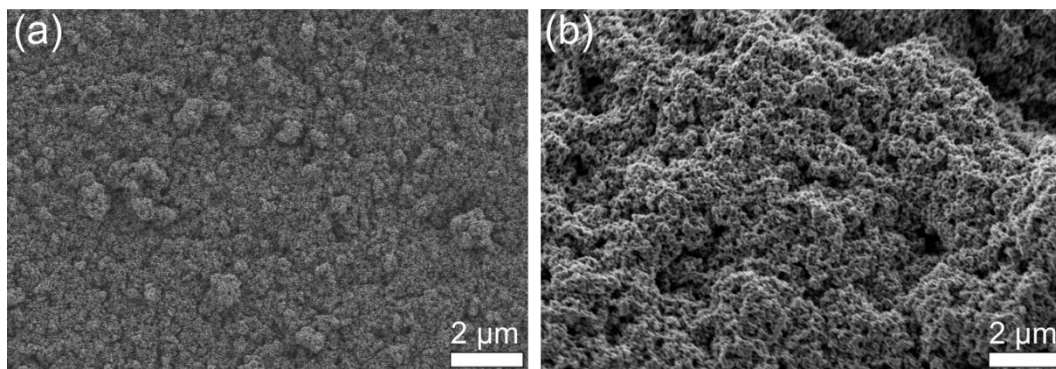


**Figure 3.4.** SEM images of (a) brittle and (b) compliant ionogel scaffolds. The ionic liquid was removed by aqueous extraction to reveal silica scaffold structure.

Differences in the silica scaffold microstructure between the brittle and compliant ionogels can be clearly seen in Figure 3.4, wherein the IL was removed from each sample by extraction with water.<sup>30</sup> The general structure of both scaffolds is characteristic of sol-gel reactions,<sup>32</sup> however the characteristic particle size of the silica network appears to be strongly formulation-dependent. The aggregates of sol particles that form the scaffold microstructure are visible in Figure 3.4, in which both brittle and compliant ionogels are shown at the same magnification. At the same scale, the brittle ionogel appears to exhibit a significantly smaller primary particle size. This suggests that in addition to overall silica content, the silica scaffold microstructure can also be varied by changing the initial reagent ratios.<sup>18</sup> The tunability of the silica particle size may allow IL-rich formulations of silica-based ionogels to be designed to interface optimally with a given high surface area electrode when formed *in situ* for energy storage devices. Whereas the pore structure of sol-gel silicas is important for many applications, in the case of supercapacitors it is of paramount importance to avoid blocking the *electrode* pores with silica particles and thereby reduce the effective electrode surface area available for energy storage.

### 3.2.2 Ionogel Electrical Properties

The electrical performance of ionogel thin films was characterized using AC impedance spectroscopy and cyclic voltammetry under ambient conditions. Table 3.2 includes the capacitance and ionic conductivity values for the compliant and brittle ionogels as well as the neat ionic liquid, which were determined using

impedance data. The 2.5 V width of the voltage sweep window, together with the TGA results (Figure 3. 3) that show that volatile species comprise less than 2% of dried ionogel mass, demonstrates that there is not enough residual water remaining from the scaffold synthesis (or absorbed from ambient water vapor) to significantly affect the electrical properties of these ionogels.

**Table 3.2.** Summary of ionogel electrical properties. Capacitance and ionic conductivity values were determined from impedance data using glassy carbon blocking electrodes. Ionic conductivity values were corrected to compensate for the resistance of the experimental setup ( $\sim 6 \text{ } \Omega$ , Appendix A, Figure A1). Capacitance values represent the performance of the two-electrode device as a whole, comprising two ionic double layers in series.

Ionogel Type:	Compliant	Brittle
Capacitance ( $\mu\text{F}/\text{cm}^2$ )		
• Ionogels	$7.5 \pm 0.4$	$2.0 \pm 0.1$
• Neat EMI TFSI	$7.7 \pm 0.4$	
Ionic Conductivity ( $\text{mS}/\text{cm}$ )		
• Ionogels	$9.3 \pm 0.5$	$0.0058 \pm 0.0003$
• Neat EMI TFSI	$10.9 \pm 0.5$	

Notably, the values of both ionic conductivity and capacitance of the compliant ionogel are comparable with those obtained for the neat ionic liquid. In the same experimental setup, neat EMI TFSI exhibited an ionic conductivity of  $10.9 \pm 0.5$  mS/cm and an overall capacitance (two double layers in series) of  $7.7 \pm 0.4$   $\mu\text{F}/\text{cm}^2$ , in agreement with previous reports.<sup>37</sup> Nearly equivalent electrical performance of the compliant ionogel and that of the neat IL demonstrates that the low silica content in the compliant ionogel formulation does not impede formation of the electric double layers, nor does it greatly interfere with motion of ions within the gel. In contrast, the ionic conductivity of the brittle ionogel is significantly lower than that of the neat IL. This lower ionic conductivity may be ascribed to a greater resistance to ionic diffusion due to the increased scaffold content as well as damaged electrical contact due to shrinkage. Similarly, the low overall capacitance shown by the brittle ionogel demonstrates the degradation of electrical performance caused by the loss of electrical contact during drying.

Figure 3.5 shows the magnitude of impedance vs. frequency and corresponding Nyquist plots for the compliant and brittle ionogels, as well as neat EMI TFSI. The shapes of the impedance spectra can yield information regarding the capacitive behavior of each ionogel as well as its maximum switching frequency. The compliant ionogel shows lower impedance generally, and its impedance response matches that of neat EMI TFSI much more closely than does that of the brittle ionogel (Figure 3.5a). The lower bulk ionic conductivity of the brittle ionogel can be clearly observed as a nearly three order of magnitude greater impedance at high frequencies compared to that of the compliant ionogel

and neat IL. The manifestation of capacitive behavior (strongly frequency-dependent impedance) on the part of the compliant ionogel occurs at a frequency within a factor of two of that of the neat IL at steady state, whereas the brittle ionogel does not start to exhibit capacitive behavior until frequencies lower by more than two orders of magnitude compared to the neat IL.

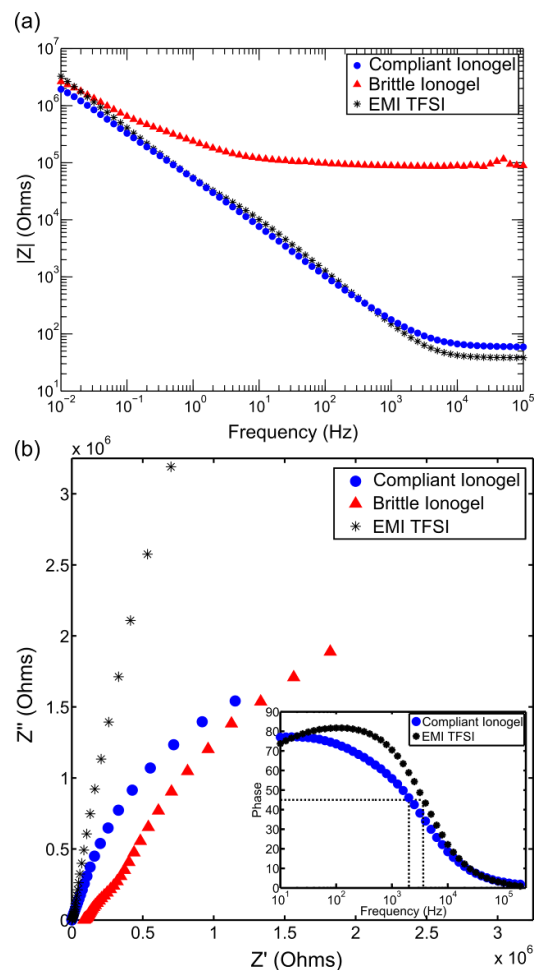


**Figure 3.5.** Impedance spectra for compliant and brittle ionogels. The neat EMI TFSI spectrum is also shown for comparison. (a) Magnitude of impedance. (b) Imaginary ( $Z''$ ) versus real ( $Z'$ ) components of impedance (Nyquist plot). The frequency range for the data shown is 0.01 Hz to 3 kHz. (inset) Phase angle of impedance for compliant ionogel and neat EMI TFSI. Onset of capacitive behavior (defined as occurring at a phase angle of  $-45^\circ$ ) is reached by the compliant ionogel at  $\sim 2100$  Hz, within a factor of two of neat EMI TFSI ( $\sim 3700$  Hz) as shown by the vertical dotted lines. The phase behavior of the brittle ionogel is not shown since the onset of capacitive behavior is significantly off-scale.

Compliant ionogels show clear capacitive response to a cycle of positive and negative linear voltage sweeps. As shown in Figure 3.6a, the current response is nearly rectangular and scales linearly with sweep rate. Capacitance values extracted from the cyclic voltammograms are comparable to those obtained using impedance data. Moreover, the 2.5 V sweep width is within the voltage stability window of the ionogel and clearly demonstrates that any residual volatile species or atmospheric moisture do not significantly impact device performance. While the ionogel current response shows some distortion at the extreme voltage points of each sweep, it is nearly the same as that of the neat IL (Figure 3.6b).



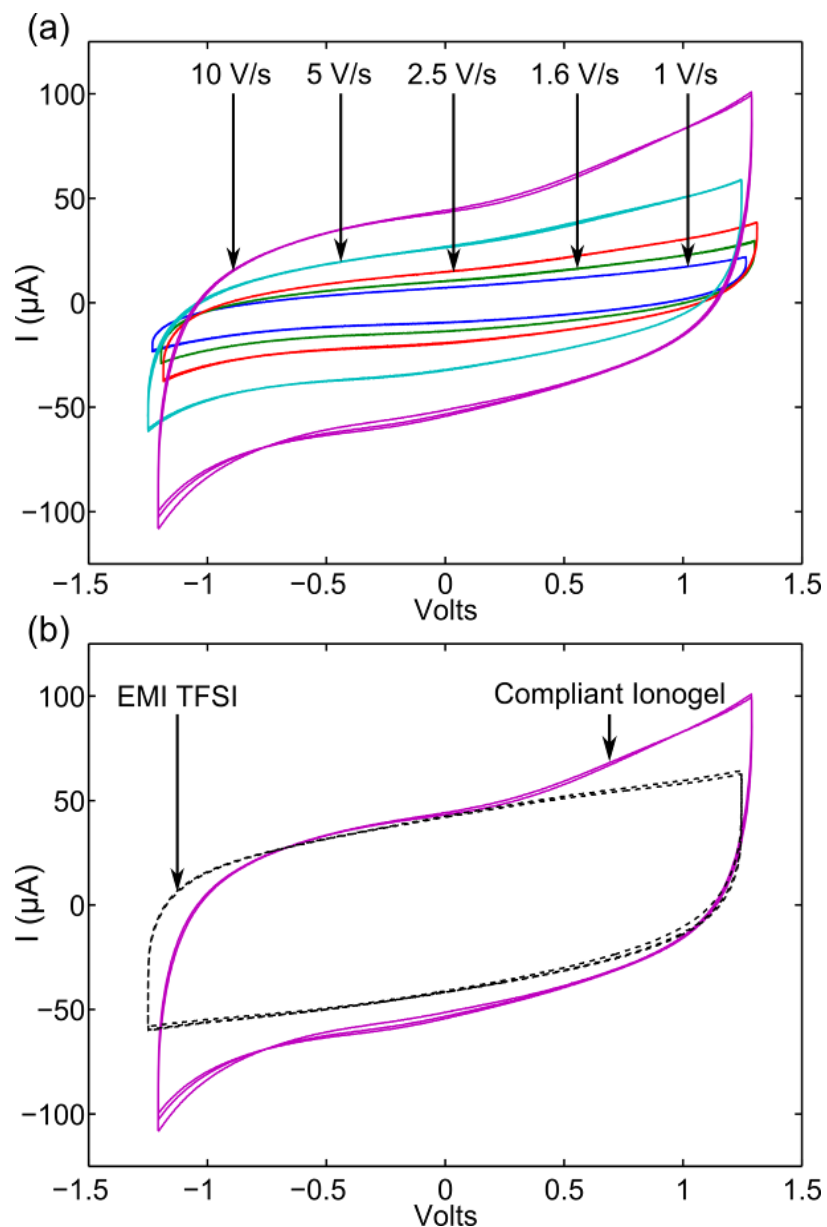


**Figure 3.6.** (a) Current response to cyclic voltage sweeps of the compliant ionogel at various sweep rates. Voltage was swept in the positive and negative directions successively three times at each sweep rate. The ionogel shows clear capacitive behavior, with roughly rectangular shape and linear scaling of current with sweep rate. (b) Current response of the compliant ionogel as compared to that of neat EMI TFSI at a sweep rate of 10 V/s.

### 3.3 Conclusion

The improved class of ionogel formulations described herein provides clear advantages in both the electrical and mechanical properties of *in situ*-formed silica-supported ionogels for flexible energy storage applications. Compliant ionogels retain greater dimensional stability during the sol-gel reaction byproduct drying period and exhibit superior electrical performance as a result. The high ionic liquid loading of these ionogels results in ionic conductivity and double layer capacitance values approximately equivalent to those of the neat IL. Their negligible volume loss and flexible mechanical character make them well-suited for *in situ* device fabrication, including thin film electrochemical double layer capacitors.

### 3.4 Experimental Materials and Methods

#### 3.4.1 Ionogel Preparation

Tetramethoxysilane (deposition grade, 98%) and formic acid (98%) were purchased from Sigma Aldrich. 1-ethyl-3-methylimidazolium bis(trifluoromethylsulfonyl)imide (EMI TFSI) was purchased from EMD Merck. All reagents were used as received.

Ionogel precursor solutions were mixed in glass vials. A particular ionogel reactant formulation was deemed “successful” if it gelled (*i.e.* showed no apparent flowing behavior) within 24 hours. The reaction was allowed to proceed spontaneously upon mixing of the reactants in a sealed vessel at ambient temperature without continuous agitation. Ionogel properties were in general repeatable over several trials. For bulk mass loss measurements, solutions were allowed to gel in a sealed vial overnight and then to dry uncovered. Samples prepared for mechanical and electrical characterization were injected into molds, which ensured good reproducibility. Initial ionogel volume was reproducible to within 5% error. Solutions were allowed to gel *in situ* overnight while sealed. Samples were unsealed the day after injection and ionogels were allowed to dry uncovered. The gelation and drying processes occurred at room temperature ( $\sim 22^{\circ}\text{C}$ ). Within the molds, typical drying periods observed for compliant and brittle puck-like ionogels were 12 and 15 days, respectively.

### 3.4.2 Physical Characterization

Thermogravimetric analysis (TGA) tests were conducted using a TA Instruments Q500 thermogravimetric analyzer with a ramp program. The initial temperature was ambient and the ramp terminated at 800° C; the ramp speed was 10° C/min. Volatile mass was defined as mass lost below 200° C. Silica scaffold mass was defined as mass remaining at 750° C. Ionic liquid mass was found by mass balance. Final ionogel composition was reproducible to within 10% error.

Cylindrical Teflon molds with a cross-sectional area of 0.32 cm<sup>2</sup> and thickness of 0.32 cm were used for mechanical analysis. Stress-strain tests were acquired by unconfined compression testing using an Instron 3366 testing frame with a 100 N load cell. The rate of strain applied was 0.1% strain per second to an upper limit of 40% strain. Young's moduli were determined using best-fit lines to the resulting stress-strain data from 15% to 20% strain, a regime in which both samples deformed elastically.

### 3.4.3 Electrical Characterization

To facilitate electrical characterization, precursor solutions were injected into molds consisting of a Teflon ring bounded by planar and smooth glassy carbon blocking electrodes, leading to an ionogel thickness of 0.16 cm and cross-sectional area of 0.32 cm<sup>2</sup>. AC impedance spectra and cyclic voltammograms were recorded using a VersaSTAT 3 potentiostat with a built-in frequency response analyzer (Princeton Applied Research). Spectra employed a 10 mV RMS oscillation around 0 V vs. open circuit. Impedance spectra were measured

periodically over the course of the drying process until ionogels reached steady state, as determined by stabilization of the ionogel electrical response. Final spectra were recorded on the 15<sup>th</sup> day after injection. The real component of complex impedance ( $Z'$ ) at high frequencies represents resistive character of the ionogel. Ionogel conductivity ( $\sigma$ ) was calculated using the formula:

$$(3.1) \quad \sigma = t (A Z')^{-1}$$

where  $t$  represents ionogel thickness,  $A$  represents the cross-sectional area of the planar electrodes, and  $Z'$  is the value of real impedance at a frequency near 100 kHz (where resistive behavior dominates).  $Z'$  values were corrected for setup resistance (Appendix A, Figure A1). Specific capacitance values for two-electrode structures were calculated using values of the imaginary component of impedance at low frequency:

$$(3.2) \quad C = (2\pi f A |Z''|)^{-1}$$

where  $Z''$  represents the imaginary component of the impedance at frequency  $f = 5$  Hz. At this frequency, all samples displayed predominantly capacitive behavior.

Cyclic voltammetry was performed with a 2.5 V window centered around 0 V relative to open circuit. Three cycles were performed sequentially to ensure reproducibility; the capacitor was discharged between tests at different voltage sweep rates.

### 3.5 References

Reprinted with permission from:

Horowitz, A. I. & Panzer, M. J. *J. Mater. Chem.*, **22**, 16534 – 16539 (2012).

Copyright The Royal Society of Chemistry, 2012.

1. Armand, M., Endres, F., MacFarlane, D. R., Ohno, H. & Scrosati, B. Ionic-liquid materials for the electrochemical challenges of the future. *Nat. Mater.* **8**, 621–629 (2009).
2. Conway, B. E. *Electrochemical Supercapacitors Scientific Fundamentals and Technological Applications*. (Springer US, 1999).
3. Lewandowski, A. & Galiński, M. Carbon–ionic liquid double-layer capacitors. *J. Phys. Chem. Solids* **65**, 281–286 (2004).
4. Stępiak, I. & Andrzejewska, E. Highly conductive ionic liquid based ternary polymer electrolytes obtained by in situ photopolymerisation. *Electrochimica Acta* **54**, 5660–5665 (2009).
5. Chen, Z. *et al.* High-Performance Supercapacitors Based on Hierarchically Porous Graphite Particles. *Adv. Energy Mater.* **1**, 551–556 (2011).
6. Futaba, D. N. *et al.* Shape-engineerable and highly densely packed single-walled carbon nanotubes and their application as super-capacitor electrodes. *Nat. Mater.* **5**, 987–994 (2006).
7. Frackowiak, E. Carbon materials for supercapacitor application. *Phys. Chem. Chem. Phys.* **9**, 1774 (2007).
8. Largeot, C. *et al.* Relation between the Ion Size and Pore Size for an Electric Double-Layer Capacitor. *J. Am. Chem. Soc.* **130**, 2730–2731 (2008).

9. Le Bideau, J., Viau, L. & Vioux, A. Ionogels, ionic liquid based hybrid materials. *Chem. Soc. Rev.* **40**, 907–925 (2011).
10. Visentin, A. F. & Panzer, M. J. Poly(Ethylene Glycol) Diacrylate-Supported Ionogels with Consistent Capacitive Behavior and Tunable Elastic Response. *ACS Appl. Mater. Interfaces* **4**, 2836–2839 (2012).
11. Ducros, J.-B., Buchtová, N., Magrez, A., Chauvet, O. & Le Bideau, J. Ionic and electronic conductivities in carbon nanotubes – ionogel solid device. *J. Mater. Chem.* **21**, 2508 (2011).
12. Kavanagh, A. *et al.* Photo-patternable hybrid ionogels for electrochromic applications. *J. Mater. Chem.* **21**, 8687 (2011).
13. Mizumo, T., Watanabe, T. & Ohno, H. Thermally Stable and Proton Conductive Ionogel Based on Brønsted Acidic Ionic Liquid with the Support of Silicate Network. *Polym. J.* **40**, 1099–1104 (2008).
14. Gayet, F. *et al.* Polymer nanocomposite ionogels, high-performance electrolyte membranes. *J. Mater. Chem.* **20**, 9456–9462 (2010).
15. Gayet, F. *et al.* Unique Combination of Mechanical Strength, Thermal Stability, and High Ion Conduction in PMMA–Silica Nanocomposites Containing High Loadings of Ionic Liquid. *Chem. Mater.* **21**, 5575–5577 (2009).
16. Yeon, S.-H., Kim, K.-S., Choi, S., Cha, J.-H. & Lee, H. Characterization of PVdF(HFP) Gel Electrolytes Based on 1-(2-Hydroxyethyl)-3-methyl Imidazolium Ionic Liquids. *J. Phys. Chem. B* **109**, 17928–17935 (2005).

17. Shin, J. Ionic liquids to the rescue? Overcoming the ionic conductivity limitations of polymer electrolytes. *Electrochem. Commun.* **5**, 1016–1020 (2003).
18. Le Bideau, J., Miah, M. Y., Vioux, A., Fajula, F. & Galarneau, A. Bimodal porous silica monoliths obtained by phase separation in non-aqueous media. *J. Mater. Chem.* **20**, 964–971 (2010).
19. Zhang, S., Lee, K. H., Frisbie, C. D. & Lodge, T. P. Ionic Conductivity, Capacitance, and Viscoelastic Properties of Block Copolymer-Based Ion Gels. *Macromolecules* **44**, 940–949 (2011).
20. Susan, M. A. B. H., Kaneko, T., Noda, A. & Watanabe, M. Ion Gels Prepared by in Situ Radical Polymerization of Vinyl Monomers in an Ionic Liquid and Their Characterization as Polymer Electrolytes. *J. Am. Chem. Soc.* **127**, 4976–4983 (2005).
21. Lee, K. H., Zhang, S., Lodge, T. P. & Frisbie, C. D. Electrical Impedance of Spin-Coatable Ion Gel Films. *J. Phys. Chem. B* **115**, 3315–3321 (2011).
22. He, Y., Boswell, P. G., Bühlmann, P. & Lodge, T. P. Ion Gels by Self-Assembly of a Triblock Copolymer in an Ionic Liquid <sup>†</sup>. *J. Phys. Chem. B* **111**, 4645–4652 (2007).
23. Patel, M., Gnanavel, M. & Bhattacharyya, A. J. Utilizing an ionic liquid for synthesizing a soft matter polymer ‘gel’ electrolyte for high rate capability lithium-ion batteries. *J. Mater. Chem.* **21**, 17419–17424 (2011).



24. Shimano, S., Zhou, H. & Honma, I. Preparation of Nanohybrid Solid-State Electrolytes with Liquidlike Mobilities by Solidifying Ionic Liquids with Silica Particles. *Chem. Mater.* **19**, 5216–5221 (2007).
25. Ueno, K., Fukai, T., Nagatsuka, T., Yasuda, T. & Watanabe, M. Solubility of Poly(methyl methacrylate) in Ionic Liquids in Relation to Solvent Parameters. *Langmuir* **30**, 3228–3235 (2014).
26. Ueno, K., Hata, K., Katakabe, T., Kondoh, M. & Watanabe, M. Nanocomposite Ion Gels Based on Silica Nanoparticles and an Ionic Liquid: Ionic Transport, Viscoelastic Properties, and Microstructure. *J. Phys. Chem. B* **112**, 9013–9019 (2008).
27. Ueno, K., Imaizumi, S., Hata, K. & Watanabe, M. Colloidal interaction in ionic liquids: Effects of ionic structures and surface chemistry on rheology of silica colloidal dispersions. *Langmuir* **25**, 825–831 (2008).
28. Néouze, M.-A., Bideau, J. L., Leroux, F. & Vioux, A. A route to heat resistant solid membranes with performances of liquid electrolytes. *Chem. Commun.* **41**, 1082–1084 (2005).
29. Néouze, M.-A., Le Bideau, J. & Vioux, A. Versatile heat resistant solid electrolytes with performances of liquid electrolytes. *Prog. Solid State Chem.* **33**, 217–222 (2005).
30. Néouze, M.-A., Bideau, J. L., Gaveau, P., Bellayer, S. & Vioux, A. Ionogels, New Materials Arising from the Confinement of Ionic Liquids within Silica-Derived Networks. *Chem. Mater.* **18**, 3931–3936 (2006).

31. Sharp, K. G. A two-component, non-aqueous route to silica gel. *J. Sol-Gel Sci. Technol.* **2**, 35–41 (1994).
32. Dai, S. *et al.* Preparation of silica aerogel using ionic liquids as solvents. *Chem. Commun.* **3**, 243–244 (2000).
33. Trilla, M., Cattoën, X., Blanc, C., Wong Chi Man, M. & Pleixats, R. Silica and hybrid silica hollow spheres from imidazolium-based templating agents. *J. Mater. Chem.* **21**, 1058–1063 (2011).
34. Klingshirn, M. A., Spear, S. K., Holbrey, J. D. & Rogers, R. D. Ionic liquids as solvent and solvent additives for the synthesis of sol–gel materials. *J. Mater. Chem.* **15**, 5174–5180 (2005).
35. Siouffi, A.-M. Silica gel-based monoliths prepared by the sol–gel method: facts and figures. *J. Chromatogr. A* **1000**, 801–818 (2003).
36. Klein, L. C. Sol-Gel Processing of Silicates. *Annu. Rev. Mater. Sci.* **15**, 227–248 (1985).
37. Galiński, M., Lewandowski, A. & Stępnia, I. Ionic liquids as electrolytes. *Electrochimica Acta* **51**, 5567–5580 (2006).

## Chapter 4

### The Variation of Silica-Supported Ionogel Properties with Reactive Formulation

#### 4.1 Introduction

Although the development of compliant silica-supported ionogels represents an important advance in achieving soft, thermally-stable electrolyte gels that can be processed *in situ*,<sup>1</sup> the formulation detailed in the previous chapter does have some important drawbacks. In particular, the gelation time is quite long, on the scale of hours. Although this may be desirable depending on the processing schema used to make solution-processed devices, it is also important to have a good grasp on what is possible within the phase space of the TMOS/FA/IL mixture. This allows for the potential of narrowly tailoring the formulation in order to achieve particular goals relating to ionogel processability or final properties.

The ternary diagram found in Chapter 3, Figure 3.1 gives a preliminary notion of the phase space; from this figure, it can be seen that there are limits outside of which gelation takes over 24 hours. However, this small amount of data alone is insufficient to answer important questions such as: is it possible to achieve a compliant ionogel with a short gelation time? What is the relationship between scaffold content and gelation time or between scaffold content and mechanical character? This chapter sets out to address these questions.

In addition to the two formulations detailed in Chapter 3, more than 20 further formulations were investigated. Silica content and gelation time were determined

for most samples. Gelation times were not precisely determined for formulations which took over twelve hours to gel. Elastic modulus was measured for a smaller subset of samples. Similarly, SEM imaging of scaffold morphology was performed for only a few samples. These data, taken as a whole, provide a strong understanding of how formulation may be adjusted to achieve an ionogel with a specified scaffold content, gelation time, mechanical character, or scaffold morphology.

## **4.2 Results and Discussion**

### **4.2.1 Variations in Gelation Time and Scaffold Content with Formulation**

Ionogel formulations were previously reported as a set of molar ratios of the form 1 mole TMOS:x moles FA:y moles IL. While this nomenclature is directly comparable with previous reports in the literature,<sup>2-5</sup> it is not the clearest way to describe the reactive formulations. As the IL serves only as a solvent and does not participate in the sol-gel network, the molar content of IL in the mixture is not a direct factor in the reaction. Rather, it is the relative concentration of reagents that affects the speed of the sol-gel reaction.<sup>6</sup> This concentration can be expressed by phrasing the formulation in terms of the volume percentage of the reactive mixture that is represented by the IL (assuming volumes are additive). The molar ratio of FA to TMOS, by contrast, directly relates the relative amounts of the two reagents in the most relevant terms, that of moles. As such, formulations can be well-represented by reporting this ratio and the volume percentage of IL. Using such a scheme, the compliant formulation detailed in the previous chapter, which

has a 6:1:6 molar ratio of FA:TMOS:IL, can also be referred to as a 6:1, 80% IL formulation.

Using this nomenclature, formulations can be represented on a simple cartesian coordinate system, with the ratio of FA to TMOS on the x-axis and the volume percentage of IL on the y-axis. Figure 4.1 shows a scatter plot of all tested formulations using this nomenclature. Two important sets of data are shown in this figure: first, points are color-coded to identify formulations that result in either brittle, single-monolith ionogels or in soft, compliant ionogels as well as formulations that took over 12 hours to gel. Second, points are sized relative to the mass percentage of silica in the final ionogel. Brittle ionogels were distinguished from compliant ionogels by their qualitative demonstration of cracking behavior as opposed to yielding to pressure.

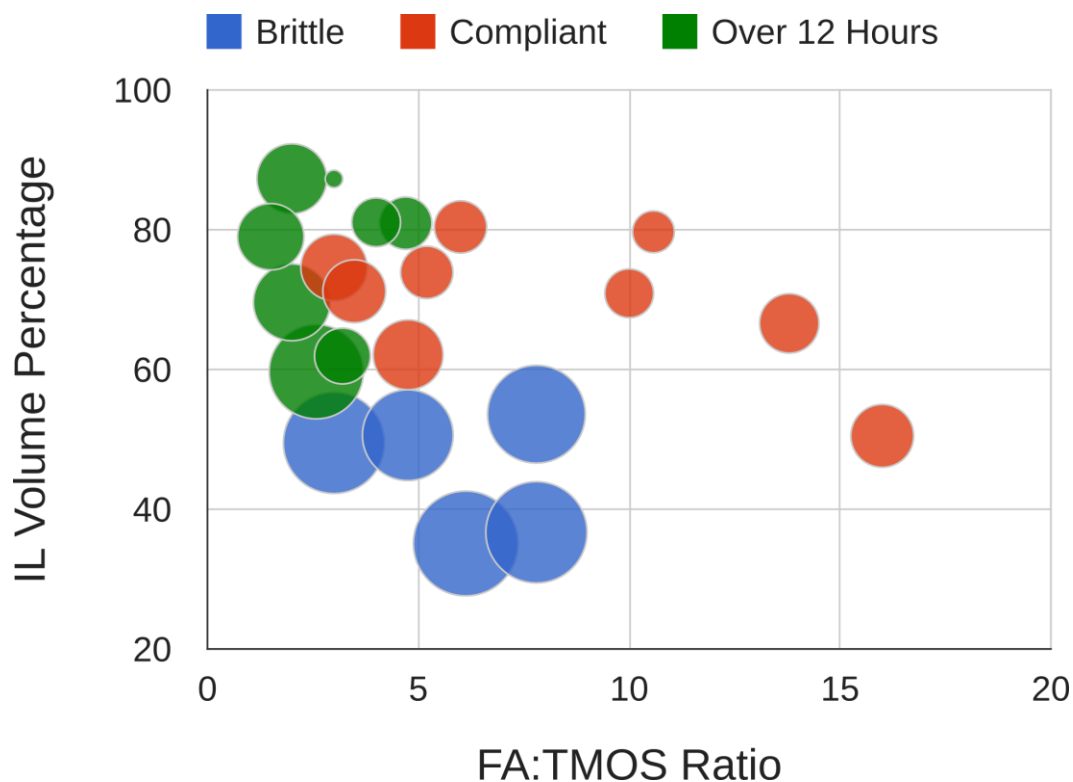


**Figure 4.1.** Scatter plot of tested formulations in the FA:TMOS, IL volume percentage phase space. Points are color-coded by the resultant ionogel. Red points represent compliant ionogels; blue points represent brittle ionogels; and green points represent formulations that did not gel within 12 hours. The size of points represents the mass percent of scaffold in the resultant ionogel (minimum = 2.9%; maximum = 16%). Brittle ionogels are produced when the FA:TMOS ratio is low and the overall reagent concentration is high (IL volume percentage is low). In other words, brittle ionogels, which have the highest silica contents, are produced when the highest proportions of TMOS are used in the reactive formulation. Compliant ionogels are produced by formulations with high IL contents, high FA:TMOS ratios, or both. Slow-gelling formulations are found when the reagent concentration and the FA:TMOS ratio are both low.

Unsurprisingly, brittle ionogels as a group have higher silica contents than compliant ionogels. The formulations which yield brittle monoliths are clustered in the lower left-hand corner, where the proportion of TMOS in the reactive formulation is the highest. The slowest gelation times are found when the IL content in the reactive mixture is high but the FA:TMOS ratio is low, resulting in both a slow reaction rate and a high diffusional barrier. Compliant ionogels can be achieved by using a small concentration of reagents (which translates to a large volume percentage of IL), or a large FA:TMOS ratio, or both.

Only by increasing the FA:TMOS ratio can rapidly-gelling compliant ionogels be achieved. A more detailed look at the gelation times can be found in Figure 4.2. Here, it can be seen that some formulations which result in compliant ionogels have gelation times that are comparably-rapid to those exhibited by most formulations resulting in brittle ionogels. Indeed, the most rapidly-gelling mixture of all tested formulations is a 16:1, 51% mixture, which results in a compliant ionogel with a 7% silica content after only 15 minutes. Again, it can be seen that increasing the proportion of IL or decreasing the proportion of FA both have the effect of increasing the gelation time. By using a very low proportion of FA to TMOS and a low IL content, formulations can be designed that will produce a brittle ionogel after a long gelation time. Such behavior may be desirable in order to obtain a rigid, crack-free ionogel.<sup>7</sup>

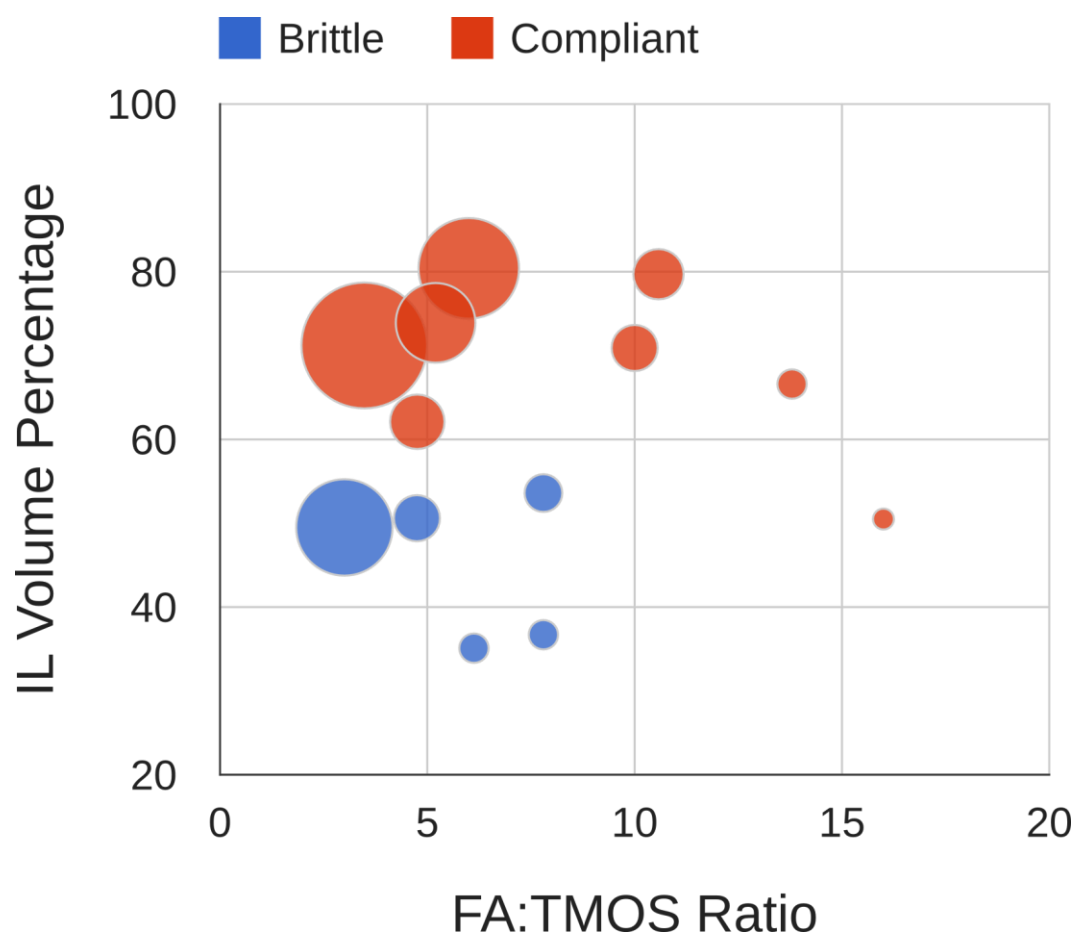


**Figure 4.2.** Scatter plot showing the gelation times of formulations which gelled within 12 hours. Red points represent formulations that result in compliant ionogels; blue points represent formulations that result in brittle ionogels. Points are sized relative to the gelation times for each formulation (minimum = 15 minutes; maximum = 9 hours). Gelation times increase as reagent concentration decreases (IL volume percentage increases) and as FA:TMOS ratio decreases.



#### 4.2.2 Variations in Mechanical Characteristics and Scaffold Morphology with Gelation Time

The elastic modulus was tested for several ionogels, with the results tabulated in Table 4.1. The moduli for the tested ionogels vary by two orders of magnitude between the maximum (almost 1 MPa) and minimum (approximately 9 kPa). As expected, the ionogels with higher silica contents have higher moduli in general. However, there is another, more interesting trend that can be gleaned from these results, namely that for comparable mass percentage of scaffold, ionogels with longer gelation times are stiffer. This trend is most notable when comparing the modulus of the ionogel made with formulation 16:1, 51% (19 kPa) with that of the ionogel made with formulation 3.5:1, 71% (160 kPa). The two ionogels have essentially identical scaffold contents, both approximately 7.5% silica by mass, but their moduli vary by an order of magnitude.

**Table 4.1.** Properties of selected ionogels, including formulation and elastic modulus. Elastic modulus tends to increase with silica content, but also is impacted by gelation time.

<b>FA:TMOS Molar Ratio</b>	<b>IL Volume %</b>	<b>Ionogel Type</b>	<b>Gelation Time (Hours)</b>	<b>Mass % of Silica in Ionogel</b>	<b>Elastic Modulus (kPa)</b>
10	70.9	Compliant	1.25	5.5	8.9
6	80.4	Compliant	6	6.0	19.2
16	50.5	Compliant	0.25	7.3	19.4
3.5	71.2	Compliant	9	7.5	157
7.8	36.7	Brittle	0.5	15.1	958

The reason for this disparity can be observed from the scaffold morphologies of these two formulations, as shown in Figure 4.3. For the rapidly-gelling formulation (Figure 4.3a), the scaffold has a relatively open pore structure, with significant void space. By contrast, the scaffold of the slower-gelling formulation (Figure 4.3b) has a very dense silica scaffold structure. This suggests that for slower-gelling formulations, the silica has time to grow into void spaces, providing enough structure to produce a stiff mechanical character, while rapidly-gelling formulations solidify before such reinforcing structures can be achieved.<sup>8</sup>

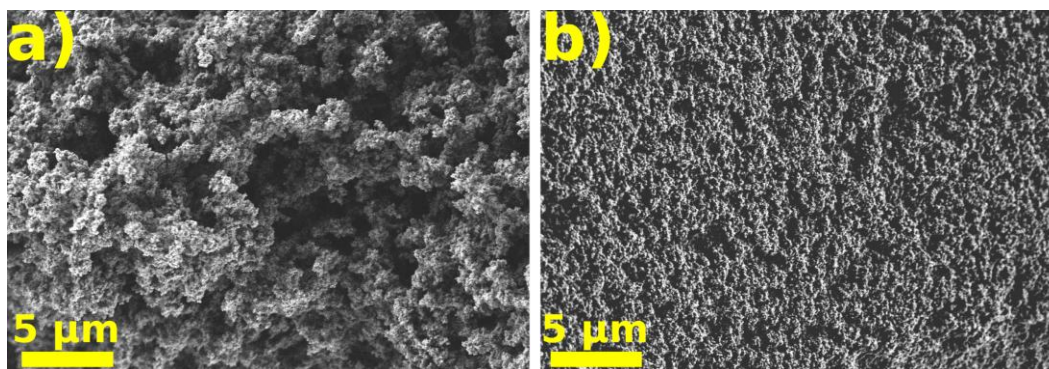


**Figure 4.3.** SEM images of silica scaffold morphology for two ionogels with the same silica content by mass (approximately 7.5%). a) Morphology of the silica scaffold of an ionogel made with the formulation 16:1 FA:TMOS by moles, 51% IL by volume. This formulation gels within 15 minutes after mixing and produces an ionogel with an elastic modulus of 19 kPa. The silica structure has significant void space. b) Morphology of the silica scaffold of an ionogel made with the formulation 3.5:1, FA:TMOS by moles, 71% IL by volume. This formulation requires nine hours after mixing to gel and produces an ionogel with an elastic modulus of 160 kPa, an order of magnitude higher than the rapidly-gelling, less-dense ionogel, due to its dense silica structure.

### **4.3 Conclusion**

The results here show conclusively that the sol-gel reaction is an incredibly versatile method for producing ionogels with a wide variety of properties. Both open and dense pore structures, stiff and soft mechanical characters, and rapid and gradual gelation can be achieved simply by varying the reactive formulation. These results can be best understood in using the nomenclature proposed here, where the FA:TMOS molar ratio is used in conjunction with the volume percentage of IL in the reaction mixture. These results were used to tailor formulations for varying applications in the chapters that follow.

## 4.4 Experimental Materials and Methods

### 4.4.1 Materials

EMI TFSI (synthesis grade) was obtained from EMD Merck. FA (98%) and TMOS (98%, deposition grade) were purchased from Sigma Aldrich. All chemicals were used as received.

### 4.4.2 Gelation Time Determination

Gelation times were tested by preparing 0.25 mL samples of precursor solution in a 1 dram vial. The vial was then mildly agitated or tilted every five minutes until flowing behavior was no longer observed. The first time point at which the sample did not flow was taken to be the gelation time.

### 4.4.3 Thermogravimetric Analysis

Silica contents were determined using thermogravimetric analysis. Samples were placed into a platinum sample pan and loaded into a TA Instruments Q500 thermogravimetric analyzer at ambient temperatures. The sample temperature was then raised to 800 °C at a ramp rate of 10 °C/minute under a nitrogen atmosphere. The mass loss experienced by the sample was recorded. The silica mass on a dry basis was calculated as the mass at 750 °C (after the decomposition of the IL) divided by the mass at 200 °C (after the evaporation of any adsorbed water or residual volatiles).

This same process was used to prepare silica scaffolds for SEM imaging as it effectively removes the IL from the ionogel.

#### 4.4.4 Mechanical Analysis

Elastic moduli were measured using a TA Instruments RSA-III dynamic mechanical analyzer. Ionogel samples were allowed to gel overnight in a PTFE cylinder bound by two PTFE plates to create pucks. Samples were left to dry in ambient conditions for at least two weeks before testing. Ionogel pucks were subjected to compressive stress-strain testing using a strain rate of 0.15 mm/s and a parallel-plate testing setup. Moduli were calculated by taking a linear regression of the stress-strain data between 15 and 20% strain.

## 4.5 References

1. Horowitz, A. I. & Panzer, M. J. High-performance, mechanically compliant silica-based ionogels for electrical energy storage applications. *J. Mater. Chem.* **22**, 16534–16539 (2012).
2. Dai, S. *et al.* Preparation of silica aerogel using ionic liquids as solvents. *Chem. Commun.* **3**, 243–244 (2000).
3. Néouze, M.-A., Le Bideau, J. & Vioux, A. Versatile heat resistant solid electrolytes with performances of liquid electrolytes. *Prog. Solid State Chem.* **33**, 217–222 (2005).
4. Néouze, M.-A., Bideau, J. L., Gaveau, P., Bellayer, S. & Vioux, A. Ionogels, New Materials Arising from the Confinement of Ionic Liquids within Silica-Derived Networks. *Chem. Mater.* **18**, 3931–3936 (2006).
5. Néouze, M.-A., Bideau, J. L., Leroux, F. & Vioux, A. A route to heat resistant solid membranes with performances of liquid electrolytes. *Chem. Commun.* **41**, 1082–1084 (2005).
6. Sharp, K. G. A two-component, non-aqueous route to silica gel. *J. Sol-Gel Sci. Technol.* **2**, 35–41 (1994).
7. Hench, L. L. & West, J. K. The sol-gel process. *Chem. Rev.* **90**, 33–72 (1990).
8. Martinelli, A. Effects of a Protic Ionic Liquid on the Reaction Pathway during Non-Aqueous Sol–Gel Synthesis of Silica: A Raman Spectroscopic Investigation. *Int. J. Mol. Sci.* **15**, 6488–6503 (2014).



## Chapter 5

### Spectroscopic Determination of Relative Brønsted Acidity as a Predictor of Reactivity in Aprotic Ionic Liquids

#### 5.1 Introduction

The nonvolatile room-temperature molten salts known as ionic liquids (ILs) offer a remarkable set of physiochemical properties and may represent safer alternatives to conventional volatile organic liquids, and as such have been the focus of intense research interest.<sup>1,2</sup> ILs have been demonstrated as attractive reaction media or enabling components for a wide variety of applications, including Suzuki reactions,<sup>3</sup> polymerizations,<sup>4</sup> acid scavenging (*e.g.* the BASIL™ process, patented by BASF<sup>5</sup>), the acid-catalyzed production of 1,4-dichlorobutane,<sup>6</sup> dissolution and processing of cellulose or chitin,<sup>7-9</sup> sol-gel reactions,<sup>10-12</sup> as well as being explored as catalysts in their own right<sup>13,14</sup> and as ionic conductors in solid electrolytes.<sup>15-19</sup> In recent years, commercialization of some of these processes has been initiated by major chemical companies as well as by new, IL-focused startups, with several pilot plants already constructed.<sup>20,21</sup>

A significant fraction of the applications of interest for ILs use them in combination with Brønsted acids, which may serve as catalysts or reagents. While there is a significant body of work concerning Brønsted acids in nonaqueous solvents,<sup>22-24</sup> the behavior of acids in ILs and how that behavior may vary with the identity of the acid and/or the IL has been difficult to predict. A rigorous theoretical understanding of the activity of an acidic proton in solution, or acidity

more generally, depends on a thorough description of the species present in that solution.<sup>25</sup> It has proven difficult to develop such descriptions for IL systems, especially as they depend strongly on the IL (see further discussion in Appendix B).<sup>26</sup> ILs themselves may display either Brønsted or Lewis acidic or basic character,<sup>27,28</sup> further complicating the story.<sup>26</sup>

As such, it is desirable to develop a tool for predicting the strength or reactivity of a Brønsted acid dissolved in an IL.<sup>29</sup> Attempts have been made to measure Hammett acidities in an IL medium,<sup>30,31</sup> but these acidities have been found to be indicator-dependent, suggesting that the theory behind the Hammett acidity is not valid for IL media.<sup>30</sup> Similarly, a technique designed to probe the interactions between an acid and an IL via protonated dyes has been utilized to determine Kamlet-Taft parameters of ILs.<sup>22,26–28</sup> However, while this method is useful for investigating the inherent properties of the ILs as solvents, it yields a relative ordering of acid dissociation in ILs that is determined by the specific dye used, but it does not offer predictions for the rates of acid-involving reactions of interest or a straightforward means rigorously comparing acid/IL pairs.<sup>32,33</sup> Moreover, all previous methods of investigating acids in ILs have required ILs of high purity and often optical clarity, as they are based on either NMR<sup>31</sup> or UV-vis spectroscopy.<sup>27,30</sup> Nor have such techniques been demonstrated to have predictive capabilities as applied to reactions of interest.

In this work, a simple spectroscopy-aided titration technique is introduced to probe relative acidities of solutions of Brønsted acids in aprotic ILs, yielding good predictive capability for relative acid-limited reaction rates in different IL

environments. A simple acid-base titration approach using pyridine as a FTIR-sensitive reporter/base is demonstrated to possess predictive power for determining the relative acidity of solutions of two different Brønsted acids, utilized for different reactions, within a series of three ILs that systematically vary in both cation and anion identities. Importantly, the results demonstrate that the acidities of these solutions and therefore apparent relative reaction rates of acid-involving reactions vary significantly in different ILs, in trends that depend on the acid identity as well as the identities of both the IL anion and cation.

## **5.2 Results and Discussion**

### **5.2.1 FTIR Titration Approach**

The details of the titration approach can be found in Section 5.4. Briefly, increasing amounts of an acid of interest are systematically added to an IL containing pyridine as an FTIR-active reporter. A set of common ILs combining the 1-ethyl-3-methylimidazolium (EMI) and 1-butyl-1-methylpyrrolidinium (BMP) cations with either the bis(trifluoromethylsulfonyl)imide (TFSI) or tris(perfluoroethyl)trifluorophosphate (FAP) anions, which vary in their physical properties (Appendix B, Table B1), was used in this study. ILs commonly possess various hydrocarbon structures on their cations and are therefore very IR-active (Figure 5.1a). An appropriate reporter molecule for FTIR studies with ILs would offer several strong, distinct signals that transition with solution acidity. Pyridine ( $pK_a$  in water = 5.25) is ideal for this purpose, as it displays several

peaks that undergo significant changes in intensity (appearing or disappearing gradually) with greater acid concentrations. Two vibrational modes, the symmetric and asymmetric ring stretching  $\nu_{19a}$  and  $\nu_{19b}$  peaks, provide the primary signals that are useful for quantitative analysis. The peak corresponding to  $\nu_{19b}$  (hereafter referred to as the “free pyridine peak”) is located at  $\sim 1440\text{ cm}^{-1}$  in pure pyridine<sup>34,35</sup> and is very strong. This peak is observed to disappear in solutions with high Brønsted acid contents.<sup>36</sup> For pyridinium, the  $\nu_{19b}$  peak is found at  $\sim 1540\text{ cm}^{-1}$ .<sup>37</sup> Meanwhile, the  $\nu_{19a}$  peak of pure pyridine located at  $\sim 1480\text{ cm}^{-1}$  is weaker, while the same vibrational mode produces a strong peak at  $\sim 1490\text{ cm}^{-1}$  for pyridinium-rich solutions. The exact position of the free pyridine peak (Figure 5.1b) reflects the polarity of the IL. In EMI FAP, the most Lewis acidic of the three ILs used here,<sup>22,38</sup> the free pyridine peak is shifted by the greatest degree to a higher wavenumber.

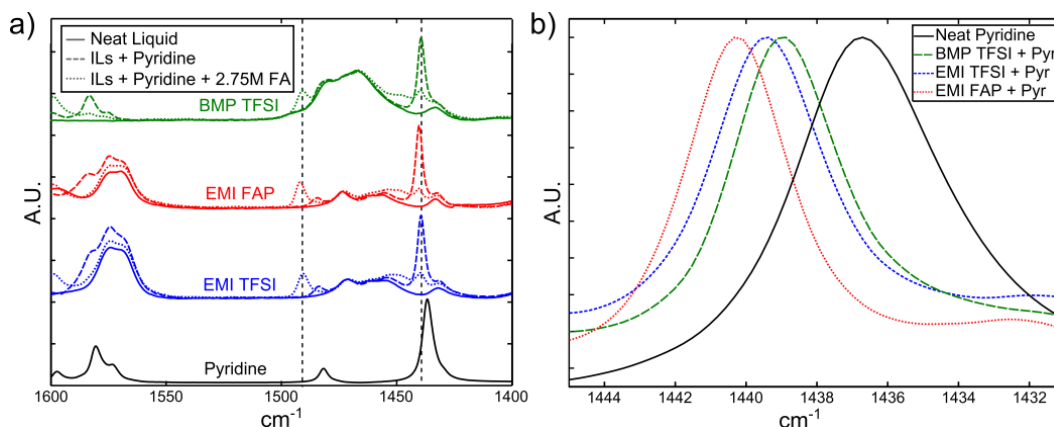


**Figure 5.1.** Relevant FTIR peaks for titration studies. a) An overview of the relevant FTIR spectral region for pyridine and the ILs used in this investigation. Neat IL spectra (solid lines) are overlaid with the spectra of a pyridine/IL solution (1:5 v/v, dashed lines) and a solution of 2.75 M formic acid (FA) in the IL/pyridine mixture (dotted lines). Some features from the pyridine spectrum are visible in the IL/pyridine mixture spectra, notably, the peak at  $\sim 1440\text{ cm}^{-1}$ , representing the  $\nu_{19b}$  mode of pyridine. This peak, along with the position of one of the peaks indicating the presence of pyridinium (the  $\nu_{19a}$  mode at  $\sim 1490\text{ cm}^{-1}$ ), has been marked with a vertical dashed line. b) FTIR spectral positions of the  $\nu_{19b}$  peak for neat pyridine, as well as for 1:5 (v/v) solutions in the different ILs. The shift in this peak to higher wavenumber is due to the different inherent Lewis acidities of the ILs.

Ordering of the relative acidity of acid-in-IL solutions was performed by determining the acid concentration at which the free pyridine peak was no longer detectable in the IL/pyridine/acid mixture, denoted as the threshold molarity. Lower threshold molarity corresponds to higher relative acidity.

Figure 5.2 shows an example of the determination of the threshold molarity for formic acid (FA;  $pK_a = 3.8$  in water) in BMP TFSI (spectra for the other acid/IL systems are shown in Appendix B, Figure B1). The free pyridine peak is observed to disappear as the FA concentration is increased from 1.4 M to 4.9 M (Figure 5.2a). The loss of the peak can be localized to a narrower concentration range (Figure 5.2b). Numerical derivatives of the FTIR spectra are used to quantitatively define the threshold molarity as the acid concentration at which the derivative no longer exhibits a zero crossing in this region (Figure 5.2c; Appendix B, Figure B2). Using this method facilitates an objective, reproducible determination of the relative acidities of solutions of different acids in ILs.

Depending on the details of the FTIR spectrum of a particular IL of interest, the pyridinium peaks mentioned above may also be used for quantitative analysis (Appendix B, Figure B3). Here, the derivative would be used to determine when a pyridinium peak first appears, rather than when the free pyridine peak disappears. One potential advantage of using the free pyridine peak, however, is that it may theoretically be used to calculate the percentage dissociated of the acid of interest, as the free pyridine peak will no longer appear when all of the available pyridine has reacted with the Brønsted acid. In order to obtain a rigorous determination of the true disappearance of the free pyridine peak, however, it is likely that a

spectral deconvolution must be performed. This is not necessary for the FTIR results to have predictive value, but may be of interest for future investigations.

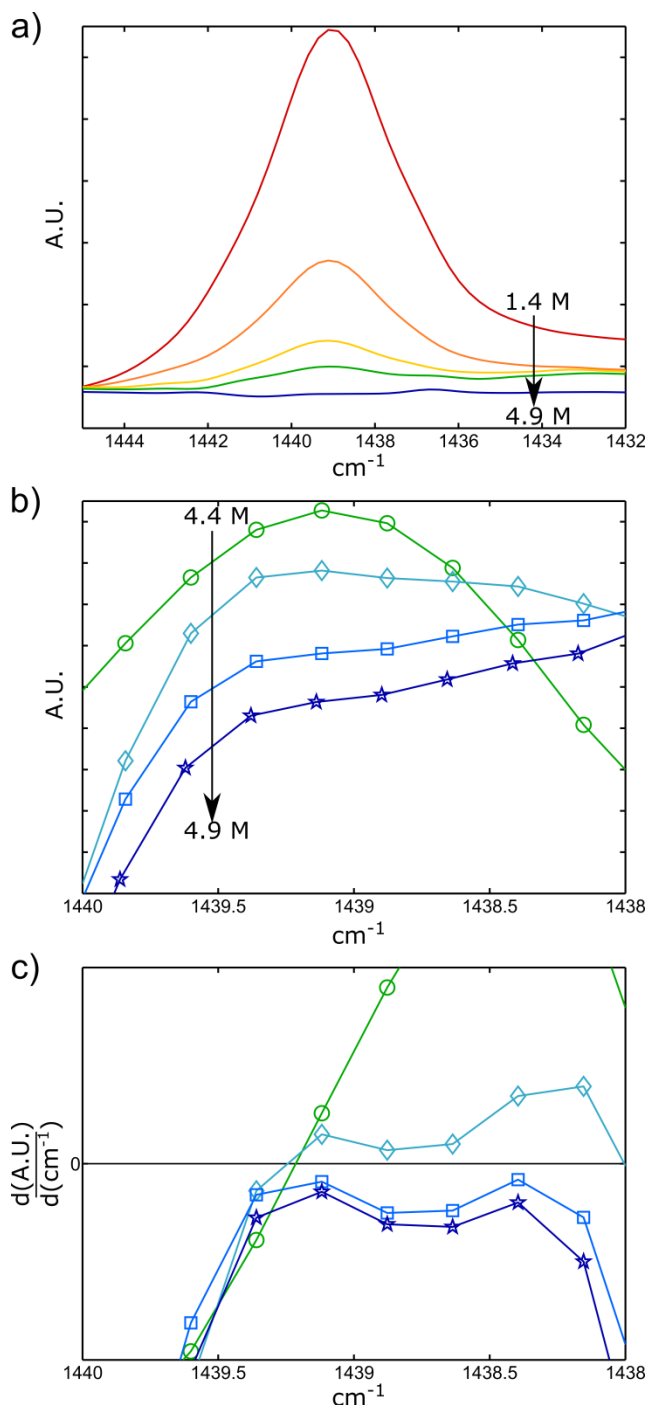


**Figure 5.2.** Example titration results showing the disappearance of the free pyridine peak with increasing formic acid concentration in BMP TFSI. a) The free pyridine peak disappears as more FA is added to the solution (arrow denotes increasing FA; the spectra shown are for 1.4 M, 2.7 M, 3.9 M, 4.4 M, and 4.9 M acid concentrations). b) Zoomed-in view near the free pyridine peak showing smaller acid molarity steps and the disappearance of the free pyridine peak between 4.4 M and 4.9 M FA. The two

intermediate spectra correspond to 4.6 M and 4.8 M FA concentrations. c) Taking the numerical derivative of the spectra shown in panel b facilitates a quantitative determination of when the peak disappears (no zero crossing); here, there is no peak starting at a 4.8 M FA solution (open square symbols).



### 5.2.2. Reaction Results

Two different reactions were used to demonstrate the predictive capability of acid titration using a pyridine probe (Figure 5.3). For both reactions, there is a Brønsted acid participant that exerts a strong effect on the reaction rate. The first reaction examined was the non-hydrolytic, acid-catalyzed sol-gel reaction of tetramethoxysilane (TMOS) and FA, which produces solid silica<sup>39</sup> to create intricate silica nanostructures and/or to encapsulate the IL into an “ionogel” form for use as a solid electrolyte or other functional material.<sup>15,16</sup> In this investigation, ionogels were produced using the three different ILs; two distinct formulations (FA/TMOS/IL ratio) were used, which varied in their FA content.

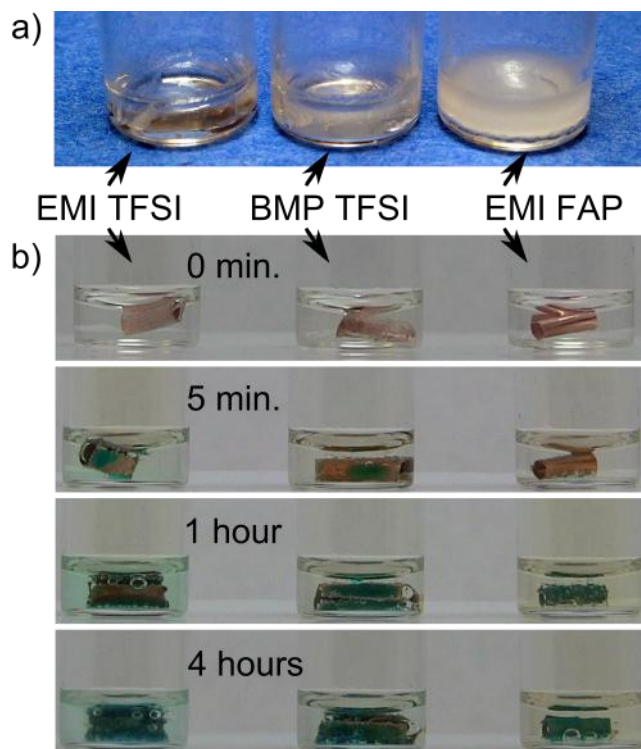


**Figure 5.3.** Photographs of reaction products in different ILs. a) Photograph of sol-gel silica-supported ionogels created with a low FA formulation in EMI TFSI, BMP TFSI, and EMI FAP. b) Time-lapse photographs of metallic copper sheets etched in  $\text{HNO}_3$ -in-IL solutions of EMI TFSI, BMP TFSI, and EMI FAP. The copper is etched most rapidly in the EMI TFSI and least rapidly in the EMI FAP.

The resultant ionogels (Figure 5.3a) exhibited obvious differences in their appearance, as well as notable variation in their gel times for a given formulation (Table 5.1). The low-FA gel formed in EMI TFSI is optically clear but has several fissures, suggesting significant stresses were exerted on the scaffold due to volatilization of reaction byproducts.<sup>15,39</sup> The gel formed in BMP TFSI is cloudier while the gel formed in EMI FAP is opaque and shows no apparent cracking or shrinkage. Some of these differences may be ascribed to changes in the gel microstructure (Appendix B, Figure B4), which is known to be a result of the patterning effect of different ions.<sup>12</sup> The gel time, which was previously shown to be highly dependent on acid content, may be used as a proxy for the reaction rate of the sol-gel reaction.<sup>39</sup> The clear differences in gelation time observed therefore indicate varying degrees of relative acidity in each IL.

In order to verify the predictive value of the titration technique, copper etching by nitric acid ( $\text{pK}_a = -1.3$  in water) was also investigated:



The etching rate varies across the different ILs, as observed in the photographic time series shown in Figure 5.3b. Copper nitrate (blue color) forms on the surface of the copper metal sheet in EMI TFSI within five minutes of immersion, with the sample in BMP TFSI following soon afterward. Meanwhile, negligible signs of reaction are observed for the sample in EMI FAP. After one hour, the sample in EMI TFSI is visibly corroded, the IL itself has taken on a blue tint, and the brown hue of  $\text{NO}_2$  gas can be seen in the headspace of the vial above the IL. At this time, corrosion is just beginning to visibly proceed on the sample in EMI FAP. After

four hours, the samples in EMI TFSI and BMP TFSI are largely corroded, while some bare copper can still be observed for the sample in EMI FAP, demonstrating the clear variation in reaction rate within the different ILs.

Table 5.1 summarizes the key findings of this study: namely, that the apparent rates of the two reactions vary significantly in the different ILs and that the variations observed in these rates correlate well with the threshold molarity trend (an indicator of relative acidity) determined by FTIR-enabled titration in each IL. The disappearance of the free pyridine peak with increasing formic acid (FA) concentration occurs in the order: EMI FAP < BMP TFSI < EMI TFSI, signifying that FA is most available to react in EMI FAP. This trend is identical to the order of the gel times (a proxy for reaction rate) required when performing the silica-forming sol-gel reaction with both high- and low-FA formulations in these ILs; gelation was most rapid in EMI FAP and slowest in EMI TFSI. By contrast, the threshold molarity needed to produce the disappearance of the free pyridine peak when titrating with  $\text{HNO}_3$  occurs in the reverse order: EMI TFSI < BMP TFSI < EMI FAP, indicating that  $\text{HNO}_3$  is most available to react in EMI TFSI. This trend is reflected in the fraction of copper etched by the  $\text{HNO}_3$ -in-IL solutions after 24 hours, which ranged from 57.1% in EMI FAP to 87.5% in EMI TFSI. These results clearly demonstrate that the titration technique has predictive value for reaction rates involving different acids.

**Table 5.1.** FTIR titration and reaction rates summary.

Ionic Liquid	FA Threshold Molarity (M)	Gel Time (min)		HNO <sub>3</sub> Threshold Molarity (M)	% Cu Etched after 24 hr
		<i>High FA</i>	<i>Low FA</i>		
EMI TFSI	5.4	35 ± 5	190 ± 5	2.2	87.5 ± 0.5
BMP TFSI	4.8	25 ± 5	140 ± 5	2.3	73.5 ± 0.5
EMI FAP	4.0	15 ± 5	50 ± 5	2.6	57.0 ± 0.5

The relative reaction rates correlate only with the threshold molarities found for each acid across the different ILs, and not with any of the IL properties shown in Table B1. Importantly, they do not correlate with the observed shift of the free pyridine peak in the ILs, either (Figure 5.1b). This is noteworthy, as alternative methods of determining acidities in ILs have proposed an inherent ranking of the strength of different acids in ILs based on only interactions between the IL and a reporter molecule.<sup>27</sup> The present results demonstrate that such a ranking may not be reliable when considering a specific reaction. The power of the titration technique therefore lies in its ability to directly determine a relative ranking of the acidity of solutions of a Brønsted acid across different ILs.

The technique of pyridine titration with a Brønsted acid in ILs offers benefits for both practical and theoretical applications. A relative ordering of expected reaction rates can be obtained without actually having to perform an acid-driven reaction within several different ILs, which is an advantage for reactions that may be complex, time-consuming, or resource intensive. In addition, the very same acid stock solution can be used for both the titration experiments and the reaction of interest, eliminating possible complications such as the effects of water content in the acid or the IL because the same species are utilized in both situations. The results of this study also demonstrate that acidity in ILs is a function of both IL cation and anion identities, rather than being primarily due to the anion as previously argued.<sup>29,32</sup> This is an important insight, as it suggests that an acid dissolved in an IL is affected by a number of interactions, which include those between the conjugate base and the IL cation, in addition to those captured by the

Kamlet-Taft parameters as well as the affinity between the acidic proton and IL anion. The titration technique thus offers a potential platform for further investigations into understanding the mechanisms of acid dissociation and acidic reactions in ILs, supplementing those based on NMR,<sup>40</sup> modeling,<sup>41</sup> and voltammetric studies.<sup>42</sup>

### **5.3 Conclusion**

The experimental technique demonstrated here offers a simple but powerful spectroscopic tool for predicting the relative rates of Brønsted acid-dependent reactions in different ILs. This approach offers a window into the varying behavior of acids in ILs, and can serve as a straightforward IL screening method in a wide variety of emergent and industrially relevant applications. Importantly, the current results demonstrate that the reactive behavior of acids in ILs can vary widely and depends on the identities of both the cation and anion that comprise the IL, suggesting that there are complex interactions between the acidic proton(s), the conjugate base, and both constituent ions of the IL, thus opening the door to further theoretical and experimental studies.

## 5.4 Experimental Materials and Methods

### 5.4.1 Materials

Pyridine (ACS reagent grade, 99%), formic acid (98%), nitric acid (Fluka,  $\geq 69\%$ ), and TMOS (deposition grade, 98%) were purchased from Sigma Aldrich. 110 copper foil (99.9%) was purchased from McMaster-Carr. Synthesis-grade ionic liquids were purchased from EMD Merck. All chemicals were used as received.

### 5.4.2 FTIR-enabled Acid Titration of Pyridine-in-IL Solutions

Solutions containing pyridine in the IL with a 1:5 volume ratio were prepared. Pyridine is highly miscible with all of the ILs used in this study. To prepare each titration sample for FTIR spectroscopy, a measured amount of acid was added to 175  $\mu\text{L}$  of the pyridine-in-IL solution, thoroughly mixed, and allowed to sit for several hours to ensure equilibration between the acid and pyridine. In total, 29 microliter (approximately 360 micromoles) of pyridine were added to each sample. Samples were first prepared with increasing acid contents in 10  $\mu\text{L}$  increments, with between 0 – 100  $\mu\text{L}$  of the acid added. FTIR spectra of these samples were then measured to determine the approximate acid concentration range in which the free pyridine peak visually disappeared. Next, samples were prepared with increasing acid contents in 5  $\mu\text{L}$  increments within a 20 – 25  $\mu\text{L}$  range centered on the approximate transitional acid concentration, followed by samples with acid contents differing by 1  $\mu\text{L}$  in a further reduced 5 – 7  $\mu\text{L}$  range



to more precisely determine the threshold molarity. Samples were tested on either side of the identified ranges to ensure that the peak transition occurred reproducibly within this range. FTIR spectra were measured on a JASCO Corporation FT/IR-6200 by conducting 100 scans. The spectra shown in Figure 5.1a were baseline-corrected using a multi-point linear correction for display purposes. Numerical derivatives were performed on unprocessed spectra; these were performed in MATLAB® using the simple difference-based differential function.

#### 5.4.3 Ionogel Preparation and Determination of Gel Times

Ionogels were prepared as previously described.<sup>15</sup> Two precursor formulations were investigated, one containing a large excess of formic acid (FA), the other containing a lower amount of FA. The high FA formulation used in this study had a 13.8:1 molar ratio of FA:TMOS while the low FA formulation had a 4.8:1 FA:TMOS molar ratio. Both formulations initially contained 66% IL by volume, which was held constant for the different ILs to ensure that the gel times could be reasonably compared. To determine the gel time, samples were gently tilted every five minutes until no flow behavior was observed. Samples were allowed to dry uncovered for at least one week before being photographed or undergoing SEM sample preparation. The IL was removed from the silica scaffold for SEM imaging by heating the sample under nitrogen to ~700 °C until no further mass loss was observed.

#### 5.4.4 Copper Etching

Nitric acid-in-IL solutions were prepared by adding  $\text{HNO}_3$  stock solution to pure ILs to make solutions with 0.3 mL total volume. Samples were sealed, thoroughly mixed, and allowed to equilibrate. As water is both less dense than and immiscible with the hydrophobic ILs utilized in this study, the small amount of water introduced by the acid stock solution first formed a thin layer on top of the IL and then slowly evaporated into the headspace of the sealed vial; no final aqueous phase was observed after this step.

Pieces of copper foil (5 mm x 5 mm x 0.05 mm thick) were weighed before being submerged in the acid-in-IL solutions and allowed to react undisturbed overnight. After 24 hours, the copper pieces were removed, thoroughly rinsed with deionized water, dried under flowing nitrogen, and weighed again. The fraction of copper etched was calculated from the measured mass difference. Copper was present in molar excess to ensure that availability of the acid would be the limiting factor in the etching rate. The photos shown in Figure 5.3b were color-balanced to ensure comparability.

## 5.5 References

Reprinted (adapted) with permission from:

Horowitz, A. I., Arias, P., & Panzer, M. J. *Chem. Commun.*, **51**, 6651 – 6654 (2015).

Copyright The Royal Society of Chemistry, 2015.

1. Armand, M., Endres, F., MacFarlane, D. R., Ohno, H. & Scrosati, B. Ionic-liquid materials for the electrochemical challenges of the future. *Nat. Mater.* **8**, 621–629 (2009).
2. Earle, M. J. & Seddon, K. R. Ionic liquids. Green solvents for the future. *Pure Appl. Chem.* **72**, 1391–1398 (2000).
3. Mathews, C. J., Smith, P. J. & Welton, T. Palladium catalysed Suzuki cross-coupling reactions in ambient temperature ionic liquids. *Chem. Commun.* **14**, 1249–1250 (2000).
4. Jain, N., Kumar, A., Chauhan, S. & Chauhan, S. M. S. Chemical and biochemical transformations in ionic liquids. *Tetrahedron* **61**, 1015–1060 (2005).
5. Masse, M. *et al.* Method for the separation of acids from chemical reaction mixtures by means of ionic fluids.
6. Stegmann, V. & Massone, K. Method for producing haloalkanes from alcohols.
7. Sanderson, K. Lignocellulose: A chewy problem. *Nature* **474**, S12–S14 (2011).
8. Shill, K. *et al.* Ionic liquid pretreatment of cellulosic biomass: Enzymatic hydrolysis and ionic liquid recycle. *Biotechnol. Bioeng.* **108**, 511–520 (2011).

9. Qin, Y., Lu, X., Sun, N. & Rogers, R. D. Dissolution or extraction of crustacean shells using ionic liquids to obtain high molecular weight purified chitin and direct production of chitin films and fibers. *Green Chem.* **12**, 968–971 (2010).
10. Dai, S. *et al.* Preparation of silica aerogel using ionic liquids as solvents. *Chem. Commun.* **3**, 243–244 (2000).
11. Trilla, M., Cattoën, X., Blanc, C., Wong Chi Man, M. & Pleixats, R. Silica and hybrid silica hollow spheres from imidazolium-based templating agents. *J. Mater. Chem.* **21**, 1058–1063 (2011).
12. Zhou, Y., Schattka, J. H. & Antonietti, M. Room-Temperature Ionic Liquids as Template to Monolithic Mesoporous Silica with Wormlike Pores via a Sol–Gel Nanocasting Technique. *Nano Lett.* **4**, 477–481 (2004).
13. Welton, T. Ionic liquids in catalysis. *Coord. Chem. Rev.* **248**, 2459–2477 (2004).
14. Kim, D. W. & Chi, D. Y. Polymer-Supported Ionic Liquids: Imidazolium Salts as Catalysts for Nucleophilic Substitution Reactions Including Fluorinations. *Angew. Chem. Int. Ed.* **43**, 483–485 (2004).
15. Horowitz, A. I. & Panzer, M. J. High-performance, mechanically compliant silica-based ionogels for electrical energy storage applications. *J. Mater. Chem.* **22**, 16534–16539 (2012).
16. Le Bideau, J., Viau, L. & Vioux, A. Ionogels, ionic liquid based hybrid materials. *Chem. Soc. Rev.* **40**, 907–925 (2011).

17. Gu, Y. *et al.* High Toughness, High Conductivity Ion Gels by Sequential Triblock Copolymer Self-Assembly and Chemical Cross-Linking. *J. Am. Chem. Soc.* **135**, 9652–9655 (2013).
18. Wang, P., Zakeeruddin, S. M., Comte, P., Exnar, I. & Grätzel, M. Gelation of Ionic Liquid-Based Electrolytes with Silica Nanoparticles for Quasi-Solid-State Dye-Sensitized Solar Cells. *J. Am. Chem. Soc.* **125**, 1166–1167 (2003).
19. Susan, M. A. B. H., Kaneko, T., Noda, A. & Watanabe, M. Ion Gels Prepared by in Situ Radical Polymerization of Vinyl Monomers in an Ionic Liquid and Their Characterization as Polymer Electrolytes. *J. Am. Chem. Soc.* **127**, 4976–4983 (2005).
20. Seddon, K. R. Ionic liquids: A taste of the future. *Nat. Mater.* **2**, 363–365 (2003).
21. Plechkova, N. V. & Seddon, K. R. Applications of ionic liquids in the chemical industry. *Chem. Soc. Rev.* **37**, 123–150 (2008).
22. Reichardt, C. Polarity of ionic liquids determined empirically by means of solvatochromic pyridinium N-phenolate betaine dyes. *Green Chem.* **7**, 339–351 (2005).
23. Bordwell, F. G. Equilibrium acidities in dimethyl sulfoxide solution. *Acc. Chem. Res.* **21**, 456–463 (1988).
24. Popovych, O. & Bates, R. G. Estimation of Medium Effects for Single Ions in Non-Aqueous Solvents. *C R C Crit. Rev. Anal. Chem.* **1**, 73–117 (1970).

25. Mihichuk, L. M., Driver, G. W. & Johnson, K. E. Brønsted Acidity and the Medium: Fundamentals with a Focus on Ionic Liquids. *ChemPhysChem* **12**, 1622–1632 (2011).
26. Johnson, K. E., Pagni, R. M. & Bartmess, J. Brønsted Acids in Ionic Liquids: Fundamentals, Organic Reactions, and Comparisons. *Monatshefte Für Chem. - Chem. Mon.* **138**, 1077–1101 (2007).
27. MacFarlane, D. R., Pringle, J. M., Johansson, K. M., Forsyth, S. A. & Forsyth, M. Lewis base ionic liquids. *Chem. Commun.* **18**, 1905–1917 (2006).
28. Tokuda, H., Tsuzuki, S., Susan, M. A. B. H., Hayamizu, K. & Watanabe, M. How Ionic Are Room-Temperature Ionic Liquids? An Indicator of the Physicochemical Properties. *J. Phys. Chem. B* **110**, 19593–19600 (2006).
29. Thomazeau, C., Olivier-Bourbigou, H., Magna, L., Luts, S. & Gilbert, B. Determination of an acidic scale in room temperature ionic liquids. *J. Am. Chem. Soc.* **125**, 5264–5265 (2003).
30. Robert, T., Magna, L., Olivier-Bourbigou, H. & Gilbert, B. A Comparison of the Acidity Levels in Room-Temperature Ionic Liquids. *J. Electrochem. Soc.* **156**, F115 (2009).
31. Gräsvik, J., Hallett, J. P., To, T. Q. & Welton, T. A quick, simple, robust method to measure the acidity of ionic liquids. *Chem. Commun.* **50**, 7258–7261 (2014).
32. Cláudio, A. F. M. *et al.* Extended scale for the hydrogen-bond basicity of ionic liquids. *Phys. Chem. Chem. Phys.* **16**, 6593–6601 (2014).

33. Wasserscheid, P. & Keim, W. Ionic liquids-new ‘solutions’ for transition metal catalysis. *Angew. Chem.* **39**, 3772–3789 (2000).
34. Corrsin, L., Fax, B. J. & Lord, R. C. The Vibrational Spectra of Pyridine and Pyridine-d<sub>5</sub>. *J. Chem. Phys.* **21**, 1170–1176 (1953).
35. Wilmschurst, J. K. & Bernstein, H. J. The Vibrational Spectra of Pyridine, Pyridine-4-d, Pyridine-2,6-d<sub>2</sub>, and Pyridine-3,5-d<sub>2</sub>. *Can. J. Chem.* **35**, 1183–1194 (1957).
36. Yang, Y. & Kou, Y. Determination of the Lewis acidity of ionic liquids by means of an IR spectroscopic probe. *Chem. Commun.* **2**, 226–227 (2004).
37. Cook, D. Vibrational Spectra of Pyridinium Salts. *Can. J. Chem.* **39**, 2009–2024 (1961).
38. Spange, S., Lungwitz, R. & Schade, A. Correlation of molecular structure and polarity of ionic liquids. *J. Mol. Liq.* **192**, 137–143 (2014).
39. Sharp, K. G. A two-component, non-aqueous route to silica gel. *J. Sol-Gel Sci. Technol.* **2**, 35–41 (1994).
40. Trulove, P. C. & Osteryoung, R. A. Proton speciation in ambient-temperature chloroaluminate ionic liquids. *Inorg. Chem.* **31**, 3980–3985 (1992).
41. Del Pópolo, M. G., Kohanoff, J. & Lynden-Bell, R. M. Solvation Structure and Transport of Acidic Protons in Ionic Liquids: A First-principles Simulation Study. *J. Phys. Chem. B* **110**, 8798–8803 (2006).
42. Aldous, L. *et al.* Voltammetric Studies of Gold, Protons, and [HCl<sub>2</sub>]<sup>-</sup> in Ionic Liquids. *J. Phys. Chem. C* **111**, 8496–8503 (2007).

## **Chapter 6**

### **The Impact of Ionogel Casting Time on Silica Morphology and Supercapacitor Device Performance**

#### **6.1 Introduction**

A new class of hybrid materials known as “ionogels” has attracted strong interest from researchers in the field of electrochemical energy storage.<sup>1,2</sup> Ionogels combine ionic liquids (salts that are molten at room temperature) with a solid scaffold material to form an ionically-conductive solid or solid-like gel. These materials have great potential as components in electrochemical energy storage devices as they solve many of the problems presented by conventional electrolytes.<sup>2</sup> Most notably, they eliminate flammability-related concerns as ionic liquids (ILs) have negligible vapor pressure and therefore are not flammable. The utility of a gel form lies in minimizing device weight and reducing the need for containment layers. Since ionogels do not show flowing behavior, no heavy or rigid containment layer is needed to prevent electrolyte leakage. As a result, the use of ionogels has the potential to improve device energy and power densities and enable thin-film, flexible form factors.

Many solid materials have been investigated as possible scaffolds for ionogel systems. These have included organic gelators, polymers, and inorganic oxides, among others.<sup>1,3–18</sup> Inorganic oxides such as silica have proven to be an interesting choice as the support material for ionogel due to their extremely high thermal stabilities. The use of an inorganic oxide scaffold guarantees that the



thermal stability of the ionogel will be limited by the IL, rather than the scaffold as is the case for many polymer-supported systems.<sup>16</sup> The high thermal stability limits offered by inorganic oxides would constitute a significant improvement on the state of the art of energy storage, both improving current technologies and opening the door to new, high-temperature uses of energy storage.

There are two main ways to incorporate inorganic oxides into ILs to form an ionogel. The first is to simply mix a material such as fumed silica nanoparticles into the IL.<sup>9–11</sup> Although this is a very straightforward and facile method, it is *ex situ* (i.e., the ionogel cannot be formed in contact with the electrodes). *In situ* processability is advantageous from a scale-up perspective. In addition, *in situ* formation of ionogels is strongly preferable for applications in which an ionogel might be used in concert with a high-surface area electrode, as is the case in supercapacitor devices. Pore access is a significant concern in such devices, as the nano- or micro-scale pores in finely-structured electrodes can easily become blocked or may be inaccessible due to energetic barriers,<sup>19–23</sup> reducing the effective surface area of the electrode and therefore the energy storage potential of the device. When a liquid ionogel precursor is exposed to an electrode before undergoing gelation, better pore utilization may be expected as compared to the “sandwiching” method required when using *ex situ*-type ionogels, as the unconfined IL may more easily diffuse into the pore volume.

As a result of these considerations, a significant body of work has been accumulated devoted to sol-gel chemistry, the second main method of combining inorganic oxides with ILs.<sup>12–18,24</sup> “Sol-gel” describes a class of chemistries in

which a liquid oxide precursor undergoes a series of reactions to form solid particles known as sols. These sols then gel to form a continuous oxide structure. Sol-gel is an ideal method for the creation of ionogels as it is a solution-based process that is well-studied and industrially relevant and can be used to produce a wide variety of products.<sup>25,26</sup>

The sol-gel reaction used in this investigation is a simple, non-hydrolytic, one-pot reaction using two reagents: tetramethoxysilane (TMOS) is used as the silica precursor and formic acid (FA) is used as the catalyst.<sup>27</sup> During the course of this reaction, TMOS undergoes carboxylation, esterification, hydrolysis, and condensation reactions to create a silica network, which grows over a period of time that can last from minutes to hours or even days. Both TMOS and FA are soluble in ILs of interest, and as such the sol-gel reaction can be conducted in an IL medium to create a silica-supported ionogel.

Reports by a number of researchers have described the creation of bulk ionogels<sup>12-14</sup> and detailed the impact of changing the reactive formulation or introducing variations into the chemistry of the sol-gel reaction.<sup>15-18</sup> However, little work has been conducted on the creation of ionogel thin films, as are desirable for the fabrication of next-generation devices, or on the dynamics of the sol-gel process as it pertains to ionogels.

Sol-gel is unique among ionogel creation processes as it involves the gradual growth of solid particles from a liquid state (as opposed to a crosslinking polymerization, or the blending of an IL with an already-formed solid material). The viscosity change between the sol and gel states tends to be quite abrupt.<sup>25</sup> As

such, it is conceivable that an ionogel precursor solution could be cast onto a porous electrodes at many points throughout the scaffold growth process, leading to potential differences in the pore utilization and electrolyte/electrode interface of the device. This suggests that casting time, in addition to other parameters such as reactive formulation, must be optimized in order to obtain high-performance devices.

In this work, silica-supported ionogel thin films are cast *in situ* for the first time and the influence of ionogel casting time on silica scaffold morphology and device performance is explored. It is shown that casting ionogel films at different points prior to the expected bulk gel time has a significant impact on final silica morphology when casting is conducted in an ambient atmosphere. The impact of the differences in films grown with different casting times is demonstrated by comparing the performance of early-times casting devices with late-times casting devices. All devices were made with laser-scribed graphene electrodes on a flexible vinyl substrate. It is shown that devices made with later casting times have significantly improved performance as compared to devices made with earlier casting times, potentially due to decreased pore blockage.

## **6.2 Results and Discussion**

### **6.2.1 The Influence of Casting Time and Atmosphere on Silica Morphology**

In order to explore the influence of casting time on silica morphology, a rapidly-gelling formulation was employed with a 13.8:1 molar ratio of FA:TMOS

and 66% ionic liquid by volume in the reactive mixture. The IL used in this investigation was 1-ethyl-3-methylimidazolium bis(trifluoromethylsulfonyl)imide (EMI TFSI). This formulation produces a compliant ionogel and has an expected bulk gelation time of 30 minutes. In other words, 30 minutes is the time required for flowing behavior to cease when gelation is conducted on a bulk liquid sample in a sealed vial.

The impact of casting time on film morphology was explored by casting films onto a glass microscope slide immediately after mixing, as well as at  $\frac{1}{3}$  and  $\frac{2}{3}$  of the way through the expected bulk gelation time (corresponding to 10 and 20 minutes after mixing, respectively). Interestingly, doctor-bladed films prepared in an ambient atmosphere were observed to cease flowing behavior within several minutes of casting, regardless of the casting time. The final films showed significant differences from the bulk ionogel. The silica content of ionogel films was observed to increase throughout the gelation time, from 3.6% at 0 minutes, to 4.8% at 10 minutes, to 5.1% at 20 minutes. Bulk ionogels created using this formulation have a silica content of approximately 7.9% by weight. This difference may be partially ascribed to the volatility of TMOS, which is considerable.<sup>28</sup>

In accordance with this observation, the silica morphology also varied strongly depending on film casting time. As shown in Figure 6.1, the film cast at 0 minutes after mixing has a scaffold that consists of several-micron large agglomerates of smooth, globular particles. Small nodules are observed to grow as casting time increased. The film cast at  $\frac{2}{3}$  of the way through the bulk gelation

time appears very similar to the bulk scaffold, with a rough, finely-textured surface and a highly interconnected and porous structure. As it has been shown that the structure of the silica scaffold stops changing shortly after gelation,<sup>29</sup> these morphological differences can be ascribed to the difference in gelation dynamics experienced by the samples cast at different times.

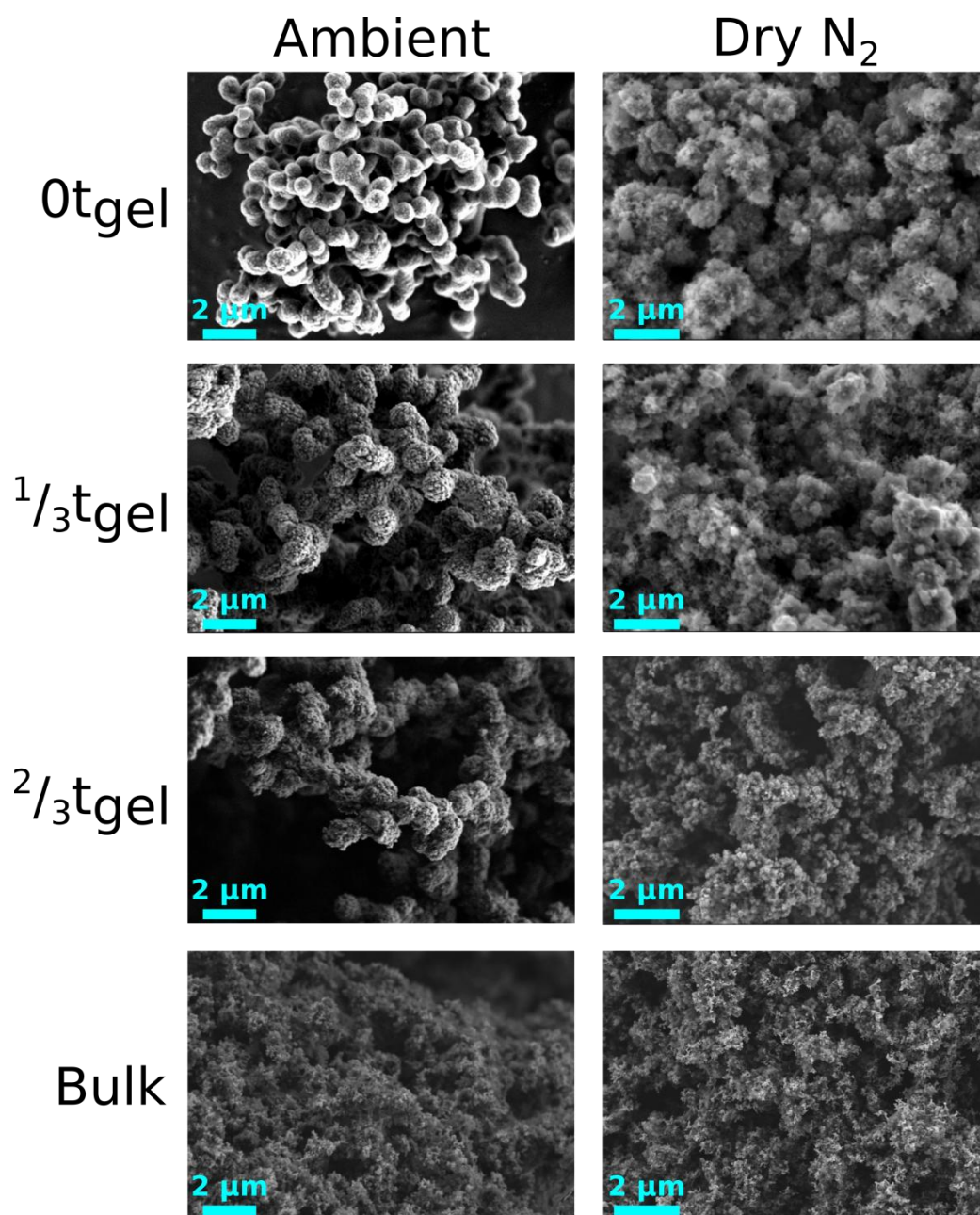


**Figure 6.1.** SEM images of silica scaffolds from doctor-bladed films and bulk ionogels made using the formulation 13.8:1 FA:TMOS, 66% EMI TFSI by volume. Samples were made both in ambient conditions and in a dry nitrogen atmosphere. In ambient conditions, casting at early times leads to very different scaffold morphology than is seen in the bulk. Samples cast in a dry environment, however, have very similar scaffold morphologies regardless of casting time.

Films cast in a dry nitrogen environment do not show the extreme morphological differences observed in samples cast in an ambient environment (Figure 6.1). Without the presence of moisture, these films continued to show flowing behavior over the entire expected bulk gelation time. Fine structure is seen on all samples and the silica contents are identical within error regardless of casting time (at approximately 6.1% silica by mass).

Because the differences in scaffold morphology largely disappear when films are cast in a dry environment, it can be concluded that the rapid-gelation effect and morphological differences arise primarily due to the influence of moisture. Although water is not added as a reagent to this system, it is created both as an intermediate and a byproduct.<sup>27</sup> As a result, the scaffold growth process is very sensitive to moisture. It appears that the exposure to atmospheric moisture experienced by thin ionogel films leads to an arrestation of the scaffold growth process soon after casting. This leads to the effect seen in Figure 6.1, wherein a film cast at 0 minutes after mixing displays only the large nucleated silica particles and not any of the fine, interconnected growth of later reaction stages.

#### 6.2.2. The Impact of Casting Time on Device Performance

Casting time also has a significant effect on device performance when ionogels are paired with porous, high surface area (HSA) electrodes to create supercapacitor devices (Figure 6.2). It is known that the addition of silica content tends to decrease bulk ionogel conductivity and therefore increase the overall resistance of a device.<sup>16</sup> However, in addition to this effect on the bulk, pore

blockage is a major concern when conducting *in situ* gelation.<sup>22,23</sup> In this investigation, laser-scribed graphene pads with silver paint leads were used as the HSA electrodes. The structure of these electrodes can be seen in Figure 6.3. Exfoliated graphene sheets have pores ranging in size from tens of nanometers to one micron. Although sufficiently small to block the entrance of most silica aggregates formed over the course of the gelation process, this pore size distribution is sufficient to allow the entrance of sol-gel reagents or silica nucleates.



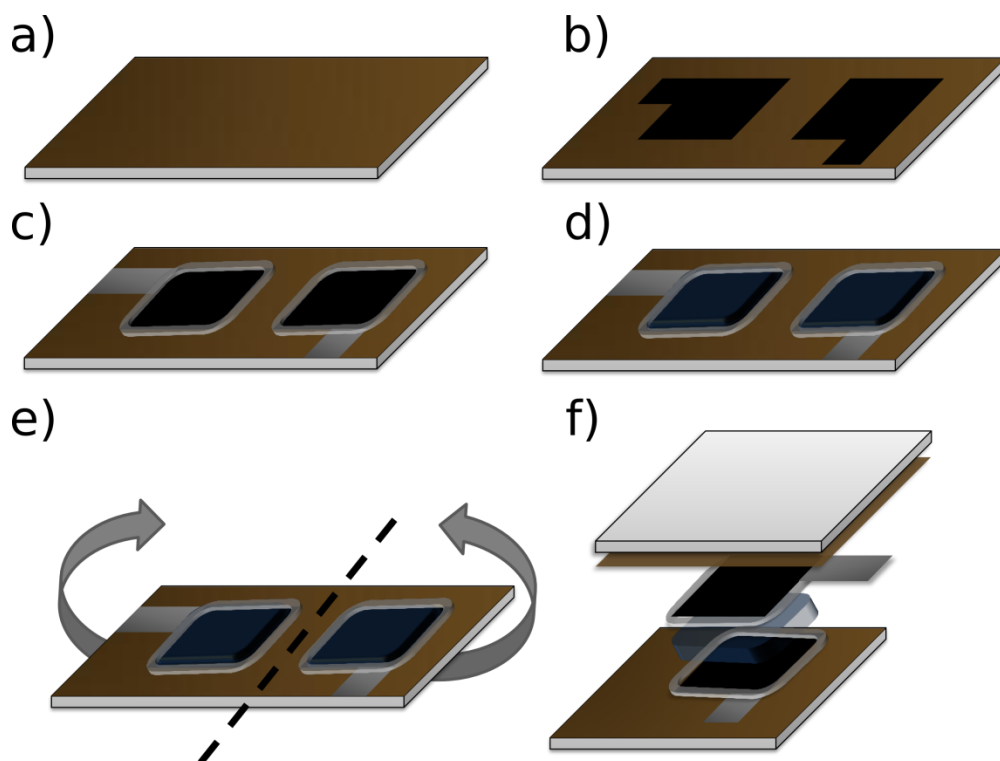


**Figure 6.2.** The process of creating supercapacitor devices with ionogel electrolytes. a) A graphene oxide film is cast onto a flexible vinyl substrate that has been overlain on a Lightscribe-enabled compact disc (not shown). b) Graphene electrodes in the shape of squares with small “tabs” are laser-scribed onto the graphene oxide surface. The vinyl film is removed from the substrate and cut to isolate the two electrodes needed to make a single device. c) Silver ink is painted onto the electrode tabs to make leads, and an epoxy border is created around the exposed graphene area. Two windowed PTFE films are used to mask the rest of the substrate (not shown). d) Ionogels are cast and allowed to react undisturbed for several minutes. e) The PTFE films are removed and the substrate is folded to bring the ionogel layers into contact, forming the device. f) An exploded view of the final device, which consists of an ionogel symmetrically sandwiched with graphene, graphene oxide, and vinyl.

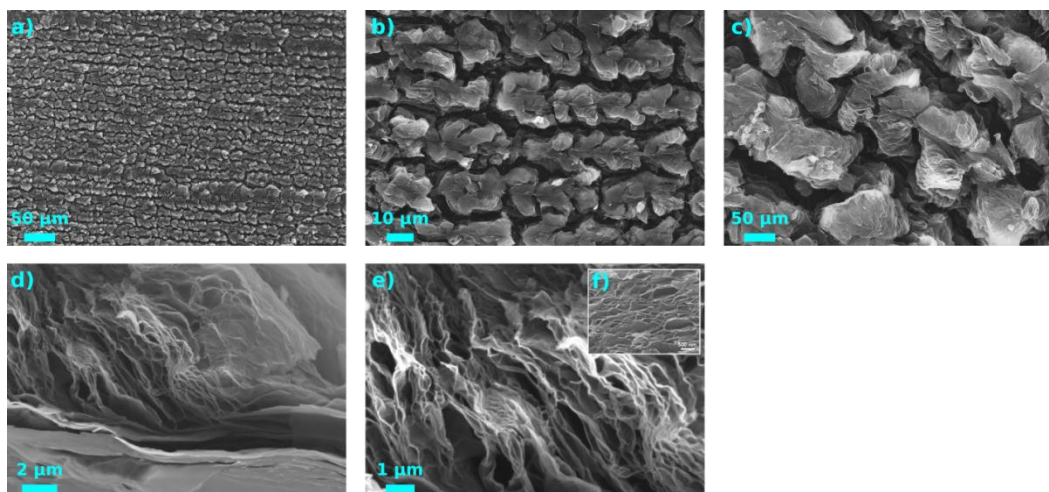


**Figure 6.3.** SEM images of laser-scribed graphene. (a-c) Top-view images showing grooves in the graphene surface. These grooves are an artifact of operation of the optical drive used in the laser-scribing process, and may allow good infiltration of the electrolyte into the pore structure of the graphene. (d-e) Side-view images showing the graphene pore structure. The smooth areas at the bottom of (d) are un-reduced graphene oxide. Although the pores appear to be tilted or vertically-oriented, this is an artifact of the sample preparation and orientation, and pores are natively oriented parallel to the vinyl substrate. Graphene pores vary in size between tens of nanometers and one micron, and are comparable in scale and morphology to those shown in El Kady and Kaner<sup>30</sup> (f, sized here so that panels e and f are at the same magnification). This suggests that differences in the graphene conductivity are due to variations in the graphene oxide flake size and degree of aggregation, rather than any disparities in the laser-scribing process itself.

Electrical measurements of supercapacitor devices made with ionogel electrolyte films cast at different times confirm that the smaller aggregates are able to penetrate into graphene pores, causing pore blockages. Devices were made in air with identical electrodes, with the only difference being the electrolyte. Three electrolytes were tested: the neat IL, an ionogel film cast immediately (0 minutes) after mixing, and an ionogel film cast at a delayed time (20 minutes after mixing, or  $\frac{2}{3}$  of the way through the expected bulk gelation time). The morphological differences between the ionogel electrolytes in the two devices are comparable to those found in doctor-bladed ionogel films (Figure 6.3).

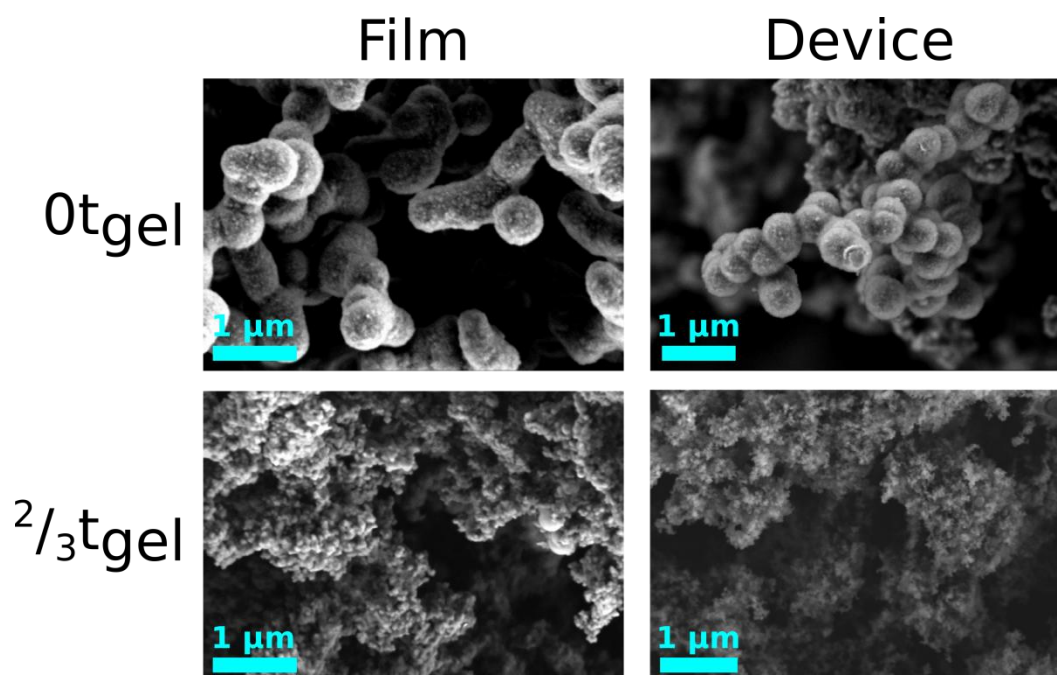


**Figure 6.4.** SEM images of silica scaffolds for samples cast as doctor-bladed films in an ambient atmosphere as well as for samples cast in an ambient atmosphere as electrolyte layers in devices with graphene electrodes. Immediate casting (at  $0t_{\text{gel}}$ ) leads to silica scaffolds with a smooth, globular structure and smaller aggregate sizes, whereas delayed casting (at  $2/3t_{\text{gel}}$ ) leads to finely-texture silica scaffolds with large aggregate sizes. For both the doctor-bladed films and the device electrolytes, the samples cast immediately after mixing have less silica by mass than the delayed casting samples. In the case of the device electrolytes, the immediate casting sample has a silica content of 5.8%, as compared to 7.8% for the delayed casting sample.

Ambient-atmosphere impedance measurements of these devices show the differences clearly (Figure 6.5). The device made with only neat IL and the delayed casting device have nearly identical capacitances, which demonstrates that the electrolyte has equal pore access in both devices. The immediate casting device has a much lower capacitance, suggesting significant pore blockage. Similarly, the device made with a neat IL electrolyte has the smallest series resistance, with only a slight increase shown for the delayed casting device, as is expected due to the increased bulk resistance of ionogels compared to the neat IL (Table 6.1). The immediate casting device has a significantly increased series resistance. This change is not due to any difference in the bulk resistivity of the ionogels cast at different times, but rather indicates a decrease in the effective surface area of the electrodes.

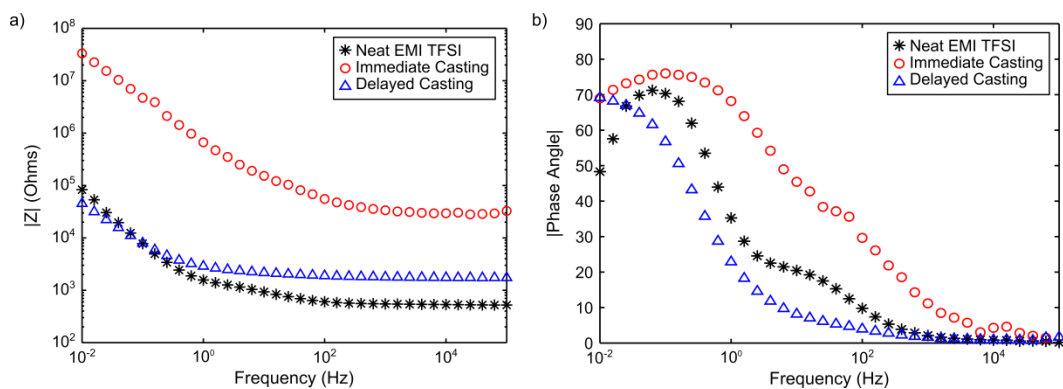


**Figure 6.5.** Ambient-atmosphere impedance spectroscopy for supercapacitor devices made with laser-scribed graphene electrodes and either neat EMI TFSI, an immediate casting ionogel, or a delayed casting ionogel electrolyte, including (a) the complex magnitude of impedance and (b) the phase angle of impedance. The delayed casting device has electrical properties which are much closer to the neat IL, including nearly identical capacitances (proportional to  $1/|Z|$  at low frequencies) and a slightly higher resistance ( $|Z|$  at high frequencies) and switching speed (the frequency at which the phase angle is  $45^\circ$ ). By contrast, the immediate casting device is much more resistive, much less capacitive, and has a significantly higher switching speed than the neat IL. These trends all suggest that there was significant pore blockage in the immediate casting device, increasing contact resistance and decreasing the surface area available for capacitive energy storage.

Pore blockage is also confirmed by the trend in switching speed for the three devices. The delayed casting device has a slightly slower switching speed than the neat IL device, which is again in accordance with the increased difficulty of ionic motion in ionogels. However, the immediate casting device has a significantly faster switching speed than the neat IL. As ionic motion in constrained pores is a relatively slow process, this increase in switching speed also demonstrates that the electrolyte has impaired pore access in the immediate casting case.

**Table 6.1.** Performance metrics for devices with various electrolyte conditions using different testing methods, including electrical impedance spectroscopy, cyclic voltammetry, and charge-discharge testing. For charge-discharge testing, current rates are given as well as voltage windows.

Testing Method	Metric		Immediate Casting	Delayed Casting	Neat IL
Impedance	Maximum phase angle (°)		76.0	69.7	71.2
	Switching speed (Hz)		19.8	0.23	0.60
	Series resistance (kOhms)		29.3	1.73	0.52
	Capacitance at 0.15 Hz (F/g)		0.001	0.66	0.66
Cyclic Voltammetry	Capacitance at 25 mV/s (F/g)		0.11	2.15	
	Capacitance at 125 mV/s (F/g)		0.021	1.37	
	Capacitance at 750 mV/s (F/g)		0.005	0.46	
Charge-Discharge	Series resistance (kOhms)	0.15 A/g, 2.5 V		9.70	
		0.12 A/g, 2 V		9.93	
		0.06 A/g, 2 V		10.6	
		0.03 A/g, 2 V		11.8	
		2 mA/g, 2 V	860		
	Capacitance (F/g)	0.15 A/g, 2.5 V		2.95	
		0.12 A/g, 2 V		2.80	
		0.06 A/g, 2 V		3.23	
		0.03 A/g, 2 V		3.97	
		2 mA/g, 2 V	0.17		



The immediate- and delayed casting devices were also subjected to cyclic voltammetry and charge-discharge testing in a dry nitrogen atmosphere. These tests allow for additional measurements of capacitance as well as demonstrating the electrochemical stability window of the devices. Cyclic voltammograms of the two devices for three different scan rates and voltage windows are shown in Figure 6.6. The delayed casting device demonstrates a much larger capacitance (Table 6.1) as well as showing a relatively rectangular scan shape through 2.5 V, which is characteristic of capacitive devices. The immediate casting device has a much reduced capacitance as well as a football-shaped scan that is indicative of undesirable side reactions. These reactions are likely due to interaction with the silver paint leads. Although an epoxy “fence” was used to contain the ionogel layer, some leakage was experienced by all samples. The increased reactive activity demonstrated by the immediate casting device may be due to breakdown caused by interaction with the reagents in the reactive formulation. Both TMOS and FA are quite reactive. However, by  $\frac{2}{3}$  of the way through the expected gelation time, much of the TMOS and FA in the mixture is expected to be converted to less-reactive intermediates and byproducts. This suggests that if ionogels were to be cast immediately after mixing, the reactivity of the mixture would be a significant concern.

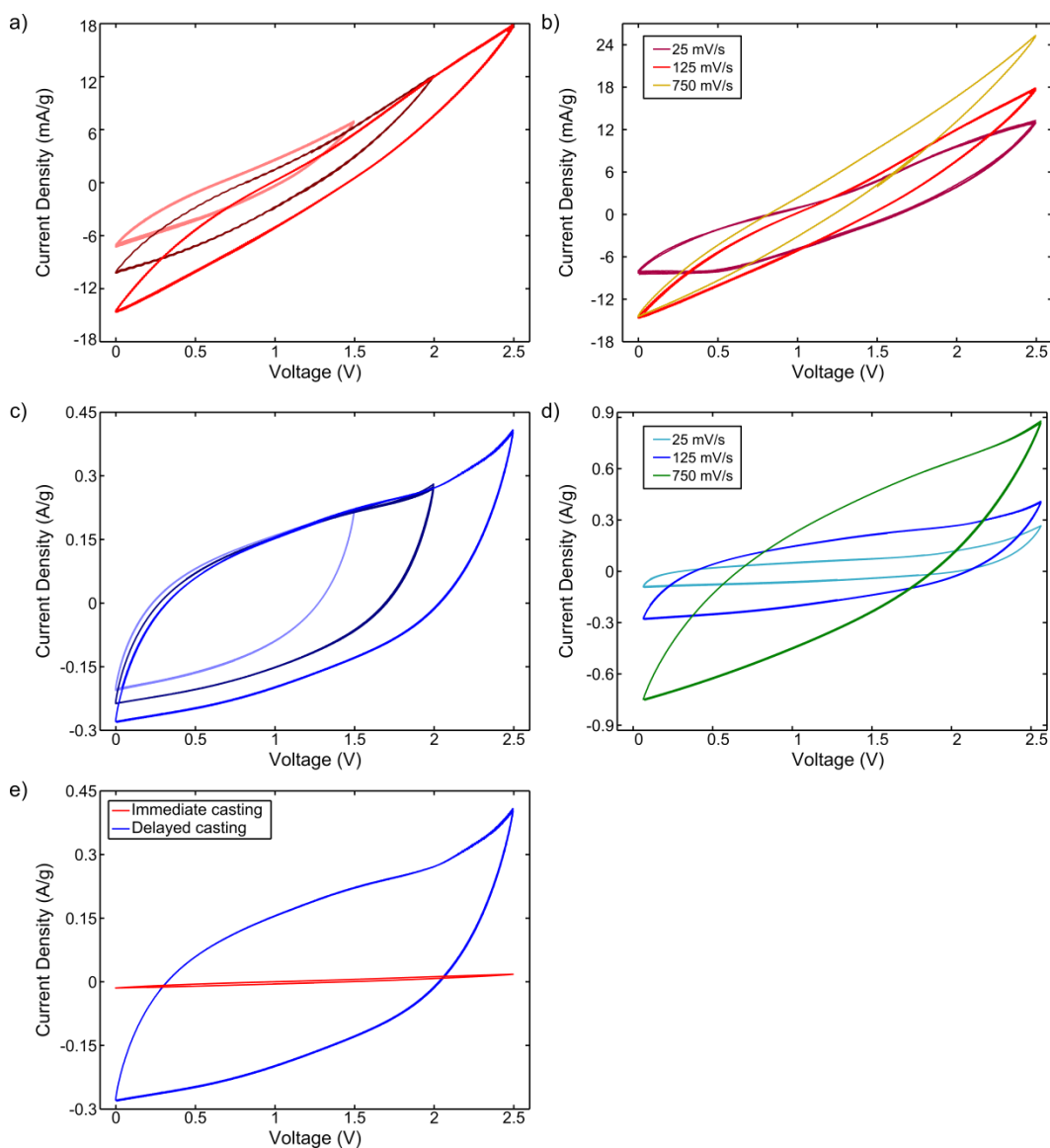


**Figure 6.6.** Cyclic voltammograms for (a-b) immediate casting and (c-d) delayed casting devices, as well as (e) a comparison of the two at a 0.125 V/s scan rate. Current density is normalized by the active electrode mass. Voltage window comparisons (a, c) also use a 0.125 V/s scan rate. The delayed casting demonstrates much higher capacitances, as well as a more rectangular scan shape, as opposed to the narrow football shape of the immediate casting device. Both devices show some signs of reactive activity, especially above 2 V.

The same trends in behavior can be seen in data from charge-discharge testing (Figure 6.7). The immediate casting device had sufficiently low capacitance as to only be able to be tested with very low current. The delayed casting device demonstrated good linear behavior to 2 V, using current densities that were orders of magnitude higher than were possible with the immediate casting device. The series resistance of both devices increased due to the increased setup resistance involved in testing in a glovebox. However, the immediate casting device displayed a very large IR drop, indicating an extremely high device series resistance, in agreement with the impedance results discussed above. In addition, the charge cycle shows the “turnover” effect that is characteristic of the presence of electrochemical reactions, even at less than 2 V.

As a result, the immediate casting device has energy and power densities that are orders of magnitude lower than those of the delayed casting device. At the comparable current rates shown in Figure 6.7c, the immediate casting device has an energy density of 0.1 mWh/g and a power density of 3.5 mW/g, which is below the “supercapacitor” shaded area found in Figure 1.1 of the Introduction. The delayed casting device, by contrast, displays an energy density of 1.6 mWh/g and a power density of 304 mW/g. Although these values are low and normalized by the active electrode mass rather than the device mass, they are within the range of behavior expected of a supercapacitor, demonstrating that delayed casting leads to far superior performance.

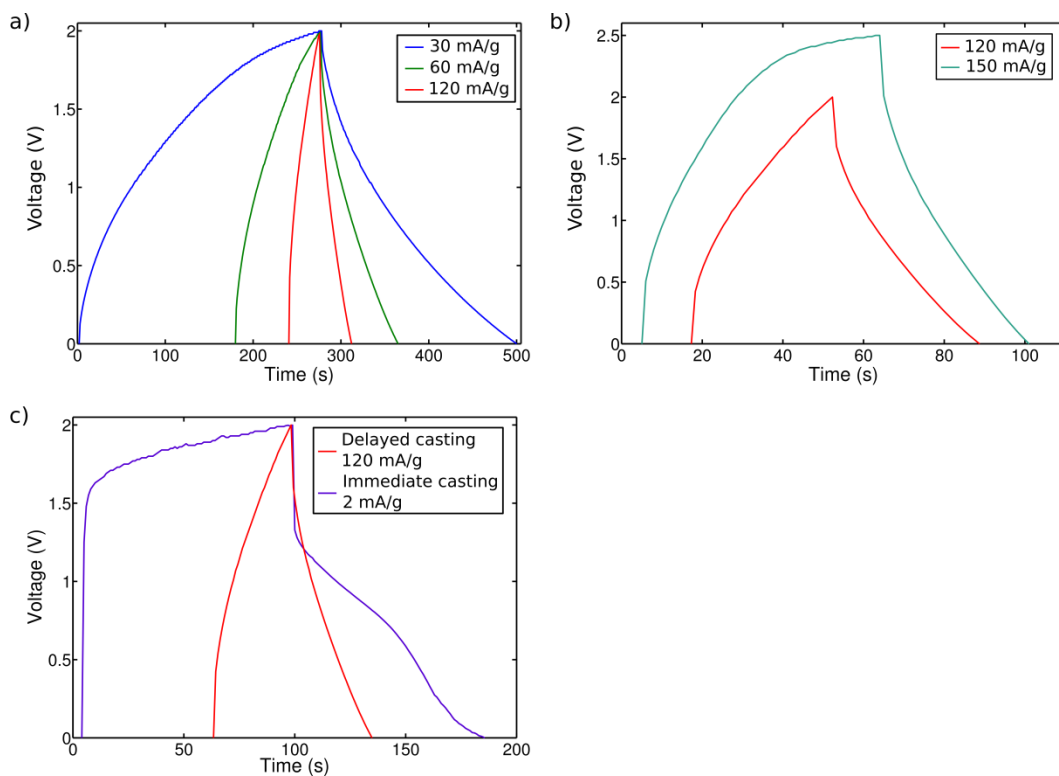


**Figure 6.7.** Charge-discharge testing. (a) Charge-discharge cycles for the delayed casting device using three different current rates. The device shows a modest IR drop as well as some evidence of reactive behavior, while maintaining a basically capacitive shape. (b) Cycles at two different voltage windows for the delayed casting device, demonstrating the plateauing that is characteristic of reactive behavior at high voltages. (c) Comparison of the delayed and immediate casting devices. The immediate casting device cannot withstand more than extremely slow currents, and shows significant signs of reactive behavior even at moderate voltages, as well as exhibiting a very large IR drop.

### 6.3 Conclusion

The results presented here have shown that the sol-gel reaction has a strong sensitivity to moisture, even when conducted in a hydrophobic IL medium without added water. Gelation occurs rapidly when the precursor solution is cast as a film and exposed to atmospheric moisture. The shift in the kinetics of the sol-gel reaction has a significant effect on final silica morphology and agglomerate size. In addition, ionogel casting time is an important factor in device performance when ionogels are paired with porous, HSA electrodes using *in situ* fabrication methods. Delaying casting until  $\frac{2}{3}$  of the way through the expected bulk gel time leads to much higher device performance, with minimal evidence of pore blockage. This result has important implications for the future industrial-scale fabrication of energy storage devices with ionogels.

## 6.4 Experimental Materials and Methods

### 6.4.1 Materials

Formic acid (98%) and TMOS (deposition grade, 98%) were purchased from Sigma Aldrich. EMI TFSI (synthesis grade) was purchased from EMD Merck. Graphene oxide dispersion (ultra-high purity, 6.2 g/L in water) was purchased from Graphene Supermarket and diluted to 3.7 g/L before use. Silver ink was taken from the reservoir of a CircuitWorks conductive pen, which was purchased from Ted Pella. Vinyl cling film was purchased from McMaster-Carr.

### 6.4.2 Casting of Ionogel Films

Films were cast using a doctor-blading technique, in which the precursor solution was pipetted onto the surface of a glass slide that had been previously prepared with layers of ParaFilm arranged to as to create a narrow channel. The channel was made to be wide enough that any reaction between the FA and ParaFilm would create only edge effects. Precursor solution was mixed using the formulation 13.8:1 FA:TMOS by moles, with 66% EMI TFSI by volume, following the procedure previously described.<sup>16</sup> Immediately after mixing, as well as at 10 and 20 minutes after mixing, an aliquot of precursor solution was removed and pipetted onto one end of the channel. A razor blade was then swept down the length of the channel, with excess solution running off of the substrate to create an even film of uniform volume. The same procedure was followed both

in and out of a glovebox to test ambient vs. dry nitrogen conditions. Ambient-condition films were approximately 140 micron thick after drying.

To test the bulk conductivity of gels cast at different times, a previously-described procedure was used to prepare ionogel samples between planar glassy carbon electrodes.<sup>16</sup>

#### 6.4.3 Thermogravimetric Analysis (TGA)

TGA was used both to determine silica content and to remove IL from the ionogels in preparation for SEM imaging. Samples were subjected to a 10 °C/min. temperature ramp from ambient temperature to 800 °C, as previously described.<sup>31</sup>

#### 6.4.4 Preparation of Graphene Electrodes

Graphene electrodes were fabricated using a laser-scribing technique first described by the Kaner group.<sup>30,32,33</sup> A LightScribe optical drive was adapted for this purpose. A flexible vinyl substrate was adhered to the surface of a LightScribe-compatible disc and the edge sealed and blocked with Mortite caulking cord (McMaster-Carr). 5 mL of a graphene oxide dispersion as described above was then drop-cast onto the entire substrate disc and allowed to dry. Once dry, AudioLabel software was used to pattern graphene onto the graphene oxide sheet to create electrodes. Electrodes consisted of a 1x1 cm square area of graphene with a 0.25x0.25 cm “tab” on one corner. Electrodes were patterned in a “paired” configuration such that a device’s worth of electrodes consisted of two pads separated by 1 cm of vinyl. Seven burn cycles at the “best” quality setting

were used to achieve a contact resistance of approximately 2 kOhm. The active mass of two electrodes was estimated to be 330  $\mu\text{g}$  using a mass balance approach.

After patterning, silver ink was painted onto the “tab” of the finished graphene electrodes, creating a lead to facilitate electrical contact between the electrodes and the potentiostat. A 300  $\mu\text{m}$  layer of Cytec EasyPoxy<sup>®</sup> K-45 epoxy was then painted around the 1x1 cm square of exposed graphene. This epoxy served as a spacer around the edges of the device as well as containing the reactive solution pre-gelation. A 1  $\mu\text{m}$ -thick PTFE sheet with a 1x1 cm window cut out of it was pressed onto the epoxy before it cured to reduce contact area between the reactive solution and the epoxy.

#### 6.4.5 Device Fabrication

Precursor solution was mixed as above. At 0 and 20 minutes after casting, 150  $\mu\text{L}$  aliquots of precursor solution were pipetted onto each electrode (two aliquots per device). The devices were observed carefully to detect gelation, which occurred 14 minutes after casting for the immediate casting case and 6 minutes after casting for the delayed casting case. After gelation occurred, the PTFE sheet was removed and the vinyl substrate connecting the two electrodes was folded to bring the ionogel layers into contact with one another. The overhanging vinyl edges were clipped together using binder clips and a small weight (approximately 8 g) was placed on top of the device to apply even pressure and ensure that the



two ionogel layers would fuse. Devices were allowed to cure for 10 days before testing to ensure the evaporation of volatiles.

#### 6.4.6 Device Testing

Electrical impedance testing and cyclic voltammetry (CV) were conducted as previously described.<sup>16</sup> CVs were recorded in a dry nitrogen environment using a voltage window of 2.5 volts and scan rates of 25, 125, and 750 mV/s. Taking the frequency of one scan as the scan rate divided by the total voltage “distance” travelled in a cycle (5 V), this corresponds to approximately to frequencies of 5, 25, and 150 mHz, all points at which the devices had high phase angles.

Charge-discharge testing was also conducted in a dry nitrogen atmosphere, using a voltage window of 2 V. For the delayed casting device, current rates of 30, 60, and 120 mA/g were used to approximate frequencies of 2, 5, and 14 mHz (corresponding to phase angles of approximately 60°, 65°, and 70°). For the immediate casting device, a current rate of 2 mA/g was used, corresponding to a frequency of 3 mHz and a phase angle of approximately 70°.

## 6.5 References

1. Le Bideau, J., Viau, L. & Vioux, A. Ionogels, ionic liquid based hybrid materials. *Chem. Soc. Rev.* **40**, 907–925 (2011).
2. Armand, M., Endres, F., MacFarlane, D. R., Ohno, H. & Scrosati, B. Ionic-liquid materials for the electrochemical challenges of the future. *Nat. Mater.* **8**, 621–629 (2009).
3. Gu, Y. *et al.* High Toughness, High Conductivity Ion Gels by Sequential Triblock Copolymer Self-Assembly and Chemical Cross-Linking. *J. Am. Chem. Soc.* **135**, 9652–9655 (2013).
4. Lee, K. H., Zhang, S., Lodge, T. P. & Frisbie, C. D. Electrical Impedance of Spin-Coatable Ion Gel Films. *J. Phys. Chem. B* **115**, 3315–3321 (2011).
5. Susan, M. A. B. H., Kaneko, T., Noda, A. & Watanabe, M. Ion Gels Prepared by in Situ Radical Polymerization of Vinyl Monomers in an Ionic Liquid and Their Characterization as Polymer Electrolytes. *J. Am. Chem. Soc.* **127**, 4976–4983 (2005).
6. Visentin, A. F. & Panzer, M. J. Poly(Ethylene Glycol) Diacrylate-Supported Ionogels with Consistent Capacitive Behavior and Tunable Elastic Response. *ACS Appl. Mater. Interfaces* **4**, 2836–2839 (2012).
7. Pandey, G. P. & Hashmi, S. A. Ionic liquid 1-ethyl-3-methylimidazolium tetracyanoborate-based gel polymer electrolyte for electrochemical capacitors. *J. Mater. Chem. A* **1**, 3372 (2013).

8. Patel, M., Gnanavel, M. & Bhattacharyya, A. J. Utilizing an ionic liquid for synthesizing a soft matter polymer ‘gel’ electrolyte for high rate capability lithium-ion batteries. *J. Mater. Chem.* **21**, 17419–17424 (2011).
9. Ueno, K., Hata, K., Katakabe, T., Kondoh, M. & Watanabe, M. Nanocomposite Ion Gels Based on Silica Nanoparticles and an Ionic Liquid: Ionic Transport, Viscoelastic Properties, and Microstructure. *J. Phys. Chem. B* **112**, 9013–9019 (2008).
10. Ueno, K., Imaizumi, S., Hata, K. & Watanabe, M. Colloidal interaction in ionic liquids: Effects of ionic structures and surface chemistry on rheology of silica colloidal dispersions. *Langmuir* **25**, 825–831 (2008).
11. Ueno, K. & Watanabe, M. From Colloidal Stability in Ionic Liquids to Advanced Soft Materials Using Unique Media. *Langmuir* **27**, 9105–9115 (2011).
12. Néouze, M.-A., Le Bideau, J. & Vioux, A. Versatile heat resistant solid electrolytes with performances of liquid electrolytes. *Prog. Solid State Chem.* **33**, 217–222 (2005).
13. Néouze, M.-A., Bideau, J. L., Gaveau, P., Bellayer, S. & Vioux, A. Ionogels, New Materials Arising from the Confinement of Ionic Liquids within Silica-Derived Networks. *Chem. Mater.* **18**, 3931–3936 (2006).
14. Néouze, M.-A., Bideau, J. L., Leroux, F. & Vioux, A. A route to heat resistant solid membranes with performances of liquid electrolytes. *Chem. Commun.* **41**, 1082–1084 (2005).

15. Gayet, F. *et al.* Polymer nanocomposite ionogels, high-performance electrolyte membranes. *J. Mater. Chem.* **20**, 9456–9462 (2010).
16. Horowitz, A. I. & Panzer, M. J. High-performance, mechanically compliant silica-based ionogels for electrical energy storage applications. *J. Mater. Chem.* **22**, 16534–16539 (2012).
17. Horowitz, A. I. & Panzer, M. J. Poly(dimethylsiloxane)-Supported Ionogels with a High Ionic Liquid Loading. *Angew. Chem.* **126**, 9938–9941 (2014).
18. Horowitz, A. I., Arias, P. & Panzer, M. J. Spectroscopic determination of relative Brønsted acidity as a predictor of reactivity in aprotic ionic liquids. *Chem Commun* (2015). doi:10.1039/C5CC01226K
19. Largeot, C. *et al.* Relation between the Ion Size and Pore Size for an Electric Double-Layer Capacitor. *J. Am. Chem. Soc.* **130**, 2730–2731 (2008).
20. Izadi-Najafabadi, A. *et al.* High-Power Supercapacitor Electrodes from Single-Walled Carbon Nanohorn/Nanotube Composite. *ACS Nano* **5**, 811–819 (2011).
21. Anothumakkool, B., Torris A. T, A., Bhange, S. N., Badiger, M. V. & Kurungot, S. Electrodeposited polyethylenedioxythiophene with infiltrated gel electrolyte interface: a close contest of an all-solid-state supercapacitor with its liquid-state counterpart. *Nanoscale* **6**, 5944 (2014).
22. Liu, H.-Y., Wang, K.-P. & Teng, H. A simplified preparation of mesoporous carbon and the examination of the carbon accessibility for electric double layer formation. *Carbon* **43**, 559–566 (2005).

23. Yu, Z., Tetard, L., Zhai, L. & Thomas, J. Supercapacitor electrode materials: nanostructures from 0 to 3 dimensions. *Energy Env. Sci* **8**, 702–730 (2015).
24. Dai, S. *et al.* Preparation of silica aerogel using ionic liquids as solvents. *Chem. Commun.* **3**, 243–244 (2000).
25. Hench, L. L. & West, J. K. The sol-gel process. *Chem. Rev.* **90**, 33–72 (1990).
26. Vioux, A., Viau, L., Volland, S. & Le Bideau, J. Use of ionic liquids in sol-gel; ionogels and applications. *Comptes Rendus Chim.* **13**, 242–255 (2010).
27. Sharp, K. G. A two-component, non-aqueous route to silica gel. *J. Sol-Gel Sci. Technol.* **2**, 35–41 (1994).
28. Anderson, A. M., Roth, T. B., Ernst, M. R. & Carroll, M. K. Saturated Liquid Densities and Vapor Pressures of Tetramethyl Orthosilicate Measured Using a Constant Volume Apparatus. *J. Chem. Eng. Data* **53**, 1015–1020 (2008).
29. Martinelli, A. Effects of a Protic Ionic Liquid on the Reaction Pathway during Non-Aqueous Sol–Gel Synthesis of Silica: A Raman Spectroscopic Investigation. *Int. J. Mol. Sci.* **15**, 6488–6503 (2014).
30. El-Kady, M. F. & Kaner, R. B. Scalable fabrication of high-power graphene micro-supercapacitors for flexible and on-chip energy storage. *Nat. Commun.* **4**, 1475 (2013).
31. Horowitz, A. I., Wang, Y. & Panzer, M. J. Reclamation and reuse of ionic liquids from silica-based ionogels using spontaneous water-driven separation. *Green Chem.* **15**, 3414–3420 (2013).

32. El-Kady, M. F., Strong, V., Dubin, S. & Kaner, R. B. Laser Scribing of High-Performance and Flexible Graphene-Based Electrochemical Capacitors. *Science* **335**, 1326–1330 (2012).
33. Strong, V. *et al.* Patterning and Electronic Tuning of Laser Scribed Graphene for Flexible All-Carbon Devices. *ACS Nano* **6**, 1395–1403 (2012).

## **Chapter 7**

### **Reclamation and Reuse of Ionic Liquids from Silica-Based Ionogels Using Spontaneous Water-Driven Separation**

#### **7.1 Introduction**

The room-temperature molten salts known as ionic liquids (ILs) have attracted attention in the literature and popular science writing for being “green” liquids of the future.<sup>1–6</sup> ILs have negligible vapor pressure at ambient temperatures and are therefore often proposed as a safer and more environmentally-friendly alternative to common organic solvents.<sup>2,4,5</sup> They have already gained traction in the field of organic synthesis, as the solvent properties of ILs can be widely tuned by adjusting the structure of the cation or anion.<sup>5,7–10</sup> The ability of ILs to act as electrolytes has also attracted researchers interested in electrochemical applications.<sup>6,11,12</sup> In particular, ILs have been investigated as electrolytes for lithium ion batteries, dye-sensitized solar cells, and electrochemical double-layer capacitors (supercapacitors). Several ILs possess relatively high ionic conductivities and wide windows of electrochemical stability, making them attractive alternatives to the traditional electrolytes used in these devices. Since many of these technologies may find use in sustainable energy applications, the apparently environmentally-friendly nature of ILs is often touted as a synergistic benefit of their use.

However, it has emerged in recent years that the reputation ILs have gained as environmentally benign is not entirely deserved. Life-cycle analyses of ILs reveal that their manufacturing is often energy-intensive<sup>4,13</sup> and their environmental

release may pose toxicity concerns.<sup>14–20</sup> Several researchers have found that IL toxicity increases with hydrophobicity (which increases with hydrocarbon chain length in common IL cations and with factors such as fluorination in common anions).<sup>14–16,21</sup> Hydrophobicity is a desirable characteristic when considering ILs for use in electrochemical devices, however, as the use of a hydrophobic IL minimizes concerns regarding water contamination and undesirable electrochemical side reactions. Similarly, the chemical stability offered by many ILs is an appealing characteristic for many applications, but also leads to concerns of bioaccumulation.<sup>14,20</sup> The environmental concerns presented by ionic liquids, combined with their relatively high cost (at over \$5/gram<sup>22</sup>), makes reclaiming and recycling ILs an attractive proposition.

ILs are well-suited for recycling due to their lack of volatility, relatively high thresholds for thermal and electrochemical decomposition, and the fact that their major applications generally do not alter the IL through any chemical reaction. ILs are already re-used in applications where they serve as solvents.<sup>7–9,23,24</sup> As these applications normally involve either only liquid-phase species or the development of a precipitate, separations are relatively straightforward.<sup>25</sup> Moreover, separations are a necessary processing step due to the need to isolate the synthesis product with as high a yield and purity as possible. Normally the desired compound is isolated from the IL medium through a liquid-liquid extraction or filtration (depending on the phase of the product). In order to reuse the IL, volatile components such as solvent residue from a liquid-liquid separation



can be removed under vacuum, or the IL can be isolated using a supercritical fluid.<sup>25</sup> Few researchers report a complete materials balance on the ionic liquid; however, the IL is typically reused at least three to five times. Previous reports have described processes leading to IL reclamation on the order of 90% or above.<sup>9,24</sup>

The IL recycling procedures described above apply only to applications where the IL is used as a liquid solvent. Another proposed paradigm for employing ILs involves confining them into a solid or solid-like form using a gelation process. The resultant hybrid materials, known as ionogels, are candidates for a wide variety of applications, as they maintain the favorable properties of the IL while preventing flow behavior.<sup>26</sup> In particular, there is great interest in using ionogels as electrolyte membranes for electrochemical energy conversion devices.<sup>27–29</sup> Using ionogels instead of ILs in the liquid form enables fully solid-state thin film device construction and an avoidance of the heavy containers that are necessary to prevent electrolyte leakage.<sup>30</sup> These are significant advantages in the field of energy generation and storage, where gravimetric energy and power densities are among the most important performance metrics.

A wide variety of ionogels have been characterized in the literature to date,<sup>27–29,31–38</sup> with the difference between them resting mainly in the choice of scaffold material and the means of combining the IL with the scaffold. Scaffold materials can be formed *in situ* within an IL through chemical reactions or spontaneous self-assembly, or prepared separately and mixed with an IL to form a solid or

solid-like material.<sup>26</sup> While polymer-based systems are common, recently silica-supported ionogels have gained interest from a number of researchers for applications ranging from supercapacitors and batteries to fuel cells and as electrorheological media.<sup>31,38–43</sup> Two primary types of silica-supported ionogels have been realized to date. The first type is created by mixing an IL with a small weight percent of fumed silica nanoparticles (denoted as FS-ionogel). Previous reports have characterized the physical properties and electrochemical response of FS-ionogels.<sup>30,32,33</sup> The properties of these ionogels may be tuned somewhat by changing the weight percent and size of the silica nanoparticles employed. FS-ionogels are simple to prepare, making them appealing for testing new electrodes with an ionogel electrolyte in electrochemical devices, but must be applied to an electrode post-gelation. It is also possible to create silica-supported ionogels *in situ*, with a silica scaffold created through sol-gel reaction (SG-ionogel).<sup>31,42,43</sup> Although initial reports described these ionogels as glassy monoliths, the physical properties of SG-ionogels may be widely tuned by changing the reactive formulation; recently a low-silica formulation was characterized by our group.<sup>38</sup> Both FS- and SG-ionogels are straightforward to fabricate and incorporate into devices.<sup>30</sup>

If ionogel-based electrochemical device development proceeds successfully, applications in which ILs are most suitable in gel form may eclipse those in which ILs are used as liquids. Moreover, chemical syntheses occur mainly in controlled lab or industrial settings, whereas devices which require an electrolyte layer are

ubiquitous, and, as such, pose a much greater risk of environmental release of toxic materials if such concerns are not taken into account in advance. As such, it is of great interest to be able to recover and recycle ILs from ionogels. The ease of creating silica-supported ionogels and their wide applicability make this system an appealing test case for demonstrating IL recovery from ionogels.

This report describes an IL reclamation process designed for use on silica-supported solid ionogel electrolytes intended for use in electrochemical devices. This process hinges on the unique ability of water to spontaneously separate a variety of hydrophobic ionic liquids from silica-supported ionogels with no further energy input. This general schema may be of use in guiding IL reclamation from ionogels more generally, thereby shoring up the “green” reputation of ionic liquids and their use.

## **7.2 Results and Discussion**

### **7.2.1 Process Considerations**

Among several common solvents examined, water has proven to be unique in its ability to separate an IL from its silica scaffold without dissolving the IL. The stability of silica-supported ionogels towards solvent exposure has been explored by others.<sup>31,44–46</sup> SG-ionogels were first investigated by Dai due to the interesting morphological properties of the silica structure.<sup>44</sup> In order to study these structures, the IL was extracted from ionogels by subjecting them to reflux in

acetonitrile for 12 hours or longer.<sup>44–46</sup> While many solvents (such as short-chain alcohols, ethyl acetate, and acetonitrile) are capable of removing the IL from a silica scaffold in this manner,<sup>31</sup> the effectiveness of this removal is highly dependent on process conditions such as exposure time and solvent temperature (Appendix C, Table C1). Moreover, this removal method results in a single, IL-poor liquid phase. In order to isolate the IL, an energy-intensive and wasteful distillation process is required to remove the excess solvent. IL reclamation using such a solvation-based method would be costly, and the large energy requirements and use of a volatile organic solvent would negate some of the environmental benefits of recycling ILs.

Spontaneous water-based separation (Figure 7.1) of an IL from a silica-supported ionogel is a rapid, low energy input process. Upon contact with water, the silica-supported ionogel rapidly swells and turns opaque; the hydrophobic IL is then spontaneously expelled without further energy input. The IL is not dissolved during this process. Instead, the mixture partitions itself into three layers (Figure 7.1): the liberated ionic liquid, a silica/water slurry, and excess water. A large excess of water was used in this investigation, but partitioning has also been observed to occur with even small amounts of water. Here, the excess water from the slurry was driven off using a hotplate in order to be able to determine the recovered silica mass, as described in Figure 7.1. However, if this is not a concern, the silica solids can be easily filtered and the water purified or reused in further recovery cycles.

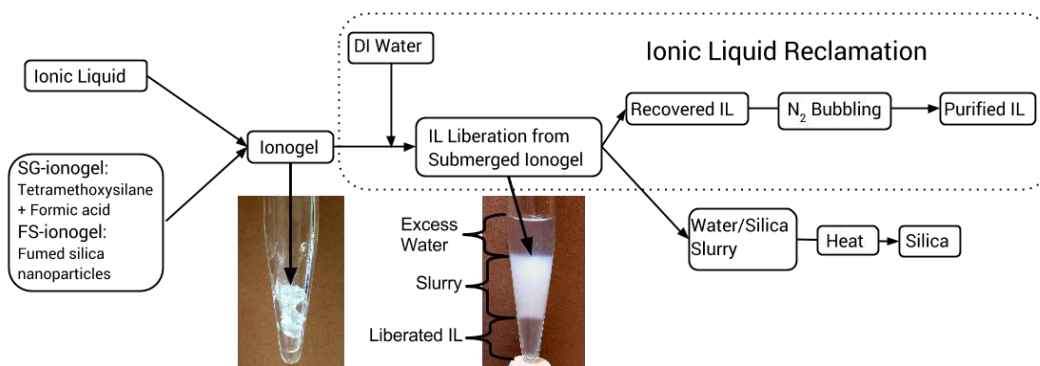


**Figure 7.1.** Process flow diagram for ionic liquid use and reclamation. The region bound by a dotted rectangle indicates the steps of the reclamation process: DI water is added, leading to a liquid/liquid separation between the IL and the aqueous phase. The IL can then be removed and purified, at which point it is ready for reuse. Photos show the ionogel before the addition of water, and the post-exposure separation into IL, water/silica slurry, and excess water layers.

Preliminary tests have shown that submersion in other solvents with which the ILs were immiscible, such as hexane or diethyl ether, does not lead to spontaneous IL removal. The effectiveness of the removal process appears to depend not only on the immiscibility of the solvent with the IL, but also on the interaction between the silica scaffold with the solvent in which it is submerged. Sol-gel silica structures, in particular, are known to have a large number of hydroxyl groups on their surface.<sup>47</sup> It is hypothesized that when the IL-coated silica scaffold is exposed to an excess of water, water molecules are successfully able to compete with the hydrophobic IL for access to the hydrophilic silica surface, forcing the IL out of the ionogel structure. Indeed, modifying the scaffold with hydrophobic groups prevents water from infiltrating the ionogel in this manner.<sup>31</sup>

While the process is sensitive to the surface properties of the scaffold, it appears to be relatively insensitive to the identity of the IL. Several hydrophobic ILs were employed in the creation of SG-ionogels in this study (Figure 7.2). The set of ILs employed represents variation in both the anion and cation species, including varying the cation chain length (a source of IL toxicity concerns as mentioned above). IL structural differences result in a range of viscosities and densities (Table 7.1). Importantly, the reclamation process leverages a density difference between the IL and the aqueous phase. As such, if the IL used to fabricate an ionogel does not have significantly greater density than the silica/water slurry, the separation process will not be efficient. For example, the

water-based reclamation process was also tested on a SG-ionogel created using the ionic liquid 1-ethyl-3-methylimidazolium tetracyanoborate (EMI TCB), which has a specific gravity of  $\sim 1.04$ . Although exposure to water did successfully cause the IL to separate from the silica scaffold, there was an insufficient density differential to facilitate rapid formation of an IL liquid layer. Instead, the liberated IL remained intermingled with the water/silica slurry, preventing efficient IL reclamation. While separation of such ILs could be encouraged with ultracentrifugation or similar techniques, such extra steps complicate the process and would increase energy requirements.

**Table 7.1.** Ionic liquid properties. Densities are from the manufacturer MSDS.

Water content was measured in ambient atmosphere after ILs were kept in general storage for several months.

<b>Ionic Liquid</b>	<b>Density (g mL<sup>-1</sup>)</b>	<b>Viscosity (cP, 25° C)</b>	<b>Water Content (ppm H<sub>2</sub>O)</b>
EMI TFSI	1.53	28 <sup>a</sup>	740
BMI TFSI	1.44	52 <sup>a</sup>	461
HMI TFSI	1.37	70 <sup>b</sup>	385
BMP TFSI	1.40	73 <sup>c</sup>	306
EMI FAP	1.71	60 <sup>d</sup>	249

<sup>a</sup> Ref. [55]

<sup>b</sup> Ref. [52]

<sup>c</sup> Ref. [53]

<sup>d</sup> Ref. [54]



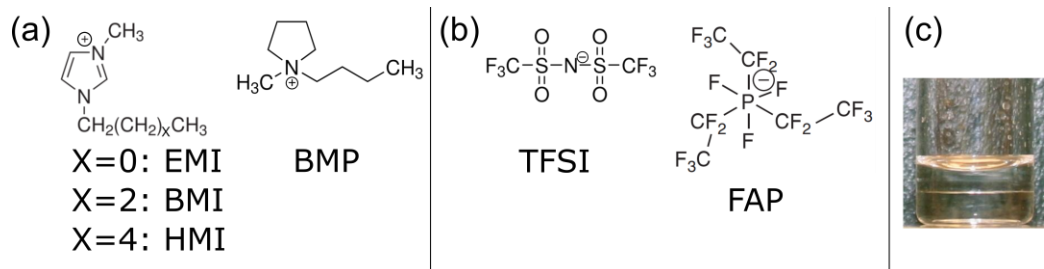


**Figure 7.2.** Structures and abbreviations for ionic liquids (ILs) employed. (a) Cations; (b) anions; (c) visible liquid phase separation between EMI TFSI (lower layer) and water. All the ionic liquids used in this investigation have specific gravities greater than 1.

### 7.2.2 Reclamation Effectiveness

The metrics of interest in evaluating the effectiveness of the reclamation process are: (1) the amount of IL that was recovered; and (2) the purity of the reclaimed IL. In general, the IL yields are quite good (Table 7.2); over 70% of the IL was reclaimed in all cases. There are two sources of IL loss: (1) IL that is not liberated from the silica scaffold, and (2) transfer losses.

Thermogravimetric analysis (TGA) was used to determine the approximate composition of all materials throughout the process; data shown for the case of BMP TFSI (Figure 7.3) are representative of those obtained for the other ionogels examined (Appendix C, Table C2). The TGA trace of virgin BMP TFSI shows a single major transition, representing the decomposition of the IL (Figure 7.3). This transition is also dominant in the ionogel trace, which differs from the neat IL mainly in the residual mass remaining after the IL decomposition. This residual mass represents the silica scaffold content of the ionogel. While the dried silica/IL residue material still shows some IL content (indicating less than 100% IL liberation), there is clearly a significant amount of mass remaining after IL decomposition. The recovered IL trace looks nearly identical to that of the virgin IL, except in the region below 200° C. It is this region that reflects the loss of any volatile material, including water. As can be seen in the inset to Figure 7.3, both the ionogel and the recovered IL exhibit some degree of mass loss in this region, whereas the virgin IL shows a negligible change in mass over the same temperature range. The dried silica/IL solid residue material shows the greatest

amount of volatile (water) loss in this region, consistent with the hydrophilic nature of the silica.

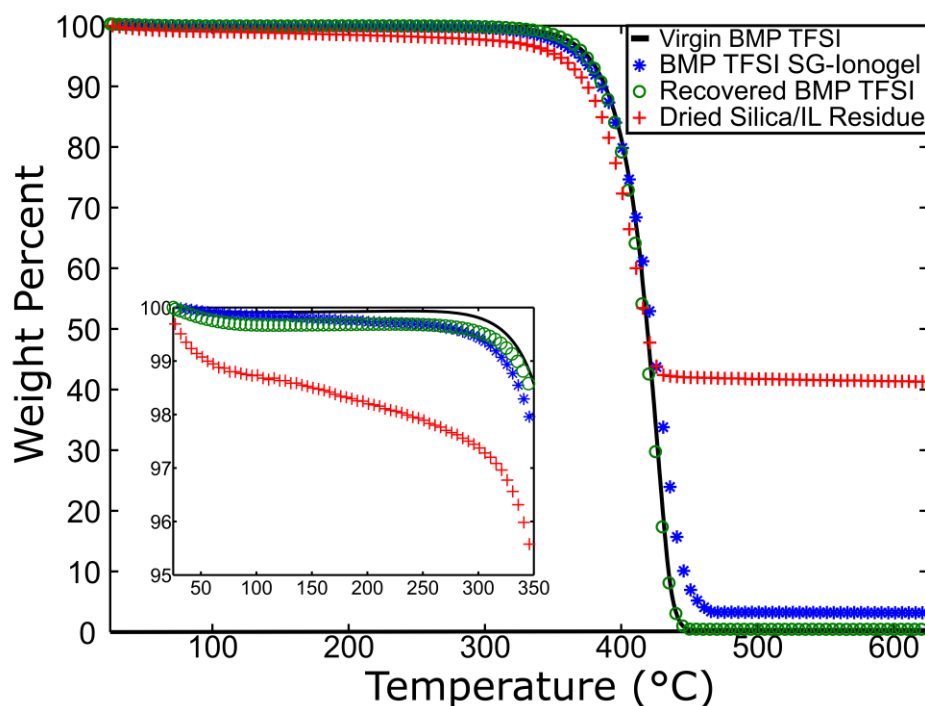


**Figure 7.3.** Thermogravimetric analysis (TGA) traces of virgin and recovered IL (BMP TFSI), the ionogel, and the dried silica/IL residue, showing differences in their composition. The inset shows the region from 25° to 350° C in greater detail, highlighting differences in the low-temperature mass loss due to the presence of water or other volatile species. The recovered IL trace is almost identical to the virgin material, with the main difference being a small increase in water content. The ionogel shows a small amount of silica content, as well as some volatile material as previously reported.<sup>38</sup> The dried silica/IL residue contains some IL and a noticeable amount of water.

TGA data were also used to calculate the extent of IL liberation, using the following equation (derived in Appendix C):

$$(7.1) \quad \% \text{ Liberated} = 100 (S_f - S_o) / (S_f - S_f S_o)$$

Here,  $S_o$  is used to denote the mass fraction of silica in the as-prepared ionogel and  $S_f$  refers to the mass fraction of silica in the leftover solid silica/IL residue (see Figure 7.3). Mass fractions were calculated on a dry basis (normalized to the sample mass at 200° C).<sup>38</sup> The % Lost to Silica is 100% minus the % Liberated. The % Reclaimed was found by mass balance and indicates the amount of IL material that was recovered following encapsulation into the ionogel, exposure to water (spontaneous separation from the silica scaffold), and purification. The total IL losses are 100% minus the % Reclaimed, and all losses not ascribed to the silica/IL residue were ascribed to transfer losses.

As seen in Table 7.2, the relative importance of transfer versus liberation losses varies among the SG-ionogels prepared using different ILs. On average across different samples, over 90% of IL content was liberated. The completeness of IL liberation may depend on many factors, ranging from IL properties such as hydrophobicity to ionogel-specific characteristics such as scaffold morphology or surface chemistry. These ionogel characteristics may vary both with the IL used as well as with ionogel formulation. Preliminary tests have shown that it is difficult to significantly change the effectiveness of the IL liberation step, either through temperature changes or through agitation. As such, further improvement of the recovery process mainly hinges on minimizing transfer losses.

Transfer losses were also high for the FS-ionogel, although the IL liberation was more complete in this case than for the EMI TFSI SG-ionogel. Once the IL is liberated from a SG-ionogel, the leftover silica forms a relatively dense and homogenous slurry layer as seen in Figure 7.1. In contrast, some agitation and resting is required to liberate the IL from FS-ionogels of similar initial IL content. This difference may be due to variations in surface chemistry between the fumed silica particles and the silica created through sol-gel. The silica slurry layer is less uniform for the case of FS particles, leading to a greater difficulty in isolating the IL and, therefore, larger transfer losses.

**Table 7.2.** Effectiveness of IL reclamation for various ionogels.

<b>Ionic Liquid</b>	<b>% Liberated</b>	<b>% Reclaimed</b>	<b>% Lost to Silica</b>	<b>% Transfer Losses</b>
EMI TFSI (FS)*	89	71	11	18
EMI TFSI (SG)*	86	79	14	7
BMI TFSI (SG)	92	84	8	8
HMI TFSI (SG)	99	81	1	18
BMP TFSI (SG)	95	73	5	21
EMI FAP (SG)	93	75	7	18

\*FS = fumed silica-supported ionogel; SG = sol-gel silica-supported ionogel

Transfer losses are expected to become relatively minor upon scale-up of the reclamation process. This investigation used a very small system volume (roughly 1 g of each ionogel). While transfer losses in this investigation constitute a relatively high percentage of the total IL mass (~15% on average), this represents a small absolute amount of material. A larger-scale system may choose the surfaces with which the IL comes in contact during the process in order to minimize IL wetting (one major source of transfer loss), while such modifications were not feasible on the lab scale. More importantly, with larger volumes of IL to recover, the reduction in surface area-to-volume ratio will work to the benefit of the recovery process.

### 7.2.3 Properties of Reclaimed ILs

In evaluating IL purity, water content is of specific interest when the intended application is utilization in an electrochemical device. Given that the ILs were submerged in water for a prolonged period during the reclamation process, it can be concluded that upon isolation from the silica slurry, the ILs were saturated with water (this occurs at a level of several thousand ppm for the studied ILs<sup>48–50</sup>). In this lab-scale investigation, IL isolation erred on the side of greater recovery, meaning that there was inevitably some visible amount of aqueous phase present in all isolated IL samples. Following isolation, N<sub>2</sub> gas was bubbled through the ILs to remove excess water, as described by Ren.<sup>51</sup> After the N<sub>2</sub> bubbling step, no samples contained a visible amount of water. However, the bubbling process



varied in effectiveness for the different ILs investigated. There was an observed increase in water content for all reclaimed ILs. EMI FAP exhibited the lowest post-bubbling water content, at 690 ppm, whereas BMP TFSI showed the highest, 4600 ppm, despite the fact that these two liquids possessed the lowest water contents when initially removed from the bottle (Table 7.1). In order to minimize the time required and the energy input to the reclamation process, N<sub>2</sub> bubbling was performed at ambient temperature. By performing the bubbling at somewhat elevated temperatures, more water may be removed.<sup>51</sup> It can be concluded that the bubbling process should be optimized for each IL.

The small amount of residual water present did not significantly affect the electrical properties of the reclaimed ILs. Figure 7.4 shows the cyclic voltammograms of virgin EMI TFSI and the recovered IL from both the SG- and FS-ionogels. The response from all three samples displays the rectangular shape characteristic of a capacitor and demonstrates stability over a 3 V window. The absolute change in capacitance was below 10% for all samples. Virgin EMI TFSI exhibited a specific capacitance of 16.5  $\mu\text{F cm}^{-2}$ , compared to 15.4  $\mu\text{F cm}^{-2}$  and 15.1  $\mu\text{F cm}^{-2}$  for EMI TFSI reclaimed from SG- and FS-ionogels, respectively. Such variations are considered to be within measurement error limits. A similar degree of consistency between virgin and reclaimed IL electrical performance was observed for all liquids examined. Therefore, recovered ILs are suitable for reuse in electrochemical devices.

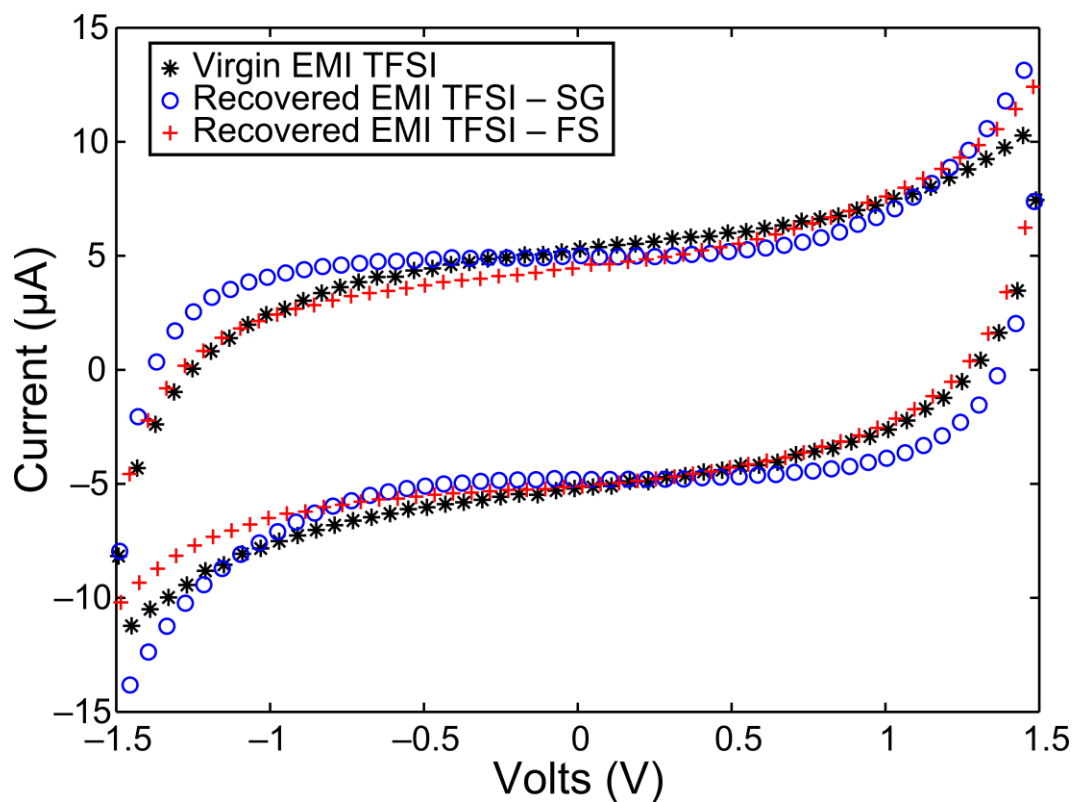


**Figure 7.4.** Cyclic voltammograms for virgin EMI TFSI and the recovered IL from both SG- and FS-ionogels. Tests were performed using a 1 V/s scan rate on a cell containing the IL between two planar stainless steel electrodes. All three traces exhibit a similar shape characteristic of a capacitive response, indicating that the IL electrical properties are not significantly affected by encapsulation into an ionogel and subsequent recovery using a water-based reclamation process.

### 7.3 Conclusion

Spontaneous water-based separation is a process capable of liberating ILs from silica-supported ionogels with minimal energy and water requirements. Its versatility has been demonstrated using a variety of ionic liquids and different ionogel types, leading to high IL recovery (>70%) in all cases. IL liberation depends on the silica scaffold surface having a greater affinity for water than for the IL. Further investigation of this phenomenon may lead to reclamation processes applicable to other ionogel types, such as polymer-based ionogels.

The IL reclamation process is amenable to scale-up, and will likely result in lower transfer losses as the system volume increases. The electrical performance of the reclaimed IL is shown to be nearly unchanged compared to the virgin IL using cyclic voltammetry. An observed double layer capacitance change of less than 10% and the retention of a 3 V electrochemical stability window indicate that reclaimed ILs are suitable for reuse in electrochemical applications, such as supercapacitors. By reclaiming ILs from ionogels, any environmental concerns posed by the use of IL-based gel electrolytes can be circumvented and their use can be truly described as “green.”

## 7.4 Experimental Details

### 7.4.1 Ionogel Preparation

Tetramethoxysilane (deposition grade, 98%), formic acid (98%), and non-porous fumed silica powder (7 nm particle size) were purchased from Sigma Aldrich. 1-Ethyl-3-methylimidazolium bis(trifluoromethylsulfonyl)imide (EMI TFSI), 1-butyl-3-methylimidazolium bis(trifluoromethylsulfonyl)imide (BMI TFSI), 1-hexyl-3-methylimidazolium bis(trifluoromethylsulfonyl)imide (HMI TFSI), 1-ethyl-3-methylimidazolium tris(perfluoroethyl)trifluorophosphate (EMI FAP), and 1-butyl-3-methylpyrrolidinium bis(trifluoromethylsulfonyl)imide (BMP TFSI) were purchased from EMD Merck. All reagents were used as received.

In order to prepare the FS-ionogel, roughly 0.11 g of FS spheres were added to a vial containing 1.5 mL of EMI TFSI. This mixture was stirred for 5 hours and allowed to sit undisturbed for several days.

SG-ionogels were prepared using a method described previously.<sup>38</sup> Formic acid, tetramethoxysilane, and an ionic liquid were mixed in a vial, which was then sealed overnight. Ionogels were then allowed to dry in ambient conditions for at least two weeks before testing. For EMI TFSI, BMI TFSI, and BMP TFSI, the formulation of the precursor solution had a 1:6 tetramethoxysilane:formic acid molar ratio and was 80% IL by volume. For HMI TFSI and EMI FAP, the reagent ratio was 4.8:1 and the solution was 67% IL by volume.

#### 7.4.2 IL Reclamation

IL reclamation tests were run in duplicate for ionogels created with HMI TFSI and EMI FAP and in triplicate for the remaining samples. Masses were recorded throughout the process. Glass vials used for reclamation tests were first treated with 1M NaOH in an effort to minimize transfer losses. After vials were rinsed with DI water, ~0.33 g of ionogel and 3 mL of deionized water was added to each vial. The use of deionized water avoids any concerns of contaminating the IL with additional ionic species. The mixtures were stirred briefly and allowed to sit undisturbed for 2 hours (for SG-ionogels) or overnight (for FS-ionogels). Long waiting periods were used in this investigation to ensure full settling of the silica layer, although full IL liberation was achieved on the scale of seconds to minutes. The IL layer was then syringed out and collected in a separate vial; the recovered IL from each replicate sample was combined for purification and further testing. After a brief waiting period to ensure that no further IL layer would form, the water/silica slurry was removed from the vial and syringed onto a watch glass. These samples were heated at 85° C until visibly dry.

Reclaimed IL was purified to remove residual water using vigorous N<sub>2</sub> bubbling at ambient temperature for three hours, using a modification of the method described by Ren.<sup>51</sup>

#### 7.4.3 Analysis

Ionic liquid water contents were determined using a Mettler-Toledo Karl Fischer titrator.

Electrical testing was performed using a VersaStat 3 Potentiostat. Cyclic voltammograms were recorded between 1.5 and -1.5 V, using a 1 V/s scan rate for five cycles. In order to calculate specific capacitance, the absolute value of the forward and reverse sweep currents measured at 0 V were averaged for each sample; this number was then divided by the scan rate and the cross-sectional area of the sample (0.317 cm<sup>2</sup>).

Thermogravimetric analysis (TGA) was performed on the neat and reclaimed ILs, the as-prepared ionogels, and the recovered silica slurry material as described previously.<sup>38</sup>

## 7.5 References

Reprinted (adapted) with permission from:

Horowitz, A. I., Wang, Y., & Panzer, M. J. *Green Chem.*, **15**, 3414 – 3420 (2013)

Copyright The Royal Society of Chemistry, 2013.

1. Armand, M., Endres, F., MacFarlane, D. R., Ohno, H. & Scrosati, B. Ionic-liquid materials for the electrochemical challenges of the future. *Nat. Mater.* **8**, 621–629 (2009).
2. Earle, M. J. & Seddon, K. R. Ionic liquids. Green solvents for the future. *Pure Appl. Chem.* **72**, 1391–1398 (2000).
3. Rogers, R. D. CHEMISTRY: Ionic Liquids--Solvents of the Future? *Science* **302**, 792–793 (2003).
4. Zhang, Y., Bakshi, B. R. & Demessie, E. S. Life Cycle Assessment of an Ionic Liquid versus Molecular Solvents and Their Applications. *Environ. Sci. Technol.* **42**, 1724–1730 (2008).
5. Welton, T. Room-Temperature Ionic Liquids. Solvents for Synthesis and Catalysis. *Chem. Rev.* **99**, 2071–2084 (1999).
6. Galiński, M., Lewandowski, A. & Stępnia, I. Ionic liquids as electrolytes. *Electrochimica Acta* **51**, 5567–5580 (2006).
7. Aprile, C. *et al.* New ionic liquid-modified silica gels as recyclable materials for l-proline- or H-Pro-Pro-Asp-NH<sub>2</sub>-catalyzed aldol reaction. *Green Chem.* **9**, 1328–1334 (2007).

8. Yadav, J. ., Reddy, B. V. ., Basak, A. . & Venkat Narsaiah, A. Recyclable 2nd generation ionic liquids as green solvents for the oxidation of alcohols with hypervalent iodine reagents. *Tetrahedron* **60**, 2131–2135 (2004).
9. Zhang, X., Fan, X., Niu, H. & Wang, J. An ionic liquid as a recyclable medium for the green preparation of  $\alpha,\alpha'$ -bis (substituted benzyldiene)cycloalkanones catalyzed by  $\text{FeCl}_3 \cdot 6\text{H}_2\text{O}$ . *Green Chem.* **5**, 267–269 (2003).
10. Wong, H., Pink, C. J., Ferreira, F. C. & Livingston, A. G. Recovery and reuse of ionic liquids and palladium catalyst for Suzuki reactions using organic solvent nanofiltration. *Green Chem.* **8**, 373–379 (2006).
11. Lewandowski, A., Olejniczak, A., Galinski, M. & Stepniak, I. Performance of carbon–carbon supercapacitors based on organic, aqueous and ionic liquid electrolytes. *J. Power Sources* **195**, 5814–5819 (2010).
12. Lewandowski, A. & Galiński, M. Carbon–ionic liquid double-layer capacitors. *J. Phys. Chem. Solids* **65**, 281–286 (2004).
13. Kralisch, D., Stark, A., Körsten, S., Kreisel, G. & Ondruschka, B. Energetic, environmental and economic balances: Spice up your ionic liquid research efficiency. *Green Chem.* **7**, 301–309 (2005).
14. Ranke, J., Stolte, S., Störmann, R., Arning, J. & Jastorff, B. Design of Sustainable Chemical ProductsThe Example of Ionic Liquids. *Chem. Rev.* **107**, 2183–2206 (2007).



15. Ranke, J. *et al.* Lipophilicity parameters for ionic liquid cations and their correlation to in vitro cytotoxicity. *Ecotoxicol. Environ. Saf.* **67**, 430–438 (2007).
16. Kulacki, K. J. & Lamberti, G. A. Toxicity of imidazolium ionic liquids to freshwater algae. *Green Chem.* **10**, 104–110 (2008).
17. Ventura, S. P. M. *et al.* Designing ionic liquids: the chemical structure role in the toxicity. *Ecotoxicology* **22**, 1–12 (2012).
18. Zhao, D., Liao, Y. & Zhang, Z. Toxicity of Ionic Liquids. *CLEAN – Soil Air Water* **35**, 42–48 (2007).
19. Capello, C., Fischer, U. & Hungerbühler, K. What is a green solvent? A comprehensive framework for the environmental assessment of solvents. *Green Chem.* **9**, 927–934 (2007).
20. Harjani, J. R., Farrell, J., Garcia, M. T., Singer, R. D. & Scammells, P. J. Further investigation of the biodegradability of imidazolium ionic liquids. *Green Chem.* **11**, 821–829 (2009).
21. Megaw, J., Busetti, A. & Gilmore, B. F. Isolation and Characterisation of 1-Alkyl-3-Methylimidazolium Chloride Ionic Liquid-Tolerant and Biodegrading Marine Bacteria. *PLoS ONE* **8**, e60806 (2013).
22. Seff, B. EMD Performance Materials Corp. Quotation. (2015).
23. Earle, M. J., McCormac, P. B. & Seddon, K. R. Diels–Alder reactions in ionic liquids. A safe recyclable alternative to lithium perchlorate–diethyl ether mixtures. *Green Chem.* **1**, 23–25 (1999).

24. Dibble, D. C. *et al.* A facile method for the recovery of ionic liquid and lignin from biomass pretreatment. *Green Chem.* **13**, 3255–3264 (2011).
25. Wu, B., Liu, W., Zhang, Y. & Wang, H. Do We Understand the Recyclability of Ionic Liquids? *Chem. - Eur. J.* **15**, 1804–1810 (2009).
26. Le Bideau, J., Viau, L. & Vioux, A. Ionogels, ionic liquid based hybrid materials. *Chem. Soc. Rev.* **40**, 907–925 (2011).
27. Patel, M., Gnanavel, M. & Bhattacharyya, A. J. Utilizing an ionic liquid for synthesizing a soft matter polymer ‘gel’ electrolyte for high rate capability lithium-ion batteries. *J. Mater. Chem.* **21**, 17419–17424 (2011).
28. Zhang, S., Lodge, T. P. & Frisbie, C. D. Electrical Impedance of Spin-Coatable Ion Gel Films. *J Phys Chem B* **115**, 3315–3321 (2011).
29. Susan, M. A. B. H., Kaneko, T., Noda, A. & Watanabe, M. Ion Gels Prepared by in Situ Radical Polymerization of Vinyl Monomers in an Ionic Liquid and Their Characterization as Polymer Electrolytes. *J. Am. Chem. Soc.* **127**, 4976–4983 (2005).
30. El-Kady, M. F. & Kaner, R. B. Scalable fabrication of high-power graphene micro-supercapacitors for flexible and on-chip energy storage. *Nat. Commun.* **4**, 1475 (2013).
31. Néouze, M.-A., Bideau, J. L., Gaveau, P., Bellayer, S. & Vioux, A. Ionogels, New Materials Arising from the Confinement of Ionic Liquids within Silica-Derived Networks. *Chem. Mater.* **18**, 3931–3936 (2006).

32. Ueno, K., Hata, K., Katakabe, T., Kondoh, M. & Watanabe, M.  
Nanocomposite Ion Gels Based on Silica Nanoparticles and an Ionic Liquid:  
Ionic Transport, Viscoelastic Properties, and Microstructure. *J. Phys. Chem. B*  
**112**, 9013–9019 (2008).
33. Ueno, K. & Watanabe, M. From Colloidal Stability in Ionic Liquids to  
Advanced Soft Materials Using Unique Media. *Langmuir* **27**, 9105–9115  
(2011).
34. Gayet, F. *et al.* Polymer nanocomposite ionogels, high-performance  
electrolyte membranes. *J. Mater. Chem.* **20**, 9456–9462 (2010).
35. Gayet, F. *et al.* Unique Combination of Mechanical Strength, Thermal  
Stability, and High Ion Conduction in PMMA–Silica Nanocomposites  
Containing High Loadings of Ionic Liquid. *Chem. Mater.* **21**, 5575–5577  
(2009).
36. He, Y., Boswell, P. G., Bühlmann, P. & Lodge, T. P. Ion Gels by Self-  
Assembly of a Triblock Copolymer in an Ionic Liquid <sup>†</sup>. *J. Phys. Chem. B*  
**111**, 4645–4652 (2007).
37. Visentin, A. F. & Panzer, M. J. Poly(Ethylene Glycol) Diacrylate-Supported  
Ionogels with Consistent Capacitive Behavior and Tunable Elastic Response.  
*ACS Appl. Mater. Interfaces* **4**, 2836–2839 (2012).
38. Horowitz, A. I. & Panzer, M. J. High-performance, mechanically compliant  
silica-based ionogels for electrical energy storage applications. *J. Mater.*  
*Chem.* **22**, 16534–16539 (2012).

39. Vioux, A., Viau, L., Volland, S. & Le Bideau, J. Use of ionic liquids in sol-gel; ionogels and applications. *Comptes Rendus Chim.* **13**, 242–255 (2010).
40. Marins, J. A., Soares, B. G., Silva, A. A., Hurtado, M. G. & Livi, S. Electrorheological and dielectric behavior of new ionic liquid/silica systems. *J. Colloid Interface Sci.* **405**, 64–70 (2013).
41. Delahaye, E. *et al.* Silica ionogels for proton transport. *J. Mater. Chem.* **22**, 17140–17146 (2012).
42. Néouze, M.-A., Bideau, J. L., Leroux, F. & Vioux, A. A route to heat resistant solid membranes with performances of liquid electrolytes. *Chem. Commun.* 1082–1084 (2005). doi:10.1039/b416267f
43. Néouze, M.-A., Le Bideau, J. & Vioux, A. Versatile heat resistant solid electrolytes with performances of liquid electrolytes. *Prog. Solid State Chem.* **33**, 217–222 (2005).
44. Dai, S. *et al.* Preparation of silica aerogel using ionic liquids as solvents. *Chem. Commun.* **3**, 243–244 (2000).
45. Klingshirn, M. A., Spear, S. K., Holbrey, J. D. & Rogers, R. D. Ionic liquids as solvent and solvent additives for the synthesis of sol-gel materials. *J. Mater. Chem.* **15**, 5174–5180 (2005).
46. Zhou, Y., Schattka, J. H. & Antonietti, M. Room-Temperature Ionic Liquids as Template to Monolithic Mesoporous Silica with Wormlike Pores via a Sol-Gel Nanocasting Technique. *Nano Lett.* **4**, 477–481 (2004).
47. Hench, L. L. & West, J. K. The sol-gel process. *Chem. Rev.* **90**, 33–72 (1990).

48. Jacquemin, J., Husson, P., Padua, A. A. H. & Majer, V. Density and viscosity of several pure and water-saturated ionic liquids. *Green Chem.* **8**, 172–180 (2006).
49. O'Mahony, A. M., Silvester, D. S., Aldous, L., Hardacre, C. & Compton, R. G. Effect of Water on the Electrochemical Window and Potential Limits of Room-Temperature Ionic Liquids. *J. Chem. Eng. Data* **53**, 2884–2891 (2008).
50. Ranke, J., Othman, A., Fan, P. & Müller, A. Explaining Ionic Liquid Water Solubility in Terms of Cation and Anion Hydrophobicity. *Int. J. Mol. Sci.* **10**, 1271–1289 (2009).
51. Ren, S., Hou, Y., Wu, W. & Liu, W. Purification of Ionic Liquids: Sweeping Solvents by Nitrogen. *J. Chem. Eng. Data* **55**, 5074–5077 (2010).
52. Widegren, J. A. & Magee, J. W. Density, Viscosity, Speed of Sound, and Electrolytic Conductivity for the Ionic Liquid 1-Hexyl-3-methylimidazolium Bis(trifluoromethylsulfonyl)imide and Its Mixtures with Water <sup>†</sup>. *J. Chem. Eng. Data* **52**, 2331–2338 (2007).
53. Shamsipur, M., Beigi, A. A. M., Teymouri, M., Pourmortazavi, S. M. & Irandoust, M. Physical and electrochemical properties of ionic liquids 1-ethyl-3-methylimidazolium tetrafluoroborate, 1-butyl-3-methylimidazolium trifluoromethanesulfonate and 1-butyl-1-methylpyrrolidinium bis(trifluoromethylsulfonyl)imide. *J. Mol. Liq.* **157**, 43–50 (2010).
54. Seki, S. *et al.* Physicochemical and Electrochemical Properties of 1-Ethyl-3-Methylimidazolium Tris (pentafluoroethyl) trifluorophosphate and 1-Ethyl-3-

Methylimidazolium Tetracyanoborate. *J. Electrochem. Soc.* **159**, A967–A971 (2012).

55. Huddleston, J. G. *et al.* Characterization and comparison of hydrophilic and hydrophobic room temperature ionic liquids incorporating the imidazolium cation. *Green Chem.* **3**, 156–164 (2001).

## Chapter 8

### Poly(dimethylsiloxane)-Supported Ionogels with High Ionic Liquid Loading

#### 8.1 Introduction

Supported ionic liquid-based composites, also known as “ionogels,” have garnered interest in recent years as they offer many of the benefits of ionic liquids (ionic conductivity, nonvolatility, nonflammability) in an immobilized solid or solid-like form. These novel hybrid materials are being considered for use as catalytic or separation membranes, as well as solid electrolytes for energy storage devices.<sup>1–21</sup> Researchers have explored a multitude of different materials as the solid scaffold material for the fabrication of ionogels. Inorganic oxide supports, especially silica scaffolds (prepared both via *ex situ* addition of nanoparticles and *in situ* sol-gel reactions) are straightforward to integrate with an IL and do not limit the thermal stability of the final product.<sup>18–21</sup> A few researchers have proposed organic/inorganic hybrid supports to improve mechanical characteristics while maintaining high thermal stability.<sup>16,17</sup> However, the complex syntheses of these hybrid scaffolds often require long reaction times at elevated temperatures.

Much of the literature characterizes gels containing organic polymer supports, which can demonstrate a flexible mechanical character.<sup>7–15</sup> However, many polymers possess limited thermal stability. Moreover, the choice of polymer is often restricted by the limited miscibility of certain polymers in ILs, especially at high degrees of polymerization. Another approach has been to employ co-solvents to overcome immiscibility barriers; however, this necessitates both time- and

energy-intensive drying periods.<sup>11,12</sup> As a result, there is great interest in understanding the limits of polymer solubility in ILs and how one might overcome them.<sup>1,22,23</sup>

Poly(dimethylsiloxane) (PDMS) is a well-known inorganic polymer with a large variety of industrial applications. The popularity of PDMS is due to its many favorable properties, which include optical transparency, elasticity, and stability with respect to a large range of chemical and thermal stresses compared to many organic polymers.<sup>24</sup> The high thermal and chemical stability of PDMS make it an intriguing candidate for use as the supporting scaffold material in ionogels. However, PDMS is immiscible with many ILs of interest. While IL/PDMS combinations using commercial PDMS kits have been proposed in the field of separation membranes, these materials are ionic liquid-poor due to the difficulty in uniformly combining the IL and PDMS, and have therefore been of limited utility.<sup>25–27</sup> This report describes a facile method to overcome the immiscibility between PDMS and ILs to create PDMS-supported ionogels with high ionic liquid loading. This new class of materials demonstrates elastic mechanical response, favorable electrical performance when used as a solid electrolyte, and high thermal stability.



## 8.2 Results and Discussion

### 8.2.1 Synthetic Approach and Ionogel Structure

PDMS-supported ionogels are formed via a simple, in situ sol-gel reaction to create a crosslinked PDMS network from a functionalized PDMS oligomer, using formic acid (FA) as a catalyst. This reaction scheme was first used with simple silicon alkoxides such as tetramethyl- or tetraethylorthosilicate (TMOS, TEOS).<sup>20,28</sup> It is well-suited for the preparation of ionogels, as unlike some acid-catalyzed sol-gel reactions, all of the reactive byproducts are volatile (*e.g.* ethanol, water) and evaporate within days of ionogel casting.<sup>21</sup> Moreover, FA, TMOS, and TEOS are soluble in many ILs of interest. In this incarnation, the silicon source is a PDMS oligomer with triethoxyethylsilyl-terminated end groups (f-PDMS, MW = 700 – 900). These functionalized end groups serve as three reactive sites per oligomer end, analogous to the four reactive sites of TEOS.

To overcome the immiscibility of f-PDMS and the IL, it is necessary to stir a mixture of FA, IL, and f-PDMS until a stable resin is obtained (Figure 8.1a). At this point, the mixture can be cast and allowed to cure in situ to produce a solid, free-standing gel (Figure 8.1b). The end groups of the f-PDMS must come into proximity with the FA in the IL phase in order to react. Agitating the system during reaction creates a co-mingled mixture of the growing PDMS network within the IL. The result is a sponge-like structure (Figure 8.1c), with domains of pure IL contained within a porous scaffold of PDMS. By following this synthetic strategy, PDMS-supported ionogels with high IL loadings may be realized using a

variety of different ILs. PDMS-supported ionogels incorporating large mass fractions of 1-ethyl-3-methylimidazolium bis(trifluoromethylsulfonyl)imide (EMI TFSI), 1-butyl-3-methylpyrrolidinium (BMP) TFSI, and EMI tetracyanoborate (TCB) have all been successfully created using this approach, as well as ionogels incorporating lithium TFSI. This report focuses on the properties of pure EMI TCB-based ionogels due to the outstanding conductivity of this IL.<sup>14</sup> For the formulation used in this study, a 30 minute mixing time is required to produce a resin, which then cures over several hours to create ionogels that contain 80% IL by mass, as compared to 5–50% for previous reports.<sup>25–27</sup>

The structure of PDMS-supported ionogels (Figure 8.1c) is significantly different than that of some other ionogel types, especially silica-supported ionogels wherein nanostructured silica is in intimate contact with the IL throughout the ionogel.<sup>18,22</sup> The PDMS scaffold sparsely crosslinked, with a molecular weight between crosslinks of ~11,000 g/mol. However, all oligomer chains are incorporated into the final scaffold structure (Appendix D, Figure D1). This is consistent with the result that the sol-gel reaction network may terminate at different extents of condensation, rather than proceeding to complete crosslinking at every reactive site.<sup>29</sup> Furthermore, despite the comparatively open pore structure of the PDMS-supported ionogels, free-standing samples display no IL leakage over time. PDMS-supported ionogels are also stable upon exposure to water, and as a result can mitigate concerns regarding water infiltration, which can limit the operating voltage of electrochemical devices.

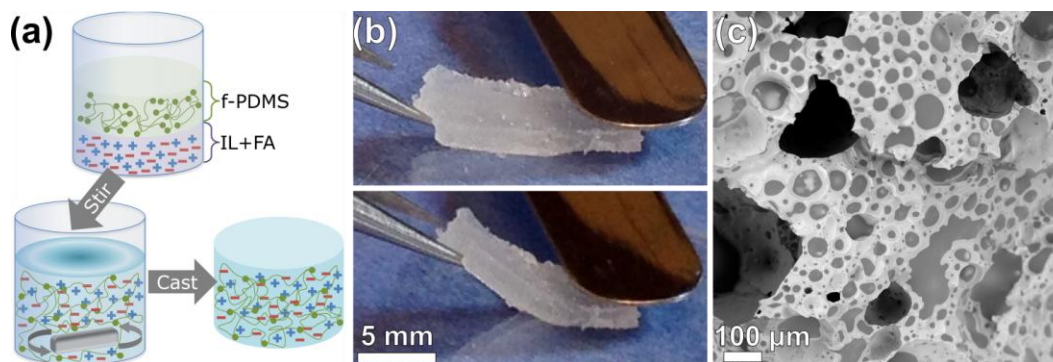


**Figure 8.1.** Preparation scheme and images of PDMS ionogels. (a) Photograph highlighting the immiscibility between the f-PDMS and IL layers without agitation and schematic diagram of the preparation of PDMS ionogels. The liquid f-PDMS oligomer of lower density (top layer) is not miscible with the ionic liquid/formic acid (IL+FA) solution (bottom layer). The crosslinking sol-gel reaction is initiated upon stirring the mixture; after a sufficient period of mixing, the resin can be cast into any arbitrary shape, resulting in a free-standing material containing the IL intermixed with crosslinked PDMS; (b) Photographs of an unbent (top) and bent (bottom) sample of PDMS ionogel, demonstrating ionogel flexibility. (c) SEM image of ionogel structure, showing the ionic liquid (dark grey regions) immobilized by a solid, sponge-like PDMS scaffold (lighter regions).

### 8.2.2 Properties of PDMS-Supported Ionogels

The ionogel displays an elastic modulus of approximately 60 kPa and demonstrates elastic deformation up to at least 30% compressive strain with only minor hysteresis (Figure 8.2). Signs of yield begin at ~45% strain, after which the hysteretic effect is increased. Despite containing 80% IL by mass, the ionogel shows solid-like behavior over a wide frequency range (Figure 8.2, inset). Some stiffening is observed at high frequencies, in agreement with previous reports.<sup>30</sup> PDMS-supported ionogels can withstand over 5000 cycles of mechanical stress and maintain mechanical integrity above 200 °C (Appendix D, Figures D2-D3).

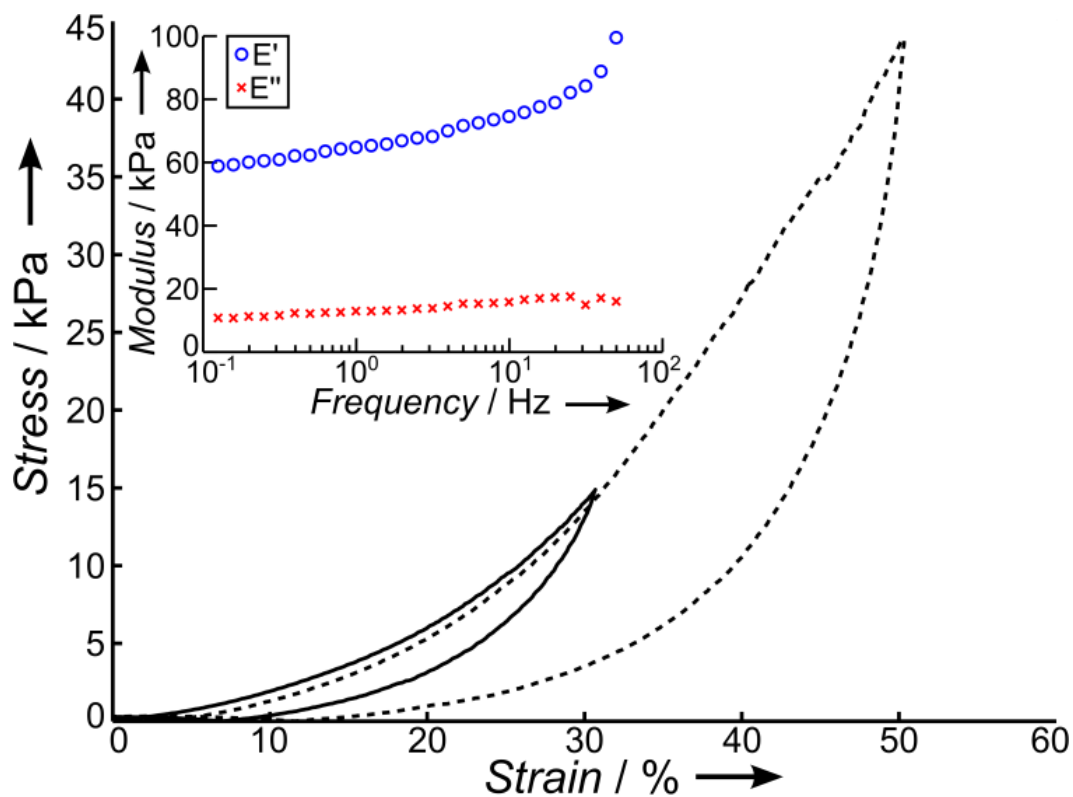


**Figure 8.2.** Ionogel mechanical characteristics. Stress-strain curves show elastic deformation until at least 30% compressive strain, with only minor hysteresis. Signs of yield are initially seen at roughly 45% strain. (Inset) Frequency sweep of ionogel dynamic mechanical response, showing some stiffening at high frequencies. The storage modulus ( $E'$ ) is larger than the loss modulus ( $E''$ ) across the frequency range studied, indicating solid-like behavior.

The crosslinked PDMS scaffold is thermally stable until at least 200 °C (Figure 8.3). The DSC trace of PDMS-supported ionogels shows only the EMI TCB melting transition, which occurs at 10 °C. No glass or melting transitions of PDMS occur within the studied temperature range.<sup>31</sup> The DSC trace of pure PDMS shows a broad transition above 0° C that indicates the presence of unreacted f-PDMS end groups and disappears after annealing the sample at 50° C for several hours. No such transition is observed in the DSC trace of the as-prepared PDMS-supported ionogel. Similarly, a disappearance of some of the peaks associated with the reactive end groups of f-PDMS can be observed in the FTIR spectrum of the ionogel (Appendix D, Figure D4).

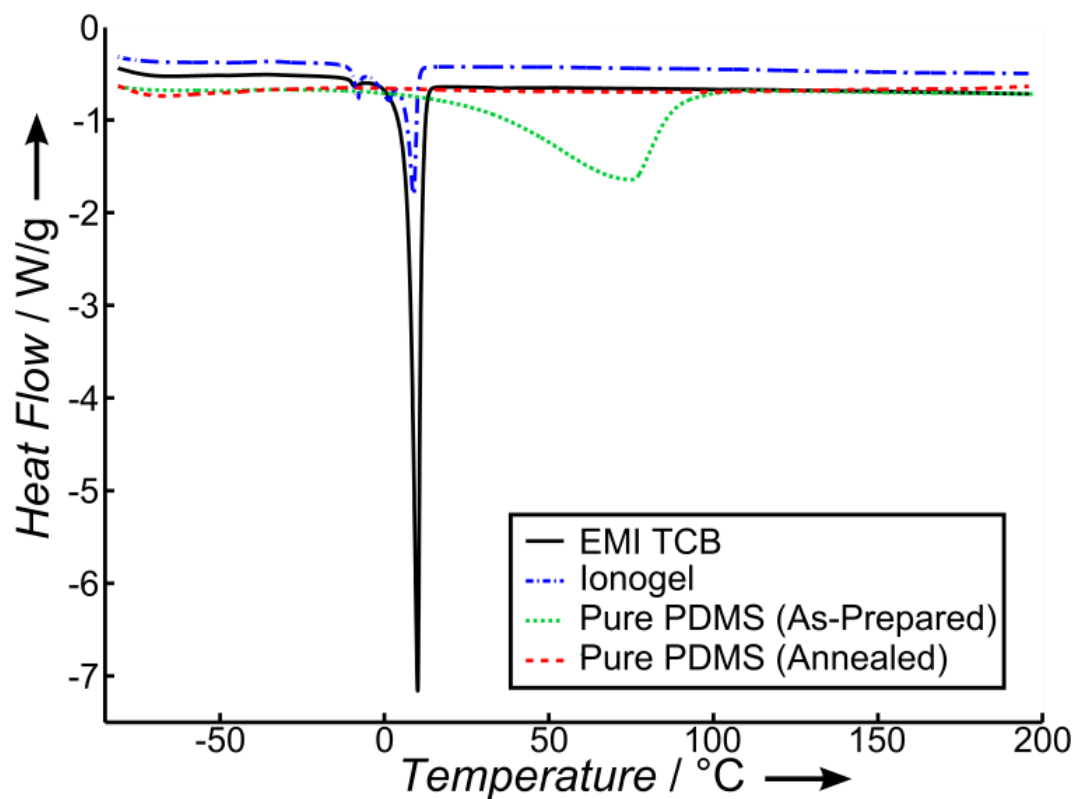


**Figure 8.3.** DSC heating traces for the neat ionic liquid (EMI TCB), PDMS-supported ionogel, and pure PDMS both as-prepared and post-annealing. Both EMI TCB and the ionogel show an IL melting peak at 10 °C. The as-prepared PDMS trace shows a broad transition in the 20 – 75 °C range, indicating the presence of unreacted end groups. This transition disappears after the PDMS is annealed at 50 °C for several hours. The ionogel shows no such transition, indicating that the scaffold crosslinking reaction is complete.

The PDMS-supported ionogels described here are suitable for use as solid electrolytes in supercapacitor devices, with an ionic conductivity at room temperature of 3.1 mS/cm, well above the 1 mS/cm benchmark desired for use in electrochemical devices (Figure 8.4).<sup>32</sup> When tested in a double-layer capacitor structure, PDMS ionogels also demonstrate clear capacitive behavior (Appendix D, Figure D5). While the conductivity of PDMS-supported ionogels is lower than that of neat EMI TCB (12.6 mS/cm), the observed activation energy of ionic conductivity for the ionogel (14.6 kJ/mol) is nearly identical to that of the neat IL (14.4 kJ/mol) and similar previously-reported values for EMI TCB-based ionogels.<sup>14</sup> The incorporation of scaffold materials with which ILs are miscible has been shown to lead to changes in the activation energy of conductivity for the corresponding ionogels.<sup>7</sup> This result reinforces the notion that for ionogels with immiscible IL/scaffold pairs, there exists only a physical barrier to ionic motion due to the presence of the scaffold, as opposed to any thermally-sensitive energetic or chemical interactions between the IL and the solid support. With continued optimization of the fabrication process, it is expected that the minimum achievable scaffold content for PDMS-supported ionogels can be further reduced, leading to larger values of ionogel conductivity.

The conductivity of Li<sup>+</sup>-bearing ionogels was measured to be 2.2 mS/cm. Such gels may be useful for battery applications. The decrease in conductivity is attributable to the well-known increase in the viscosity of lithium-in-IL solutions as compared to neat ILs.



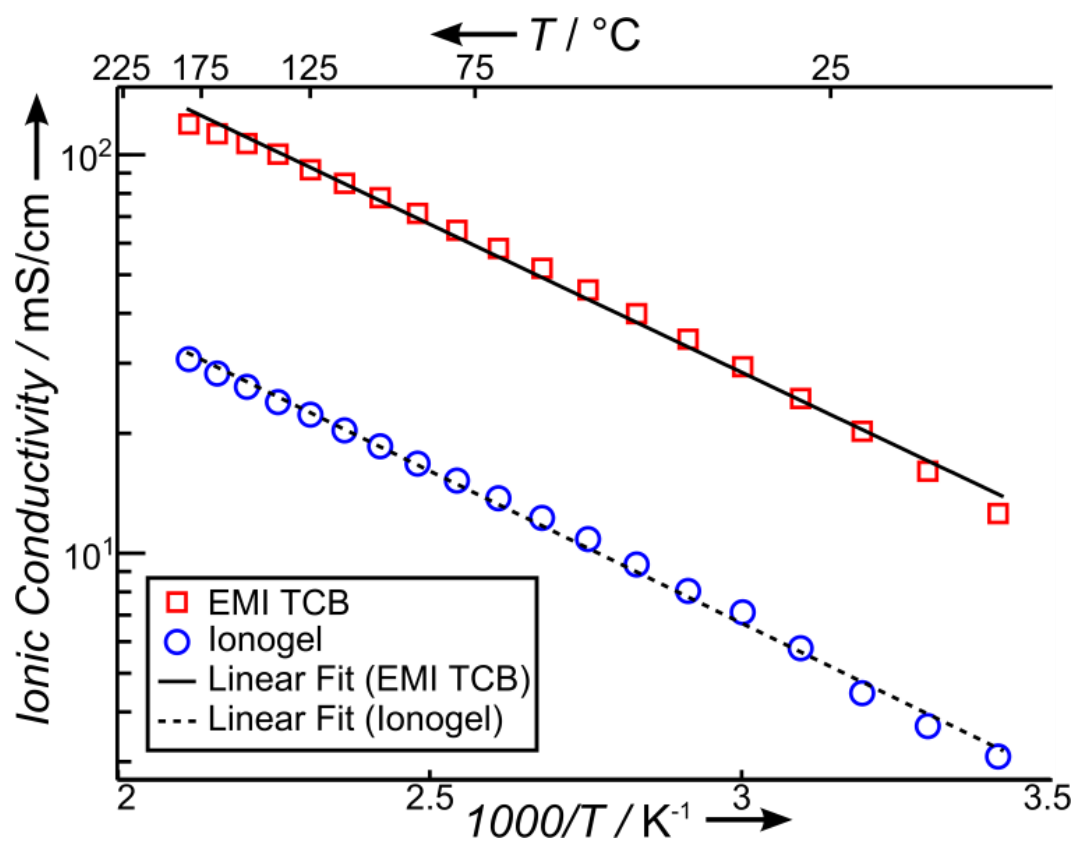


**Figure 8.4.** Arrhenius plots of ionic conductivity for a PDMS-supported ionogel and for neat EMI TCB. Ionic conductivity of the ionogel is lower than that of the neat IL, but the two activation energies are nearly identical.

### 8.3 Conclusion

Ionogels are an emerging class of materials with tremendous potential for use in a variety of applications. By employing a simple sol-gel reaction at ambient conditions, a new manifestation of ionogel containing a PDMS scaffold has been fabricated, overcoming the barrier of immiscibility between PDMS and ILs or lithium-in-IL solutions. The ionogels described here demonstrate a favorable combination of thermal stability, ionic conductivity, and elastic mechanical behavior. Moreover, they exhibit an activation energy of conductivity nearly identical to that of the neat ionic liquid. In addition to the favorable combination of properties exhibited by PDMS-supported ionogels, the synthetic technique employed here offers insight into how ILs may be combined with otherwise incompatible scaffold materials more generally, thereby opening the door to the further creation of novel ionogels.

## 8.4 Experimental Materials and Methods

### 8.4.1 Chemicals

Synthesis grade 1-ethyl-3-methylimidazolium bis(trifluoromethylsulfonyl)imide (EMI TFSI) and 1-butyl-3-methylpyrrolidinium (BMP) TFSI, and Solarpur grade (99.5%) 1-ethyl-3-methylimidazolium tetracyanoborate (EMI TCB) were purchased from EMD Millipore. Formic acid (FA, 98%) was purchased from Sigma Aldrich. Triethoxysilylethyl-terminated poly(dimethylsiloxane) (f-PDMS, 95%, MW 700 - 900) was purchased from Gelest. All chemicals were used as received.

### 8.4.2 Ionogel Preparation

All ionogel precursor solutions were prepared using a 1:13 molar ratio of f-PDMS to formic acid. The solutions consisted of 50% IL by volume. Reagents were injected into a vial containing a magnetic stir bar. Solutions to make EMI TCB-based ionogels were then stirred at ~1000 RPM for 1-2 minutes, followed by stirring at ~500 RPM for 30 minutes to obtain a resin. Initially, rapid stirring is required to overcome the viscosity of the IL and f-PDMS and ensure that the solution is thoroughly mixed. However, prolonged stirring at a high rate leads to re-separation of the phases due to the high shear forces experienced by the sample. Stirring at a low rate for a longer time prevents the sample from phase separating while the reaction proceeds. The required stir pattern varies depending on the formulation and identity of the IL. EMI TFSI and BMP TFSI-based

solutions require stirring at ~1000 RPM for 10 minutes (these ILs are more viscous than EMI TCB), followed by stirring at ~300 RPM for 15 minutes to produce a stable resin.

After a resin was obtained, samples for thermal testing were then allowed to react overnight in the sealed vial, undisturbed. In order to prepare samples for mechanical and electrical testing, the resin was poured into PTFE molds, which were then sealed and allowed to cure overnight. After opening the molds, samples were allowed to rest for several days at ambient temperature before testing to ensure the evaporation of all volatile byproducts.

#### 8.4.3 Lithium-Bearing Ionogel Preparation

Lithium-bearing ionogels were prepared by first preparing a 0.175 M solution of LiTFSI in EMI TCB. This solution was stirred at ~1000 RPM for 15 minutes to ensure full dissolution of the lithium salt. FA and f-PDMS were then added in a 1:13 molar ratio of f-PDMS to FA. As the Li solution was more viscous than the neat IL, this mixture initially required an increased stirring rate of ~1200 rpm. This was reduced to ~700 rpm after five minutes, and then further reduced to ~300 rpm for an additional 15 minutes before samples were cast as described above.

#### 8.4.4 Preparation of Pure PDMS

Pure PDMS can be prepared using this method by stirring a mixture of f-PDMS and FA at ~1000 RPM for 5-10 minutes. Pure PDMS samples used in this

investigation were prepared from solutions with a 1:13 molar ratio of f-PDMS to FA. For DSC investigations, “annealed” samples were heated at 50 °C for several hours using a hot plate under ambient conditions.

#### 8.4.5 Thermal Testing

A TA Instruments Q500 thermogravimetric analyzer (TGA) was used to determine ionogel composition and thermal stability. For thermal stability tests, samples were subjected to a 10 °C/min ramp from ambient temperature to 625 °C. To determine ionogel composition, a stepped program was used to isolate the EMI TCB decomposition transition at 425 °C. The mass loss experienced during that transition was normalized by the mass loss experienced by neat EMI TCB.

A TA Instruments Q100 differential scanning calorimeter (DSC) was used to verify that the sol-gel reaction was complete. Samples were first heated to 40 °C to erase thermal history, followed by cooling to at least -80 °C and heating to 200 °C. The cooling rate was 5 °C/min, and the heating rate was 10 °C/min.

#### 8.4.6 Mechanical Testing

A TA Instruments RSA III dynamic mechanical analyzer (DMA) was used for mechanical testing. Samples were cast into PTFE molds with a cross-sectional area of 0.32 cm<sup>2</sup> and a thickness of 0.32 cm. Samples were tested via unconfined compression. Stress-strain curves were obtained using a compression rate of 0.015 mm/min. The complex elastic modulus was measured at 5% strain after a 10 g preloading, over a frequency range of 0.1 to 80 Hz. Fatigue tests were measured

at 10% strain using a frequency of 1 Hz.

#### 8.4.7 Electrical Testing

Ionic conductivity values were obtained by electrical impedance spectroscopy (EIS) using a Princeton Applied Research VersaStat 3 potentiostat with a built-in frequency response analyzer. Spectra employed a 10 mV RMS oscillation around 0 V vs. open circuit and were measured over the frequency range 0.1 Hz to 1 MHz. To obtain room temperature ionic conductivity values, ionogel and neat EMI TCB samples were tested in a parallel-plate configuration using planar glassy carbon blocking electrodes. Samples were bounded with a PTFE ring of area 0.32 cm<sup>2</sup> and thickness 0.16 cm. Ionic conductivity was calculated as:

$$(8.1) \quad \sigma = t/AZ'$$

where  $t$  and  $A$  are the thickness and cross-sectional area of the sample, respectively, and  $Z'$  is the real component of impedance measured at the minimum phase angle frequency (100 kHz for neat EMI TCB, 5 kHz for the ionogel samples). For the ionic conductivity vs. temperature tests, samples were placed on a Linkam Instruments LTS420 temperature stage. Electrical contact was made by insertion of two pin probes into the samples, with a probe separation distance of 0.25 inches. EIS spectra were recorded at 10 °C intervals from 20 to 200 °C. Samples were allowed time to reach thermal equilibrium at each temperature. Ionic conductivity values were calculated using a geometrical correction factor, equating the conductivity of the sample at room temperature with that measured in the parallel-plate setup. Although the Vogel-Fulcher-Tammann equation is

often used for fitting ionic liquid conductivity data, the Arrhenius equation was used to calculate the activation energy of conductivity, as linear fits yielded  $R^2$  values above 0.99.

#### 8.4.8 FTIR Testing

Spectra were collected using a JASCO Corporation FT/IR-6200 by conducting 100 scans.

#### 8.4.9 Water Stability Testing

The stability of ionogels with respect to water was tested following the procedure described previously.<sup>33</sup> No liberation of the IL was observed upon submersion in water.

#### 8.4.10 Gel Permeation Chromatography

Ionogel samples were examined using gel permeation chromatography (GPC) to ensure that all f-PDMS chains were effectively incorporated into the scaffold. A sample of ionogel was first immersed in THF for one week to ensure full dissolution of both the IL and free f-PDMS chains, if any were present. The supernatant liquid was then filtered through a 0.4 micron PTFE filter before being injected into a Shimadzu GPC system equipped with a TOSOH TSKgel GMHh-M mixed-bed column and guard column (5  $\mu\text{m}$ ), using both UV and refractive index detectors. The column was calibrated with low polydispersity poly(styrene) standards (TOSOH, PSt Quick Kit) with THF as the mobile phase eluting at 0.75

mL/min.

#### 8.4.11 Hexane Absorption

The extent of crosslinking in the PDMS scaffold was determined using a hexane absorption (polymer network swelling) test. Hexane was selected as it is known to solubilize PDMS chains but is immiscible with EMI TCB. An ionogel sample was first massed, and then immersed in an excess of hexane for one week to ensure sufficient opportunity for the hexane to diffuse throughout the ionogel scaffold. The sample was then removed and its mass quickly recorded to determine the amount of hexane absorbed.



## 8.5 References

Reprinted with permission from:

Horowitz, A. I. & Panzer, M. J. *Angew. Chemie.*, **126**, 9938 – 9941 (2014).

Copyright WILEY - VCH Verlag, 2014.

1. Le Bideau, J., Viau, L. & Vioux, A. Ionogels, ionic liquid based hybrid materials. *Chem. Soc. Rev.* **40**, 907–925 (2011).
2. Welton, T. Ionic liquids in catalysis. *Coord. Chem. Rev.* **248**, 2459–2477 (2004).
3. Moganty, S. S., Jayaprakash, N., Nugent, J. L., Shen, J. & Archer, L. A. Ionic-Liquid-Tethered Nanoparticles: Hybrid Electrolytes. *Angew. Chem. Int. Ed.* **49**, 9158–9161 (2010).
4. Gu, Y., Ogawa, C., Kobayashi, J., Mori, Y. & Kobayashi, S. A Heterogeneous Silica-Supported Scandium/Ionic Liquid Catalyst System for Organic Reactions in Water. *Angew. Chem. Int. Ed.* **45**, 7217–7220 (2006).
5. Xiong, Y., Liu, J., Wang, Y., Wang, H. & Wang, R. One-Step Synthesis of Thermosensitive Nanogels Based on Highly Cross-Linked Poly(ionic liquid)s. *Angew. Chem. Int. Ed.* **51**, 9114–9118 (2012).
6. Zhang, T. & Zhou, H. From Li-O<sub>2</sub> to Li-Air Batteries: Carbon Nanotubes/Ionic Liquid Gels with a Tricontinuous Passage of Electrons, Ions, and Oxygen. *Angew. Chem. Int. Ed.* **51**, 11062–11067 (2012).
7. Susan, M. A. B. H., Kaneko, T., Noda, A. & Watanabe, M. Ion Gels Prepared by in Situ Radical Polymerization of Vinyl Monomers in an Ionic Liquid and

- Their Characterization as Polymer Electrolytes. *J. Am. Chem. Soc.* **127**, 4976–4983 (2005).
8. Miranda, D. F., Versek, C., Tuominen, M. T., Russell, T. P. & Watkins, J. J. Cross-Linked Block Copolymer/Ionic Liquid Self-Assembled Blends for Polymer Gel Electrolytes with High Ionic Conductivity and Mechanical Strength. *Macromolecules* **46**, 9313–9323 (2013).
  9. Kim, D. W. & Chi, D. Y. Polymer-Supported Ionic Liquids: Imidazolium Salts as Catalysts for Nucleophilic Substitution Reactions Including Fluorinations. *Angew. Chem. Int. Ed.* **43**, 483–485 (2004).
  10. Branco, L. C., Crespo, J. G. & Afonso, C. A. M. Highly Selective Transport of Organic Compounds by Using Supported Liquid Membranes Based on Ionic Liquids. *Angew. Chem. Int. Ed.* **41**, 2771–2773 (2002).
  11. Gu, Y. *et al.* High Toughness, High Conductivity Ion Gels by Sequential Triblock Copolymer Self-Assembly and Chemical Cross-Linking. *J. Am. Chem. Soc.* **135**, 9652–9655 (2013).
  12. Lee, K. H., Zhang, S., Lodge, T. P. & Frisbie, C. D. Electrical Impedance of Spin-Coatable Ion Gel Films. *J. Phys. Chem. B* **115**, 3315–3321 (2011).
  13. Lee, J., Panzer, M. J., He, Y., Lodge, T. P. & Frisbie, C. D. Ion Gel Gated Polymer Thin-Film Transistors. *J. Am. Chem. Soc.* **129**, 4532–4533 (2007).
  14. Pandey, G. P. & Hashmi, S. A. Ionic liquid 1-ethyl-3-methylimidazolium tetracyanoborate-based gel polymer electrolyte for electrochemical capacitors. *J. Mater. Chem. A* **1**, 3372 (2013).

15. Visentin, A. F. & Panzer, M. J. Poly(Ethylene Glycol) Diacrylate-Supported Ionogels with Consistent Capacitive Behavior and Tunable Elastic Response. *ACS Appl. Mater. Interfaces* **4**, 2836–2839 (2012).
16. Gayet, F. *et al.* Unique Combination of Mechanical Strength, Thermal Stability, and High Ion Conduction in PMMA–Silica Nanocomposites Containing High Loadings of Ionic Liquid. *Chem. Mater.* **21**, 5575–5577 (2009).
17. Le Bideau, J., Miah, M. Y., Vioux, A., Fajula, F. & Galarneau, A. Bimodal porous silica monoliths obtained by phase separation in non-aqueous media. *J. Mater. Chem.* **20**, 964–971 (2010).
18. Ueno, K., Hata, K., Katakabe, T., Kondoh, M. & Watanabe, M. Nanocomposite Ion Gels Based on Silica Nanoparticles and an Ionic Liquid: Ionic Transport, Viscoelastic Properties, and Microstructure. *J. Phys. Chem. B* **112**, 9013–9019 (2008).
19. Lu, Y., Das, S. K., Moganty, S. S. & Archer, L. A. Ionic Liquid-Nanoparticle Hybrid Electrolytes and their Application in Secondary Lithium-Metal Batteries. *Adv. Mater.* **24**, 4430–4435 (2012).
20. Néouze, M.-A., Le Bideau, J. & Vioux, A. Versatile heat resistant solid electrolytes with performances of liquid electrolytes. *Prog. Solid State Chem.* **33**, 217–222 (2005).
21. Horowitz, A. I. & Panzer, M. J. High-performance, mechanically compliant silica-based ionogels for electrical energy storage applications. *J. Mater. Chem.* **22**, 16534–16539 (2012).

22. Ueno, K., Fukai, T., Nagatsuka, T., Yasuda, T. & Watanabe, M. Solubility of Poly(methyl methacrylate) in Ionic Liquids in Relation to Solvent Parameters. *Langmuir* **30**, 3228–3235 (2014).
23. Winterton, N. Solubilization of polymers by ionic liquids. *J. Mater. Chem.* **16**, 4281 (2006).
24. Lötters, J. C., Olthuis, W., Veltink, P. H. & Bergveld, P. The mechanical properties of the rubber elastic polymer polydimethylsiloxane for sensor applications. *J. Micromechanics Microengineering* **7**, 145–147 (1997).
25. Izák, P. *et al.* Separation properties of supported ionic liquid–polydimethylsiloxane membrane in pervaporation process. *Desalination* **241**, 182–187 (2009).
26. Izák, P., Ruth, W., Fei, Z., Dyson, P. J. & Kragl, U. Selective removal of acetone and butan-1-ol from water with supported ionic liquid–polydimethylsiloxane membrane by pervaporation. *Chem. Eng. J.* **139**, 318–321 (2008).
27. Mai, N. L., Kim, S. H., Ha, S. H., Shin, H. S. & Koo, Y.-M. Selective recovery of acetone-butanol-ethanol from aqueous mixture by pervaporation using immobilized ionic liquid polydimethylsiloxane membrane. *Korean J. Chem. Eng.* **30**, 1804–1809 (2013).
28. Sharp, K. G. A two-component, non-aqueous route to silica gel. *J. Sol-Gel Sci. Technol.* **2**, 35–41 (1994).
29. Hench, L. L. & West, J. K. The sol-gel process. *Chem. Rev.* **90**, 33–72 (1990).

30. Winter, H. H. Analysis of Linear Viscoelasticity of a Crosslinking Polymer at the Gel Point. *J. Rheol.* **30**, 367 (1986).
31. Shefer, A. & Gottlieb, M. Effect of crosslinks on the glass transition temperature of end-linked elastomers. *Macromolecules* **25**, 4036–4042 (1992).
32. Schulze, M. W., McIntosh, L. D., Hillmyer, M. A. & Lodge, T. P. High-Modulus, High-Conductivity Nanostructured Polymer Electrolyte Membranes via Polymerization-Induced Phase Separation. *Nano Lett.* **14**, 122–126 (2014).
33. Horowitz, A. I., Wang, Y. & Panzer, M. J. Reclamation and reuse of ionic liquids from silica-based ionogels using spontaneous water-driven separation. *Green Chem.* **15**, 3414–3420 (2013).

## **Chapter 9**

### **Conclusions and Future Directions**

The preceding chapters have explored many of the benefits and possibilities of ionogels created through sol-gel. Overall, they paint a picture of an incredibly versatile process that is capable of being used to produce high-performance ionogels of multiple types. Moreover, they have demonstrated that the sol-gel reaction can be used to gain insight into the fundamentals of reactive and surface chemistry in IL media. However, there certainly exist more possible directions for inquiry to expand the investigations presented in this work.

#### **9.1 Future Directions**

##### **9.1.1 Hybrid Chemistries**

As discussed in the introduction, sol-gel processes can be used to create a wide variety of materials. These materials include functionalized silicon-based structures that include organic moieties, forming organic-inorganic hybrids<sup>1-17</sup> or silicones other than PDMS.<sup>18-20</sup> Such hybrids often have superior mechanical properties, with improved toughness and yield strength compared to pure silica monoliths.<sup>1-3</sup> Thin, tough, rubbery membranes such as those used for certain types of contact lenses can be produced using these methods.<sup>8</sup> Materials of this nature would be very useful for electrochemical energy storage applications as they would be suitable for the creation of very thin, flexible, robust devices.

Alternative chemistries leading to organic/inorganic hybrids and/or silicones can often be accomplished simply by substituting a silica precursor with four alkoxide groups (e.g. TMOS) for one with both alkoxide and organic groups (such as dimethoxydimethylsilane, DDMS, or methyltrimethoxysilane, MTMS). A large body of work exists describing such substitutions and their effects.<sup>12-17</sup> Hybrid organic/inorganic coatings and monoliths have been created using adaptations of FA/TMOS or FA/TEOS chemistry.<sup>9-11,18</sup> However, these reactions generally require the addition of several reagents other than FA and TMOS, and require very long reaction times (>10 days), elevated temperatures, or both. These conditions may pose processing drawbacks for the facile creation of devices.

Preliminary efforts have been made to create ionogels with mixtures of TMOS and DDMS. However, using relatively large DDMS:TMOS ratios leads to extremely long reaction times or a failure to gel, whereas small DDMS:TMOS ratios result in products that are very similar to ionogels made with pure TMOS. As such, more work remains to be done to discover how to form these alternative chemistries in an IL medium.

#### 9.1.2 Recycling in Other Ionogel Systems

The stability of ionogel systems with respect to various solvents is an important consideration for both the ease of processability and the robustness of the final device. Moreover, a thorough understanding of the interactions between ionogels and solvents may open the door to facile recycling of ILs from ionogel systems other than silica-supported ionogels. As discussed in the previous chapters, the IL can be removed from silica-supported ionogels both by dissolving

the IL in a compatible solvent (e.g. ethyl acetate) and by liberating the IL from the scaffold using spontaneous water-based separation. However, as PDMS is hydrophobic rather than hydrophilic, PDMS-supported ionogels are stable with respect to water.

The principle of spontaneous water-based separation is that the high affinity between water and the silica scaffold surface allows the water to infiltrate the ionogel and push out the IL.<sup>21</sup> Because the IL is immiscible with water, it forms a separate phase that can be easily isolated and purified. This principle is theoretically applicable to other ionogel systems. Many polar solvents (including ethyl acetate, acetone, tetrahydrofuran, dimethylsulfoxide, acetonitrile, and short-chain alcohols) have been shown experimentally to be miscible with ILs of interest. According to both experimental and published results,<sup>22–24</sup> longer-chain alcohols and alkanes (such as hexane) are generally immiscible with ILs of interest, while aromatic compounds may be sparingly soluble. The use of volatile organic compounds for IL recovery processes may present some environmental concerns that would mitigate the benefit of the use and re-use of ILs. However, the use of heavier liquids such as oils may be a more environmentally-friendly alternative.

The compatibility of water and alternative liquids with various scaffold systems has yet to be investigated. A simple combinatorial approach could be used to test whether any solvents are available that may liberate the IL from other scaffold types, such as polymers. Although some polymers may be hydrophilic enough to support the use of water, initial tests with PEG-DA (which is water-



soluble at low molecular weights) have not been successful. This indicates that the scaffold morphology may also play an important role in the success of a spontaneous liberation strategy. As such, further studies may also illuminate the nature of the interactions between the IL and scaffolds of different types.

### 9.1.3 High-Performance Devices with Ionogels

Although some device data is presented in the previous chapters, the focus of this work was the creation and characterization of novel ionogel materials through sol-gel. The data presented in Chapter 6 is important for understanding how silica-supported ionogels interact with porous, high surface area electrodes, but the devices characterized in that chapter do not exhibit exceptional performance. As such, one of the most important directions for further development is the creation of high-performance supercapacitors and batteries using ionogel electrolytes.

### 9.1.4 High-Performance Supercapacitors

The main barrier to the creation of high-performance supercapacitor devices is not the incorporation of ionogel electrolytes, but rather the development of highly conductive, robust, high surface area (HSA) electrodes.<sup>25</sup> Notably, the performance of the device made with a delayed-casting ionogel described in Chapter 6 is very close to that of the device made with only neat IL. However, the series resistance of both devices was in the range of thousands of ohms. This indicates that the graphene electrodes themselves were not sufficiently conductive to yield high performance metrics, and is in agreement with probe measurements

that found the in-plane resistance of graphene electrodes to be approximately 1 - 1.5 kOhms.

The laser-scribing technique used to create graphene electrodes was adapted from one first reported by the Kaner group.<sup>26-28</sup> However, the properties reported by the Kaner group were far superior to those achieved in this work. In particular, the series resistance of the devices described by the Kaner group was 16 ohms,<sup>26</sup> several orders of magnitude lower than that achieved by the work presented in Chapter 6. The most likely explanation for this discrepancy is that the Kaner group synthesized a graphene oxide dispersion in their lab, whereas the graphene oxide for the investigations described in Chapter 6 was commercially purchased. Parameters of the graphene oxide dispersion, such as flake size and extent of aggregation, were found to have a significant effect on the properties of the resultant graphene. A large performance increase was qualitatively observed when switching from a dispersion with >60% single-layer flakes to one with >80% single-layer flakes. A systematic study of the optimal flake size and dispersion properties using commercial materials could be undertaken to solve this problem.

In addition, the effective conductivity of HSA electrodes can be improved by the use of a current collector.<sup>29,30</sup> Current collectors are thin layers of a planar, highly-conductive material (usually a metal) that contact an HSA electrode throughout its projected surface area (Figure 9.1). Normally, contact to the rest of a circuit is made through the current collector. In this way, current must travel only through the thickness of the HSA layer, rather than the entire breadth of it, before reaching a low-resistance conductor. As the Kaner group did not

demonstrate the use of current collectors with laser-scribed graphene, such a demonstration would constitute a major contribution.

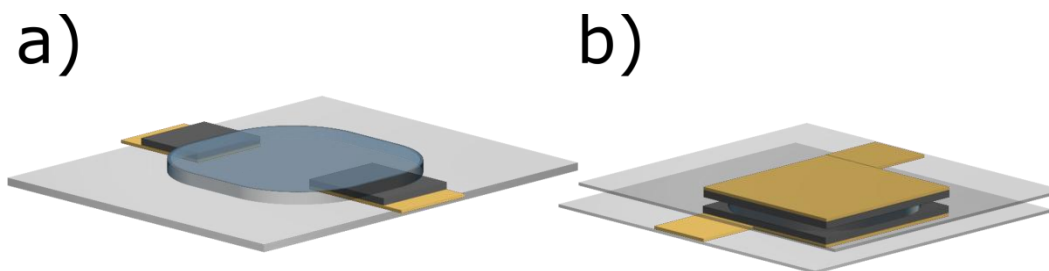


**Figure 9.1.** Diagrams of devices with current collectors, shown in gold. a) A coplanar device with gold current collector pads underneath graphene electrodes, with an ionogel layer lying on top. b) A sandwich device, with ionogel in between two layers of graphene, which lie entirely on top of two gold current collectors. The current collectors have tab leads to enable connection of a circuit.

Initial tests were performed to fabricate graphene electrodes with current collectors. These tests were performed by laying down a current collector layer made of either gold (through evaporation) or a 25 micron thick, multi-layer graphene sheet (also purchased from Graphene Supermarket) onto a flexible vinyl substrate. The substrate and current collectors were then covered with a very thin layer of graphene oxide and laser-scribing proceeded as described in Chapter 6. Graphene was successfully produced using a gold current collector, and electrical contact through the graphene layer to the gold was demonstrated. However, due to an incompatibility between the vinyl substrate and the vacuum chamber, the deposited gold layers themselves had resistances of hundreds of ohms, rather than the single-digit resistances expected of metallic gold. A substrate substitution should be attempted to overcome this barrier.

Graphene was not successfully produced using the graphene current collectors. It is theorized that this may be due to the thermal or optical properties of the current collector layer. The simplest way to approach this problem is by using a free-standing laser rather than an optical drive to perform the laser scribing. This would allow observations of the progress (or lack thereof) of the laser-scribing process to be easily made, simplifying the troubleshooting process. In addition, the use of a free-standing laser would greatly increase the versatility of the laser-scribing process, as it would allow for the use of a much wider range of substrate thicknesses as well as enabling variations in the laser wavelength and power in order to further optimize scribing on different substrates.

### 9.1.5 Batteries

Although supercapacitors are a very promising technology, traditional batteries (electrochemical cells) will have an increasingly important role to play in energy storage for the foreseeable future.<sup>31–33</sup> Current high-performance batteries, which are mainly lithium-based, present many safety and toxicity concerns, especially upon their failure.<sup>34–37</sup> Early generations of lithium batteries were known to explode upon failure, while current lithium-ion cells may outgas toxic vapors upon overheating.<sup>37</sup> This suggests that lithium-based batteries are ideal candidates for ionogel electrolytes, as ILs are not flammable and they are thermally stable to relatively high limits.

Many researchers have published works concerning ionogels incorporating lithium ions, and the use of such materials in test electrochemical cells.<sup>38–45</sup> The main drawback of using ILs in combination with lithium ions is that the presence of the lithium ions tends to increase the viscosity of the solution rather sharply, leading to a decline in ionic conductivity.<sup>46–48</sup> However, it has been shown that the use of silica support materials can enhance lithium conductivity in IL-based electrolytes, due to the affinity between the IL and the silica surface.<sup>45</sup> As such, ionogels created through sol-gel may be particularly intriguing candidates for use in battery applications.

Initial efforts with PDMS-supported ionogels were mentioned in Chapter 8, where a 0.1 M Li<sup>+</sup>-in-EMI TCB PDMS-supported ionogel was described. 1 M Li<sup>+</sup>-in-EMI TFSI PDMS-supported ionogels have also been fabricated, with ionic conductivities of 0.6 mS/cm. A higher Li<sup>+</sup> molarity is achievable in EMI TFSI as

LiTFSI is more soluble in EMI TFSI than in EMI TCB. The next step is to test the lithium transference number of these ionogels using a simple, symmetric cell with metallic lithium electrodes. Such testing must take place in a dry, inert atmosphere. The incorporation of lithium ions into silica-supported ionogels created through sol-gel can also be investigated.

## **9.2 Final Conclusions**

Ionic liquids are a truly unique class of materials, with a staggering variety of forms and possible uses. Electrochemical energy storage is only one of these potential applications, but it is a crucial one given society's strong need for improvements in energy storage and the energy system as a whole. The use of ionic liquids in a gel form may enable the creation of high-performance electrochemical energy storage devices without the safety concerns presented by the current state of the art.

Sol-gel chemistry is a promising path towards the creation of industrially-relevant ionogels. Many industrial-scale processes already exist that use sol-gel chemistries, as solution processability is a great advantage in scale-up. This work has explored many of the questions associated with the use of sol-gel for the creation of ionogels. First, it has demonstrated that a simple, one-pot chemistry can lead to a wide variety of ionogels, with large ranges in gelation time, scaffold content, scaffold morphology, and mechanical characteristics. Within this range lie compliant ionogels, which have a soft and deformable mechanical character and were demonstrated here for the first time.

In addition to the impact of formulation changes, this work has illuminated the influence of the IL itself on the sol-gel process. It has been clearly shown that the apparent acidity of FA-in-IL solutions changes based on the IL, and that moreover the scaffold morphology can take on widely different forms when sol-gel reactions are conducted in different ILs. Therefore, the identity of the IL must be taken into account when designing a formulation for a specific application. The technique used to probe the dependence of acidity on IL identity, FTIR-based titration using pyridine, was developed in the course of this work, but may be of use to researchers working in a variety of IL-related fields.

The use of silica-supported ionogels in devices has also been explored. For the first time, the dynamics of the sol-gel process and the impact thereof on device performance has been investigated, resulting in the observation that ionogel casting time is of paramount importance for device performance when using porous, HSA electrodes. It has been clearly shown that delayed casting leads to superior device performance, with performance metrics comparable to that of devices made with neat IL, as compared to devices made with ionogels cast immediately after mixing. Moreover, the post-service fate of silica-supported ionogels has been considered, and a simple recycling process designed to reclaim ILs for further reuse. This recycling process, which is based on a spontaneous water-driven separation, may allow for future investigations providing insight into the IL/scaffold surface interactions for a variety of ionogel systems.

Finally, it has been shown that sol-gel chemistry can be used to create scaffold materials other than silica in ionogel applications. PDMS-supported ionogels with



high IL loadings were demonstrated for the first time. This result opens the door to a significant expansion in the possible scaffolds available for ionogel fabrication, including new organic/inorganic hybrids and other silicone-type structures. Moreover, it demonstrates the robustness of the sol-gel approach when combined with ILs to create ionogels.

The work presented here has shown conclusively that sol-gel chemistry is well-suited for the creation of ionogels. The preceding investigations offer observations of theoretical interest that may be used to deepen the understanding of ILs and ionogels in general. Moreover, they contain results of practical importance, which further the goal of developing ionogels for energy storage applications. In sum, these results build a strong base for continued research into the use of sol-gel in combination with ILs for the purposes of electrochemical energy storage.

### 9.3 References

1. Mackenzie, J. D. Structures and properties of Ormosils. *J. Sol-Gel Sci. Technol.* **2**, 81–86 (1994).
2. Mackenzie, J. D., Chung, Y. J. & Hu, Y. Rubbery ormosils and their applications. *J. Non-Cryst. Solids* **147-148**, 271–279 (1992).
3. Wen, J. & Wilkes, G. L. Organic/Inorganic Hybrid Network Materials by the Sol–Gel Approach. *Chem. Mater.* **8**, 1667–1681 (1996).
4. Schubert, U., Huesing, N. & Lorenz, A. Hybrid Inorganic–Organic Materials by Sol-Gel Processing of Organofunctional Metal Alkoxides. *Chem. Mater.* **7**, 2010–2027 (1995).
5. Wang, D. & Bierwagen, G. P. Sol–gel coatings on metals for corrosion protection. *Prog. Org. Coat.* **64**, 327–338 (2009).
6. Shirtcliffe, N. J., McHale, G., Newton, M. I. & Perry, C. C. Intrinsically Superhydrophobic Organosilica Sol–Gel Foams. *Langmuir* **19**, 5626–5631 (2003).
7. Morikawa, A., Iyoku, Y., Kakimoto, M.-A. & Imai, Y. Preparation of new polyimide-silica hybrid materials via the sol-gel process. *J. Mater. Chem.* **2**, 679 (1992).
8. Philipp, G. & Schmidt, H. New materials for contact lenses prepared from Si- and Ti-alkoxides by the sol-gel process. *J. Non-Cryst. Solids* **63**, 283–292 (1984).
9. Sharp, K. G. Inorganic/Organic Hybrid Materials. *Adv. Mater.* **10**, 1243–1248 (1998).

10. Qian, J. *et al.* Polypropylene wax (PPw)/silica hybrid by in situ non-aqueous sol–gel process for preparation of PP/silica nanocomposites. *J. Sol-Gel Sci. Technol.* **56**, 300–309 (2010).
11. Hu, L., Zhang, X., Sun, Y. & Williams, R. J. J. Hardness and Elastic Modulus Profiles of Hybrid Coatings. *J. Sol-Gel Sci. Technol.* **34**, 41–46 (2005).
12. Wang, F. *et al.* Effects of dimethyldiethoxysilane addition on the sol–gel process of tetraethylorthosilicate. *J. Non-Cryst. Solids* **353**, 321–326 (2007).
13. Mah, S. K. & Chung, I. J. Effects of dimethyldiethoxysilane addition on tetraethylorthosilicate sol-gel process. *J. Non-Cryst. Solids* **183**, 252–259 (1995).
14. Sakka, S., Tanaka, Y. & Kokubo, T. Hydrolysis and polycondensation of dimethyldiethoxysilane and methyltriethoxysilane as materials for the sol-gel process. *J. Non-Cryst. Solids* **82**, 24–30 (1986).
15. Hegde, N. D. & Venkateswara Rao, A. Physical properties of methyltrimethoxysilane based elastic silica aerogels prepared by the two-stage sol–gel process. *J. Mater. Sci.* **42**, 6965–6971 (2007).
16. Venkateswara Rao, A., Bhagat, S. D., Hirashima, H. & Pajonk, G. M. Synthesis of flexible silica aerogels using methyltrimethoxysilane (MTMS) precursor. *J. Colloid Interface Sci.* **300**, 279–285 (2006).
17. Venkateswara Rao, A., Lathe, S. S., Nadargi, D. Y., Hirashima, H. & Ganesan, V. Preparation of MTMS based transparent superhydrophobic silica films by sol–gel method. *J. Colloid Interface Sci.* **332**, 484–490 (2009).

18. Sharp, K. G. & Michalczyk, M. J. Star gels: New hybrid network materials from polyfunctional single component precursors. *J. Sol-Gel Sci. Technol.* **8**, 541–546 (1997).
19. Oyane, A. *et al.* Sol-gel modification of silicone to induce apatite-forming ability. *Biomaterials* **20**, 79–84 (1999).
20. Babonneau, F. Hybrid siloxane-oxide materials via sol-gel processing: Structural characterization. *Polyhedron* **13**, 1123–1130 (1994).
21. Horowitz, A. I., Wang, Y. & Panzer, M. J. Reclamation and reuse of ionic liquids from silica-based ionogels using spontaneous water-driven separation. *Green Chem.* **15**, 3414–3420 (2013).
22. Camper, D., Becker, C., Koval, C. & Noble, R. Low Pressure Hydrocarbon Solubility in Room Temperature Ionic Liquids Containing Imidazolium Rings Interpreted Using Regular Solution Theory. *Ind. Eng. Chem. Res.* **44**, 1928–1933 (2005).
23. Crosthwaite, J. M., Aki, S. N. V. K., Maginn, E. J. & Brennecke, J. F. Liquid Phase Behavior of Imidazolium-Based Ionic Liquids with Alcohols. *J. Phys. Chem. B* **108**, 5113–5119 (2004).
24. Matsumoto, M., Inomoto, Y. & Kondo, K. Selective separation of aromatic hydrocarbons through supported liquid membranes based on ionic liquids. *J. Membr. Sci.* **246**, 77–81 (2005).
25. Simon, P. & Gogotsi, Y. Materials for electrochemical capacitors. *Nat. Mater.* **7**, 845–854 (2008).

26. El-Kady, M. F. & Kaner, R. B. Scalable fabrication of high-power graphene micro-supercapacitors for flexible and on-chip energy storage. *Nat. Commun.* **4**, 1475 (2013).
27. El-Kady, M. F., Strong, V., Dubin, S. & Kaner, R. B. Laser Scribing of High-Performance and Flexible Graphene-Based Electrochemical Capacitors. *Science* **335**, 1326–1330 (2012).
28. Strong, V. *et al.* Patterning and Electronic Tuning of Laser Scribed Graphene for Flexible All-Carbon Devices. *ACS Nano* **6**, 1395–1403 (2012).
29. Zhou, R. *et al.* High-performance supercapacitors using a nanoporous current collector made from super-aligned carbon nanotubes. *Nanotechnology* **21**, 345701 (2010).
30. Kaempgen, M., Chan, C. K., Ma, J., Cui, Y. & Gruner, G. Printable Thin Film Supercapacitors Using Single-Walled Carbon Nanotubes. *Nano Lett.* **9**, 1872–1876 (2009).
31. Whittingham, M. S. Materials Challenges Facing Electrical Energy Storage. *MRS Bull.* **33**, 411–419 (2008).
32. Dunn, B., Kamath, H. & Tarascon, J.-M. Electrical Energy Storage for the Grid: A Battery of Choices. *Science* **334**, 928–935 (2011).
33. Tarascon, J. M. & Armand, M. Issues and challenges facing rechargeable lithium batteries. *Nature* **414**, 359–367 (2001).
34. Ribière, P. *et al.* Investigation on the fire-induced hazards of Li-ion battery cells by fire calorimetry. *Energy Env. Sci* **5**, 5271–5280 (2012).

35. Larsson, F., Andersson, P., Blomqvist, P., Lorén, A. & Mellander, B.-E. Characteristics of lithium-ion batteries during fire tests. *J. Power Sources* **271**, 414–420 (2014).
36. Lu, T.-Y. *et al.* Thermal hazard evaluations of 18650 lithium-ion batteries by an adiabatic calorimeter. *J. Therm. Anal. Calorim.* **114**, 1083–1088 (2013).
37. Lisbona, D. & Snee, T. A review of hazards associated with primary lithium and lithium-ion batteries. *Process Saf. Environ. Prot.* **89**, 434–442 (2011).
38. Le Bideau, J., Viau, L. & Vioux, A. Ionogels, ionic liquid based hybrid materials. *Chem. Soc. Rev.* **40**, 907–925 (2011).
39. Vioux, A., Viau, L., Volland, S. & Le Bideau, J. Use of ionic liquids in sol-gel; ionogels and applications. *Comptes Rendus Chim.* **13**, 242–255 (2010).
40. Armand, M., Endres, F., MacFarlane, D. R., Ohno, H. & Scrosati, B. Ionic-liquid materials for the electrochemical challenges of the future. *Nat. Mater.* **8**, 621–629 (2009).
41. Ito, S., Unemoto, A., Ogawa, H., Tomai, T. & Honma, I. Application of quasi-solid-state silica nanoparticles–ionic liquid composite electrolytes to all-solid-state lithium secondary battery. *J. Power Sources* **208**, 271–275 (2012).
42. Le Bideau, J., Ducros, J.-B., Soudan, P. & Guyomard, D. Solid-State Electrode Materials with Ionic-Liquid Properties for Energy Storage: the Lithium Solid-State Ionic-Liquid Concept. *Adv. Funct. Mater.* **21**, 4073–4078 (2011).

43. Guerfi, A., Dontigny, M., Kobayashi, Y., Vijn, A. & Zaghib, K. Investigations on some electrochemical aspects of lithium-ion ionic liquid/gel polymer battery systems. *J. Solid State Electrochem.* **13**, 1003–1014 (2009).
44. Egashira, M., Todo, H., Yoshimoto, N. & Morita, M. Lithium ion conduction in ionic liquid-based gel polymer electrolyte. *J. Power Sources* **178**, 729–735 (2008).
45. Ferrari, S. *et al.* Lithium ion conducting PVdF-HFP composite gel electrolytes based on N-methoxyethyl-N-methylpyrrolidinium bis(trifluoromethanesulfonyl)-imide ionic liquid. *J. Power Sources* **195**, 559–566 (2010).
46. Hayamizu, K., Aihara, Y., Nakagawa, H., Nukuda, T. & Price, W. S. Ionic Conduction and Ion Diffusion in Binary Room-Temperature Ionic Liquids Composed of [emim][BF<sub>4</sub>] and LiBF<sub>4</sub>. *J. Phys. Chem. B* **108**, 19527–19532 (2004).
47. Frömling, T., Kunze, M., Schönhoff, M., Sundermeyer, J. & Roling, B. Enhanced Lithium Transference Numbers in Ionic Liquid Electrolytes. *J. Phys. Chem. B* **112**, 12985–12990 (2008).
48. Seki, S. *et al.* Physicochemical and Electrochemical Properties of 1-Ethyl-3-Methylimidazolium Tris (pentafluoroethyl) trifluorophosphate and 1-Ethyl-3-Methylimidazolium Tetracyanoborate. *J. Electrochem. Soc.* **159**, A967–A971 (2012).

## **Appendix A**

### **Supplementary Information Concerning Chapter 3: High-Performance, Mechanically Compliant Silica-Based Ionogels for Capacitive Energy Storage**

The three figures on the subsequent pages provide supplementary information concerning the investigation detailed in Chapter 3.



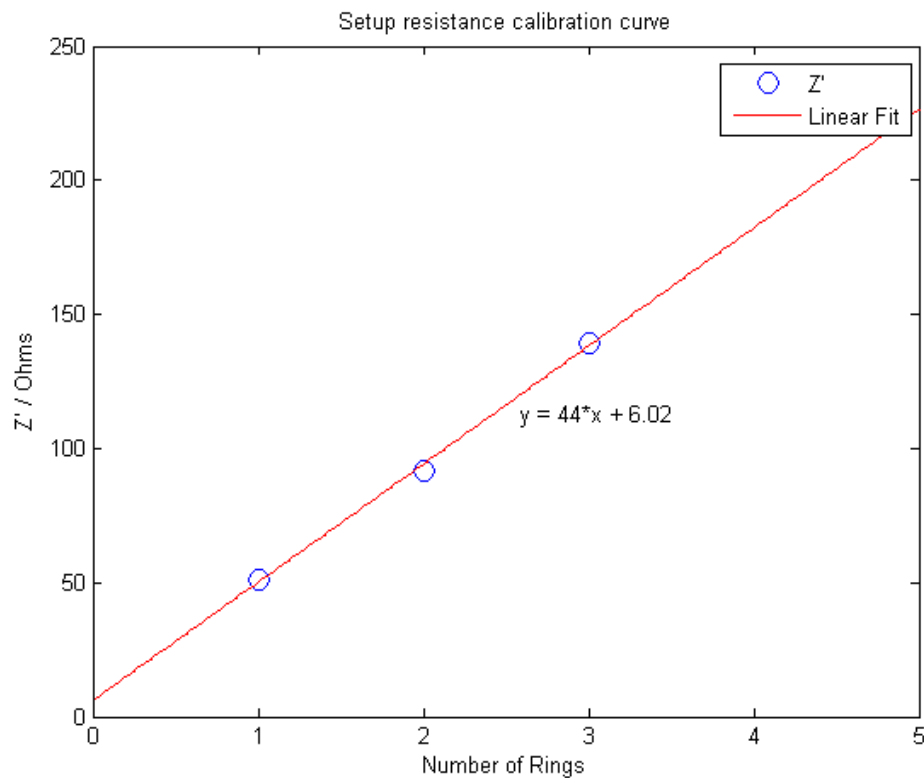


**Figure A1.** Calibration curve used to determine the intrinsic setup resistance. Impedance spectra were measured in the experimental setup using the neat IL with three different electrode spacings (molds made from 1, 2, or 3 vertically-stacked Teflon rings). The real component of the impedance ( $Z'$ ) at 100 kHz was plotted for each thickness, and a linear regression was used to extrapolate to zero IL thickness to find the setup resistance ( $\sim 6 \Omega$ ).

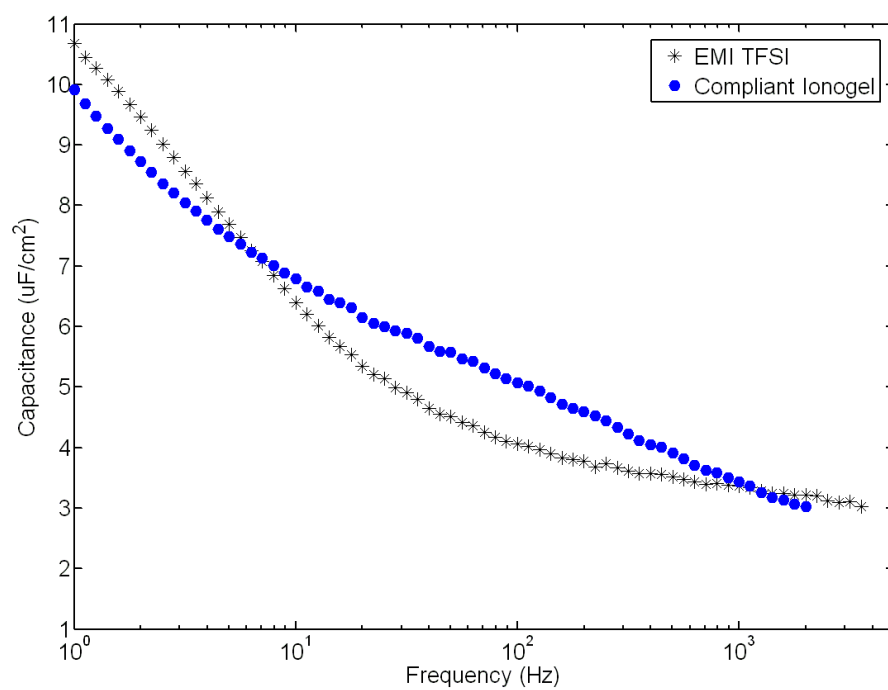


**Figure A2.** Frequency-dependent capacitance for neat EMI TFSI and compliant ionogel over frequency ranges in which capacitive behavior dominates.

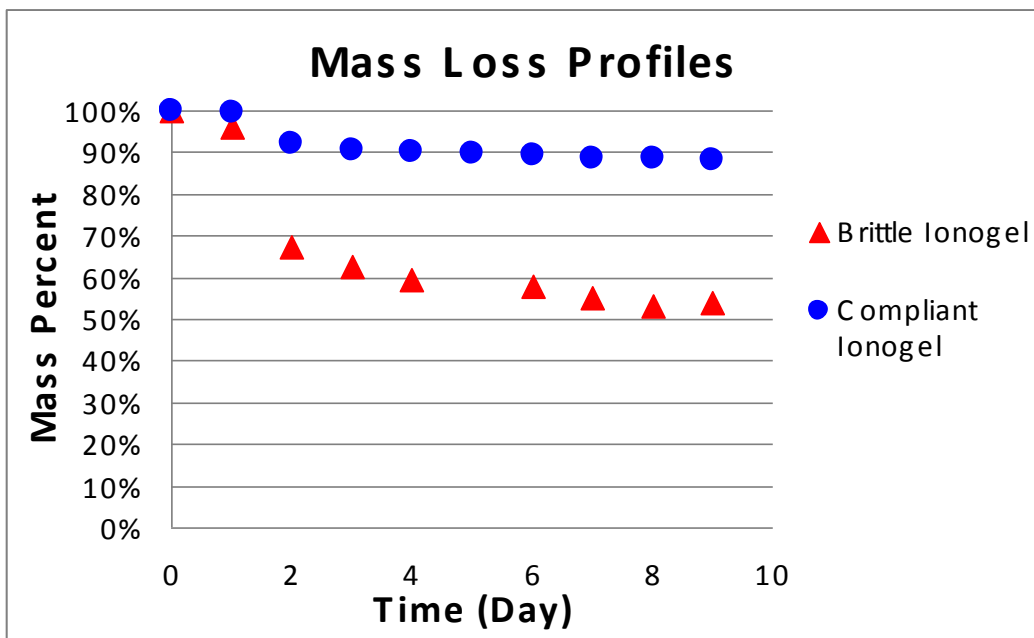


**Figure A3.** Mass loss profiles measured on bulk compliant and brittle ionogels. Compliant ionogel mass stabilizes earlier than brittle ionogel mass. Samples dried in vials, leading to a faster drying time as compared to samples injected into molds used for electrical testing due to the relatively larger open area of the vials.

## Appendix B

### Supplementary Information Concerning Chapter 5: Spectroscopic Determination of Brønsted Acid Availability as a Predictor of Relative Reactivity in Aprotic Ionic Liquids

#### B1 Supplementary Discussion Regarding Acids in Non-Aqueous Media

There is a substantial body of knowledge in the literature that concerns Brønsted acidity in non-aqueous media, dating from early in the twentieth century.<sup>1,2</sup> A number of techniques ranging from the spectroscopic<sup>3</sup> to the potentiometric<sup>4</sup> have been used to explore concepts such as the proton affinity,<sup>5</sup> tendency to donate or accept a hydrogen bond,<sup>6</sup> polarizability,<sup>7</sup> and solvent-related shifts in  $pK_a$ .<sup>8</sup>

However, these concepts have been very difficult to apply in a rigorous and useful way to IL media. Although they belong to the same class of materials, individual ILs are chemically-distinct from one another and the polarizability, proton affinity, and so forth of one IL says little about that of another IL, nor is it straightforward to compare ILs using these parameters in a way that has predictive value for reactions of interest. As discussed by Mihichuk *et al.*:<sup>9</sup>

...for many cases, a change of [conventional] solvent results in a change of  $pK_a$  that is independent of the protic molecule. This change reflects the modification of the proton's local environment. In the case of ionic liquids the situation is more complex: the acidic species is likely to be a hetero-conjugate anion derived from

the protic molecule and the solvent anion, so the change in proton environment is difficult, if not impossible, to separate out.

They later continue, “the question of acidity then is the matter of how readily the proton is available to be transferred from the base to which it is the least tightly bound.” The subject of exactly what species are present in solutions of Brønsted acids in aprotic IL media is one of present debate and active investigation.<sup>10</sup> The possible basic species available for a proton in such a solution vary widely depending on the IL and acid in question, leading to a huge number of possible equilibria.

The work of Robert *et al.*, which discusses a method for determining the Hammett acidities of acids dissolved in ILs, demonstrates the complexity inherent in attempting to apply the theories discussed above to ILs.<sup>11</sup> This work explains that the calculation of Hammett acidity for a certain acid dissolved in a certain IL was found to be dependent on the indicator used. The requirement of correcting the Hammett acidity based on the indicator used strongly suggests that the theory behind the Hammett acidity is insufficient to describe acidity in ILs as it assumes that the solvent is completely inert vis-a-vis the dissociation of the indicator.

The contribution of this work, then, is to offer a way to observe the behavior of Brønsted acids dissolved in ILs as participants in a reaction of interest. Notably, the shift undergone in acidity by the tested acids in the tested ILs is not monotonic (as evidenced by the fact that the ordering of acid availability is reversed for formic vs. nitric acid). This strongly suggests that a single set of IL-specific solvent parameters is insufficient to describe the behavior of acids in

general in solution in that IL. In addition, our method can be easily used to compare *the same acid* in *different ionic liquids* whereas previous studies are mainly concerned either with inherent IL properties or with *different acids* in the *same ionic liquid*. We describe it here with the hope that it may be used by experimentalists as a straightforward and facile screening tool, as well as by theorists as a way to further investigate crucial questions of the behavior of acids in IL-based solutions.

**Table B1.** Room temperature density, viscosity, and water content values of the ILs used in this investigation.<sup>12</sup>

Cation	Anion	Density (g/mL)	Viscosity (mPa-s)	Water Content (ppm)
EMI	TFSI	1.53	28	740
BMP	TFSI	1.4	73	306
EMI	FAP	1.71	60	249

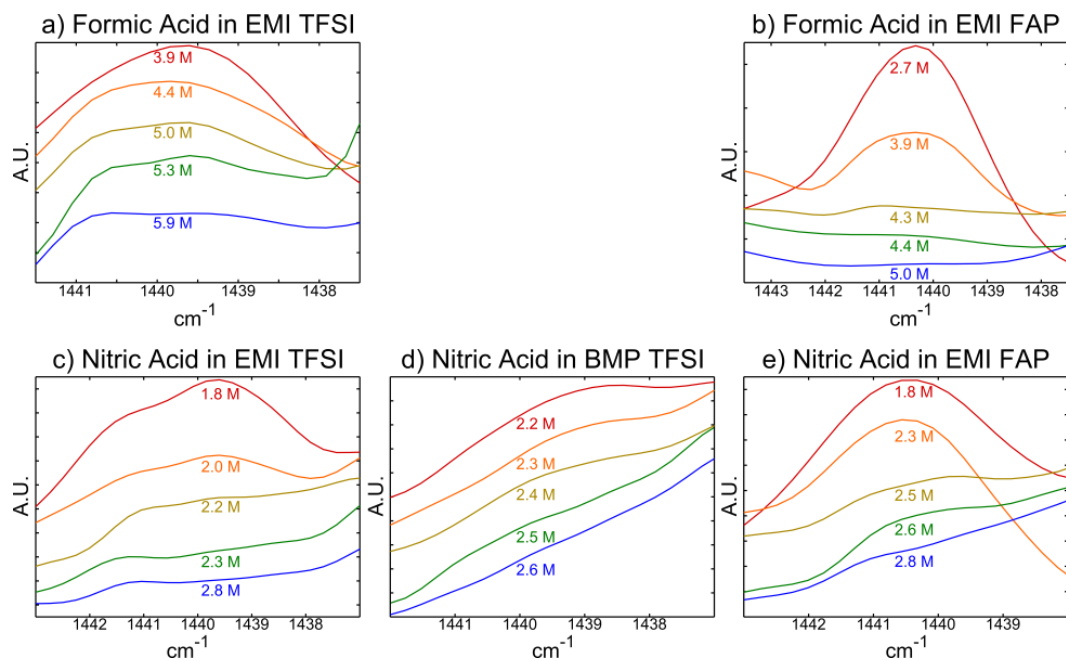


**Figure B1.** FTIR titration spectra for formic acid and nitric acid in the remaining ILs, showing the disappearance of the free pyridine peak.



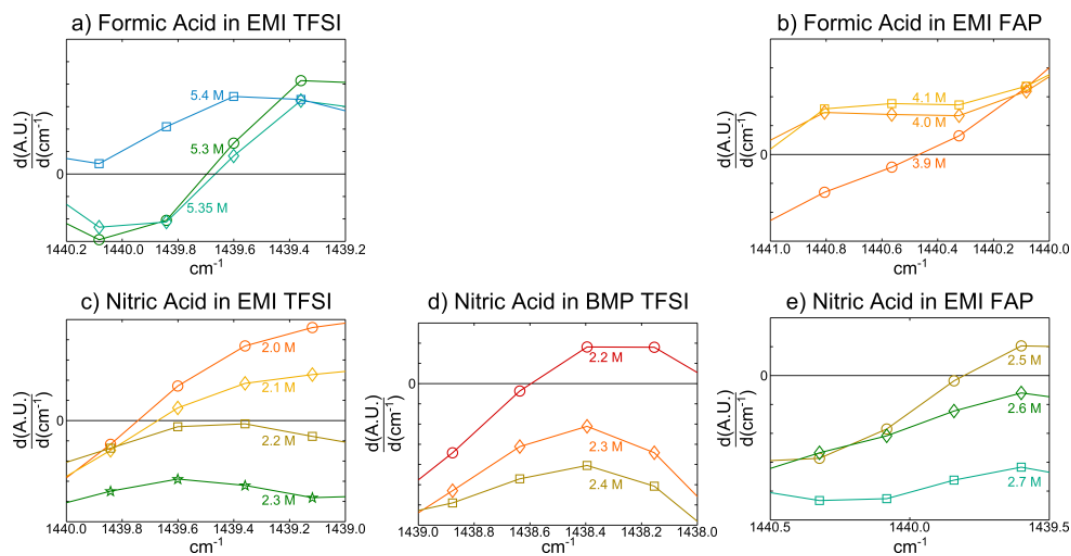


**Figure B2.** Numerical derivatives of the FTIR titration spectra for formic acid and nitric acid in the remaining ILs, showing the determination of the threshold molarities.

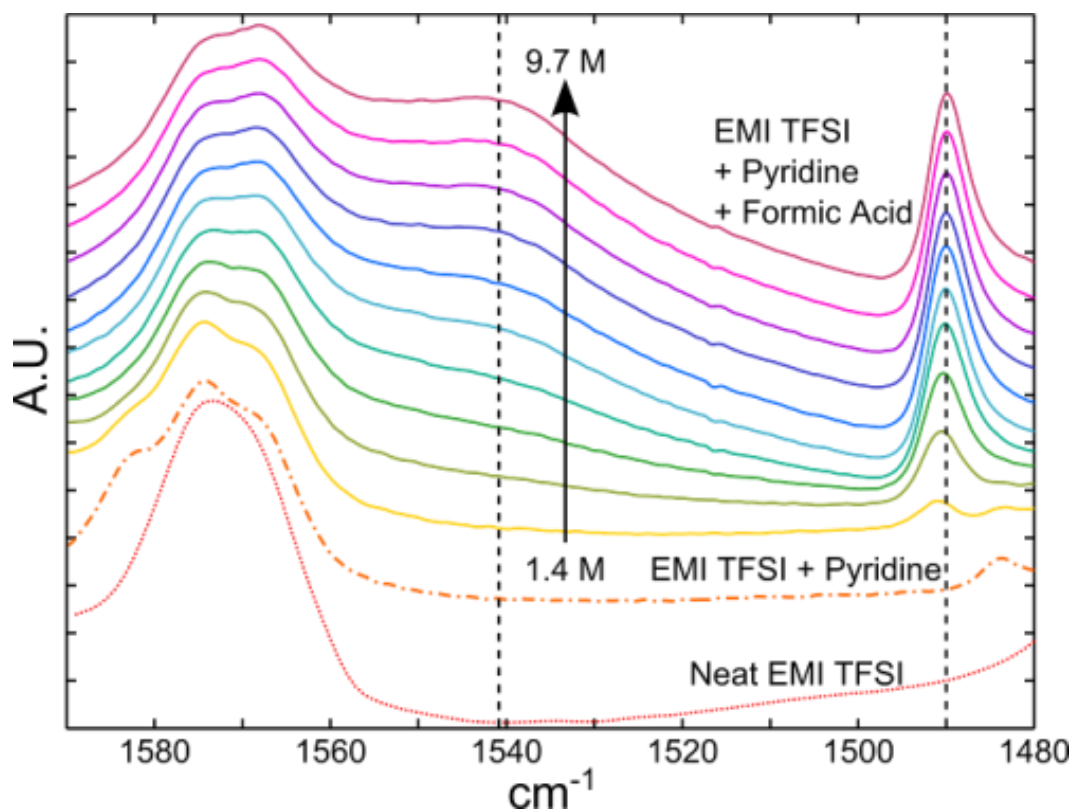


**Figure B3.** FTIR titration spectra showing the appearance of pyridinium-related peaks with increasing formic acid concentration in EMI TFSI. Spectra for neat EMI TFSI and a 1:5 (v/v) solution of pyridine in EMI TFSI are also shown for reference. The broad peak at  $1540\text{ cm}^{-1}$  (pyridinium mode  $\nu_{19b}$ ) appears as a shoulder on the EMI cation peak at  $\sim 1570\text{ cm}^{-1}$ , while the narrow peak at  $1490\text{ cm}^{-1}$  (pyridinium mode  $\nu_{19a}$ ) appears beginning at very low formic acid concentrations (first detectable at 0.6 M). As such, neither of these peaks were used for quantitative evaluations in this study. However, they do correlate with the disappearance of the free pyridine peak and may potentially be used for titrations when it is obscured by the IL signal.

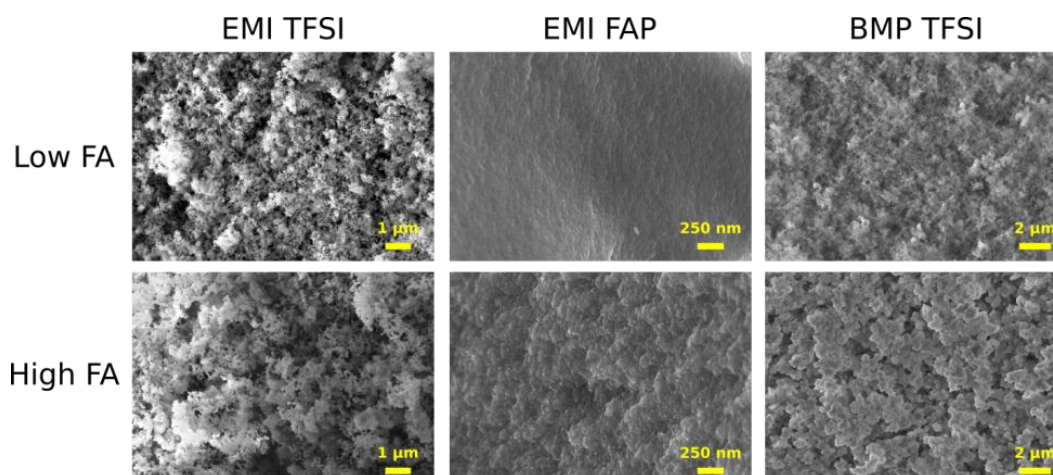


**Figure B4.** SEM images highlighting the morphologies of the silica scaffolds for ionogels created using EMI TFSI, BMP TFSI, and EMI FAP for both the high and low formic acid (FA) concentration formulations. The morphologies differ based on the identity of the IL, and especially with the identity of the anion. In all cases, the characteristic size scale of the scaffold primary particles appears to increase with increasing FA content in the reaction formulation.

## B2 References

1. Mer, V. K. la. & Downes, H. C. Acidity In Non-aqueous Solvents. Conductimetric And Electrometric Titrations Of Acids And Bases In Benzene. *J. Am. Chem. Soc.* **53**, 888–896 (1931).
2. Hammett, L. P. The Theory Of Acidity. *J. Am. Chem. Soc.* **50**, 2666–2673 (1928).
3. Reichardt, C. Solvatochromic Dyes as Solvent Polarity Indicators. *Chem. Rev.* **94**, 2319–2358 (1994).
4. Van der Heijde, H. B. & Dahmen, E. A. M. F. Potentiometric titrations in non-aqueous solution. *Anal. Chim. Acta* **16**, 378–391 (1957).
5. Popovych, O. & Bates, R. G. Estimation of Medium Effects for Single Ions in Non-Aqueous Solvents. *C R C Crit. Rev. Anal. Chem.* **1**, 73–117 (1970).
6. Kamlet, M. J. & Taft, R. W. The solvatochromic comparison method. I. The .beta.-scale of solvent hydrogen-bond acceptor (HBA) basicities. *J. Am. Chem. Soc.* **98**, 377–383 (1976).
7. Lagalante, A. F., Hall, R. L. & Bruno, T. J. Kamlet–Taft Solvatochromic Parameters of the Sub- and Supercritical Fluorinated Ethane Solvents. *J. Phys. Chem. B* **102**, 6601–6604 (1998).
8. Barrette, W. C., Johnson, H. W. & Sawyer, D. T. Voltammetric evaluation of the effective acidities (pK<sub>a</sub>') for Broensted acids in aprotic solvents. *Anal. Chem.* **56**, 1890–1898 (1984).

9. Mihichuk, L. M., Driver, G. W. & Johnson, K. E. Brønsted Acidity and the Medium: Fundamentals with a Focus on Ionic Liquids. *ChemPhysChem* **12**, 1622–1632 (2011).
10. Johnson, K. E., Pagni, R. M. & Bartmess, J. Brønsted Acids in Ionic Liquids: Fundamentals, Organic Reactions, and Comparisons. *Monatshefte Für Chem. - Chem. Mon.* **138**, 1077–1101 (2007).
11. Robert, T., Magna, L., Olivier-Bourbigou, H. & Gilbert, B. A Comparison of the Acidity Levels in Room-Temperature Ionic Liquids. *J. Electrochem. Soc.* **156**, F115 (2009).
12. Horowitz, A. I., Wang, Y. & Panzer, M. J. Reclamation and reuse of ionic liquids from silica-based ionogels using spontaneous water-driven separation. *Green Chem.* **15**, 3414–3420 (2013).

## **Appendix C**

### **Supplementary Information Concerning Chapter 7: Reclamation and Reuse of Ionic Liquids from Silica-Based Ionogels Using Spontaneous Water-Driven Separation**

The tables and derivation on the subsequent pages provide supplementary information concerning the investigation detailed in Chapter 7.

**Table C1.** Test results showing time- and temperature-dependence of IL liberation using solvents. Silica contents determined using thermogravimetric analysis (TGA). EMI TFSI-based SG-ionogels of various formulations were exposed to solvents in a ratio of 1 mL solvent to 50 mg of ionogel. At the end of the exposure period, silica solids were separated from the IL solution by vacuum filtration. No mass balance was performed on these samples.

<b>Solvent</b>	<b>Exposure Time</b>	<b>Temperature</b>	<b>Initial % Silica (S<sub>o</sub>)</b>	<b>Final % Silica (S<sub>f</sub>)</b>	<b>% Liberated</b>
EtA	1 hour	Ambient	14.0	65.4	91
EtA	2 hours	Ambient	14.0	72.0	94
EtA	1 night	Ambient	6.0	71.4	97
EtA	2 hours	80° C	9.4	82.9	98
IPA	1 night	Ambient	6.0	55.3	95
IPA	2 nights	Ambient	6.0	76.4	98

**Table C2.** Initial and final silica contents of ionogel and silica residue samples as determined by TGA.

<b>Ionogel</b>	<b>Initial % Silica (<math>S_o</math>)</b>	<b>Final % Silica (<math>S_f</math>)</b>
EMI TFSI (FS)*	6.2	38.7
EMI TFSI (SG)*	5.4	28.5
BMI TFSI (SG)	3.4	31.3
HMI TFSI (SG)	7.5	91.1
BMP TFSI (SG)	3.2	38.9
EMI FAP (SG)	6.2	49.2



### C1 Derivation of Equation 7.1

In an as-prepared gel, there are two components, the ionic liquid (of mass  $L_o$ ) and the silica scaffold (of mass  $\sigma$ ). The total mass,  $M_o$ , is the sum of  $L_o$  and  $S$ . The composition percentages are denoted

$$(C1) \quad L_o/M_o = \ell_o$$

$$(C2) \quad \sigma/M_o = S_o$$

Note that  $\ell_o + S_o = 1$ .

In the final silica material, there are also two components,  $L_f$  and  $\sigma$  — all the silica remains. The new mass is  $M_f$  and the new fractions are

$$(C3) \quad L_f/M_f = \ell_f$$

$$(C4) \quad \sigma/M_f = S_f$$

The fraction of the IL remaining is defined:

$$(C5) \quad F_R = L_f/L_o$$

We want to find the inverse of this, the fraction of the IL that has been liberated:

$$(C6) \quad F_L = 1 - F_R = 1 - L_f/L_o = \frac{L_o - L_f}{L_o}$$

Rearranging our definitions from above:

$$(C2^*) \quad \sigma = S_o M_o = S_o (L_o + \sigma)$$

$$(C1^*) \quad L_o = \sigma/S_o - \sigma$$

Similarly:

$$(C3^*) \quad L_f = \sigma/S_f - \sigma$$

$$(C5^*) \quad F_R = \frac{\sigma/S_f - \sigma}{\sigma/S_o - \sigma} = \frac{1/S_f - 1}{1/S_o - 1} = \frac{S_o - S_f S_o}{S_f - S_f S_o}$$

$$(C6^*) \quad F_L = 1 - \frac{S_o - S_f S_o}{S_f - S_f S_o} = \frac{S_f - S_f S_o - S_o + S_f S_o}{S_f - S_f S_o}$$

$$(7.1^*) \quad F_L = \frac{S_f - S_o}{S_f - S_f S_o}$$

The percent liberated (Eq. 7.1) is simply 100 times  $F_L$ .

## Appendix D

### Supporting Information Concerning Chapter 8: Poly(dimethylsiloxane)- Supported Ionogels with High Ionic Liquid Loading

#### D1 Determination of the Extent of PDMS Scaffold Crosslinking

Hexane absorption, as described above, was used to determine the extent of crosslinking in the PDMS scaffold. In the case of these ionogels, a crosslink would be located wherever at least two of the reactive end groups on one end of an f-PDMS chain were connected to other chains. Bonds may form between chains with no crosslinking if only one reactive end group per chain end forms a connection to another chain.

The molecular weight between crosslinks was calculated using the Flory-Rehner equation:<sup>1</sup>

$$(D1) \quad M_c = \frac{-\rho V_1 v_2^{1/3}}{-X v_2 + \ln(1 - v_2) + v_2}$$

where  $M_c$  is the molecular weight between crosslinks (g/mol),  $\rho$  is the density of PDMS (g/mL),  $V_1$  is the molar volume of hexane (mL/mol),  $v_2$  is the volume fraction of PDMS (discounting the presence of the IL), and  $X$  is the interaction parameter between PDMS and hexane.<sup>2</sup> Using this equation,  $M_c$  was calculated to be ~11,000 g/mol, suggesting that approximately 13 f-PDMS chains are bonded linearly between crosslinks.

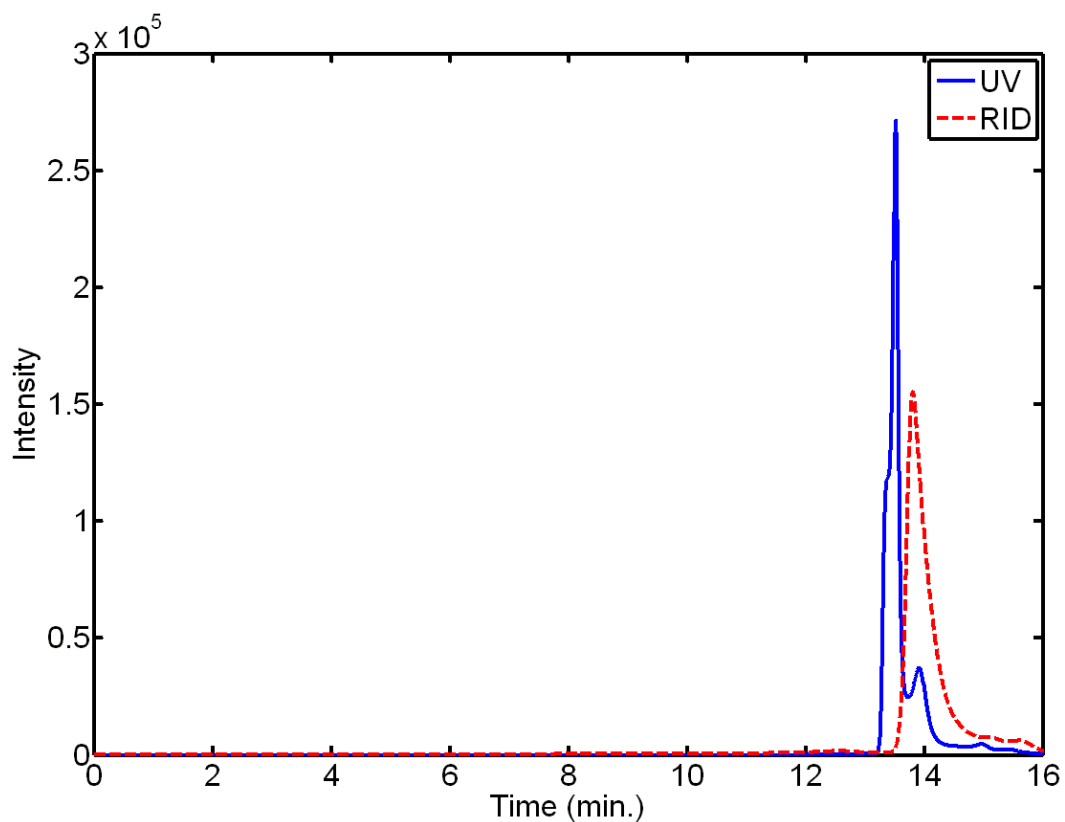


**Figure D1.** GPC spectra of the supernatant liquid from a solution in which a PDMS-supported ionogel had been submersed in THF for one week. The UV detector is positioned before the RID detector, causing the slight offset in peak positions. The main peaks correspond to a molecular weight of 213 g/mol, which is (within experimental error) equivalent to the molecular weight of EMI TCB (226 g/mol). The single main peaks indicate that only IL was liberated from the ionogel sample, suggesting that the entirety of the f-PDMS precursor was integrated into the scaffold.

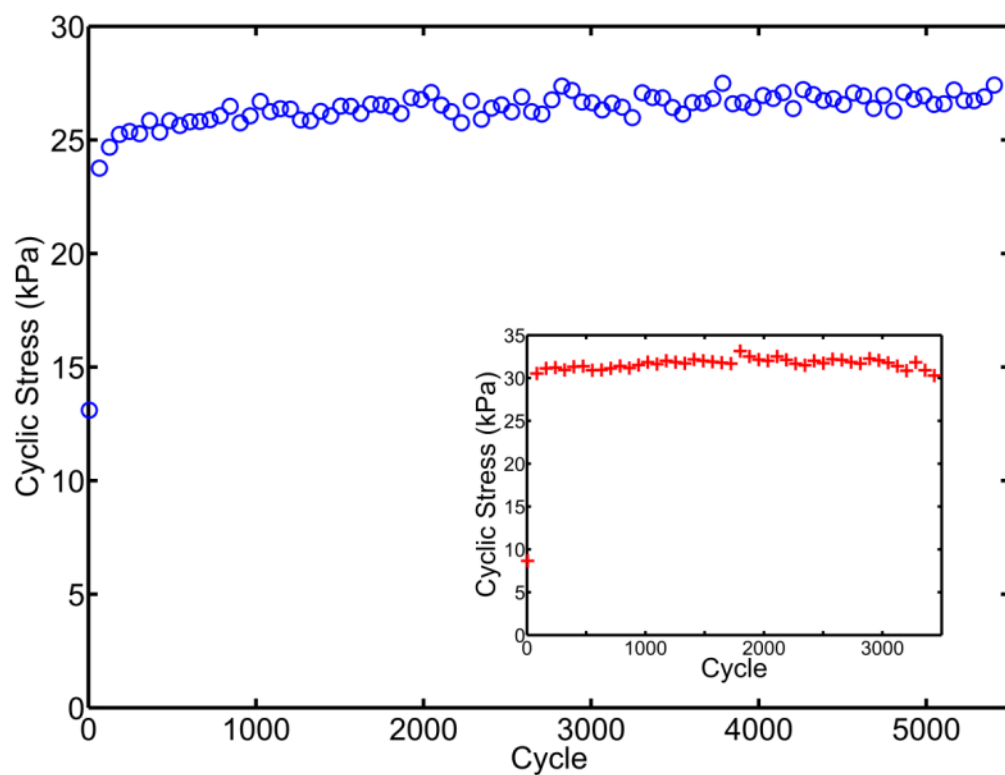


**Figure D2.** Fatigue test of PDMS-supported ionogel, demonstrating mechanical stability over more than 5000 cycles. A short burn-in period is observable. Inset shows fatigue data measured at 60 °C.

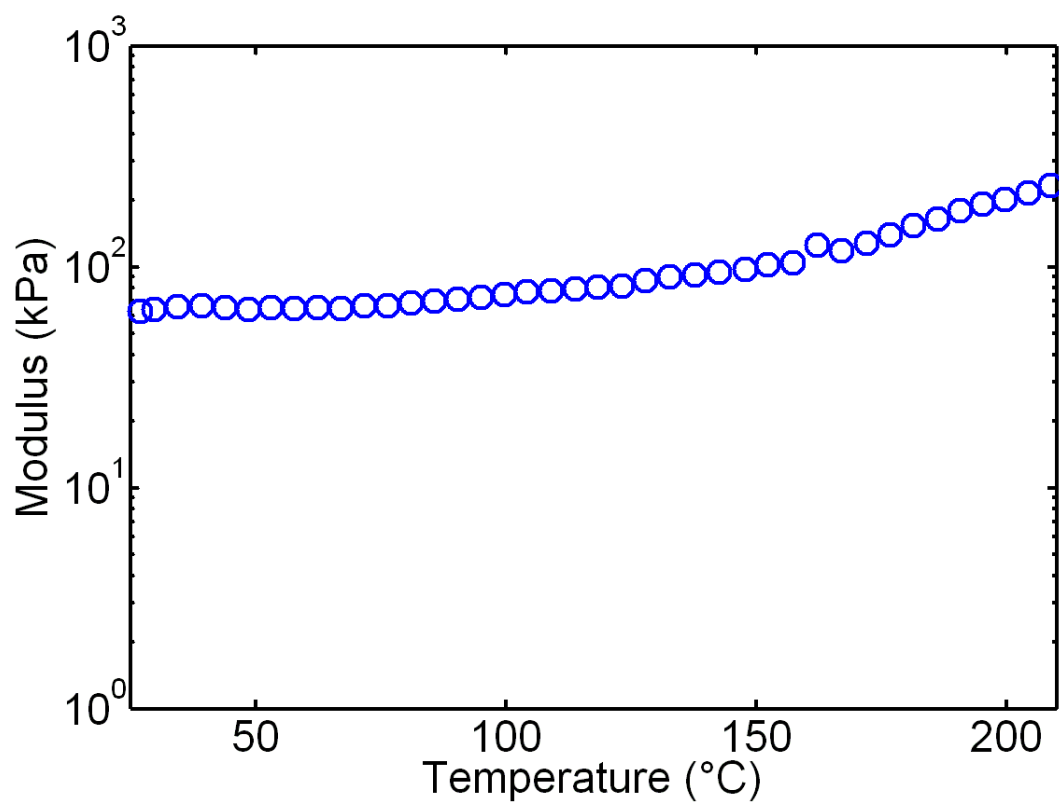


**Figure D3.** Elastic modulus vs. temperature for PDMS-supported ionogel, demonstrating mechanical stability until above 200 °C. The rise in modulus with increasing temperature is characteristic of PDMS above its glass transition temperature, but below the melting temperature.<sup>3</sup>

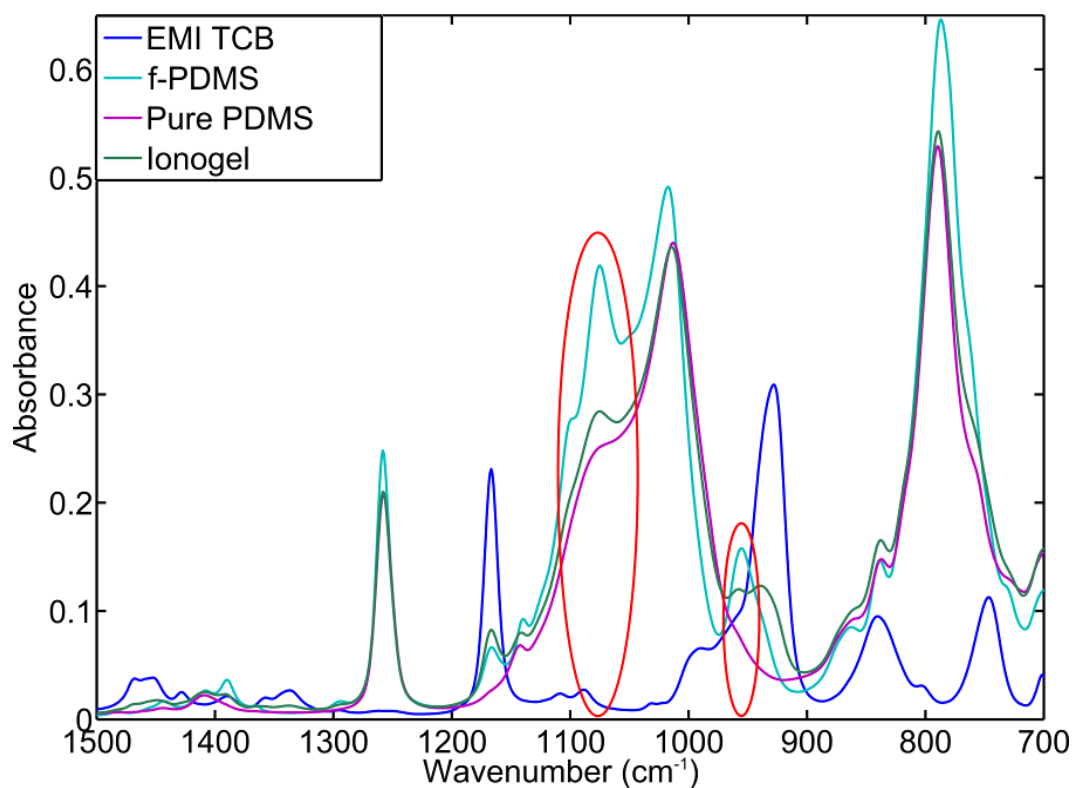


**Figure D4.** FTIR spectra of EMI TCB, the f-PDMS oligomer, crosslinked pure PDMS, and a PDMS-supported ionogel. Red circles indicate peaks that disappear or substantially decrease for the as-synthesized pure PDMS and ionogel as compared to f-PDMS. The peaks at roughly 950 and 1090  $\text{cm}^{-1}$  are identifiable as belonging to the reactive end-groups of f-PDMS.<sup>4</sup>

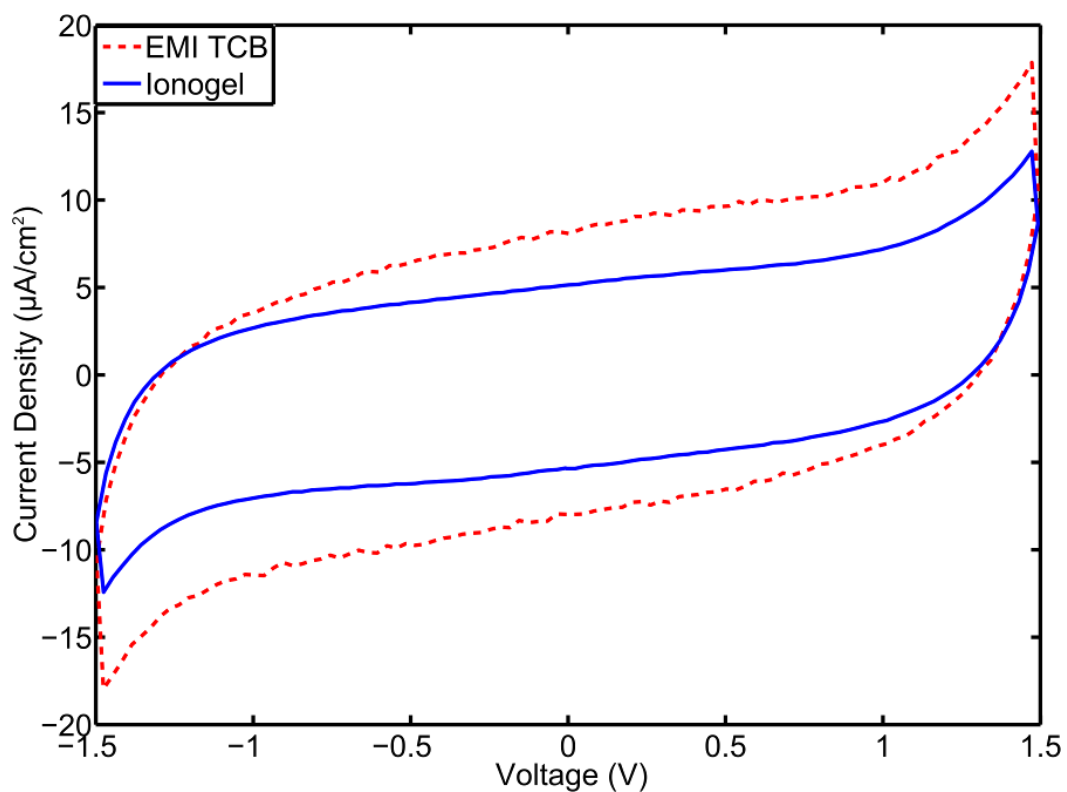


**Figure D5.** Cyclic voltammograms of a PDMS-supported ionogel and neat EMI TCB. Samples were placed between two planar glassy carbon electrodes and tested using a 0.5 V/s scan rate. The ionogel shows a largely rectangular response characteristic of capacitive behavior.



## **D2 Influence of Formulation Changes on PDMS Ionogels**

The synthetic strategy described in this work can be effectively employed to produce ionogels over a sizeable range of formulations. As the IL does not participate in the scaffold-forming reaction, altering the molar ratio of f-PDMS to FA is of the greatest interest (as described below). For all successful EMI TCB-based gels, the observed scaffold structure was similar to that shown in the main text, with minor morphological differences appearing in the average domain size of the respective IL and PDMS regions. In these investigations, all ionogel precursor solutions were stirred at ~1000 rpm for 1-2 minutes and then stirred at ~500 RPM until a resin was obtained.

Two approaches were employed to prepare ionogels with increased FA content in the reaction mixture compared to the formulation characterized in the main text. First, the total system volume and volume fraction of IL (50%) were kept constant, and the f-PDMS to FA ratio was increased from 1:13 to 1:18. This effectively decreased the amount of f-PDMS present compared to the IL, resulting in a volumetric ratio of 1:1.8 (f-PDMS:IL) as compared to 1:1.6 for the original formulation. As a result, there was an insufficient amount of f-PDMS present to fully encapsulate the IL and form a homogeneous gel. This sample exhibited a significant volume of free IL and a small volume of a heterogeneous gel (Figure D6a), containing both PDMS- and IL-rich regions. Second, the system volume was increased to both maintain the volume ratio of f-PDMS to IL at the same value as the formulation described in the main text (1:1.6) and increase the f-PDMS to FA ratio to 1:18. This new formulation did produce a homogeneous gel

with a structure similar to that of the gel described in the main text (Figure D6b), but required a longer stir time (~1 hour) before a stable resin could be formed. At first glance, this seemed counterintuitive, as increasing the amount of FA normally leads to faster reaction times. However, FA is only required in the initial phases of the reaction network (carboxylation and esterification).<sup>5</sup> In this system, a stable resin is produced only when the overall viscosity of the mixture is large enough to prevent phase separation. Additional FA volume reduces the viscosity of the mixture, effectively increasing the amount of PDMS that must be formed before the viscosity has increased sufficiently to inhibit separation of the two phases. Additionally, this relatively large volume of FA (miscible with both water and the IL) may lead to partitioning of the water generated in the initial reaction phases into the (otherwise hydrophobic) IL phase, slowing the hydrolysis phase of the reaction network.

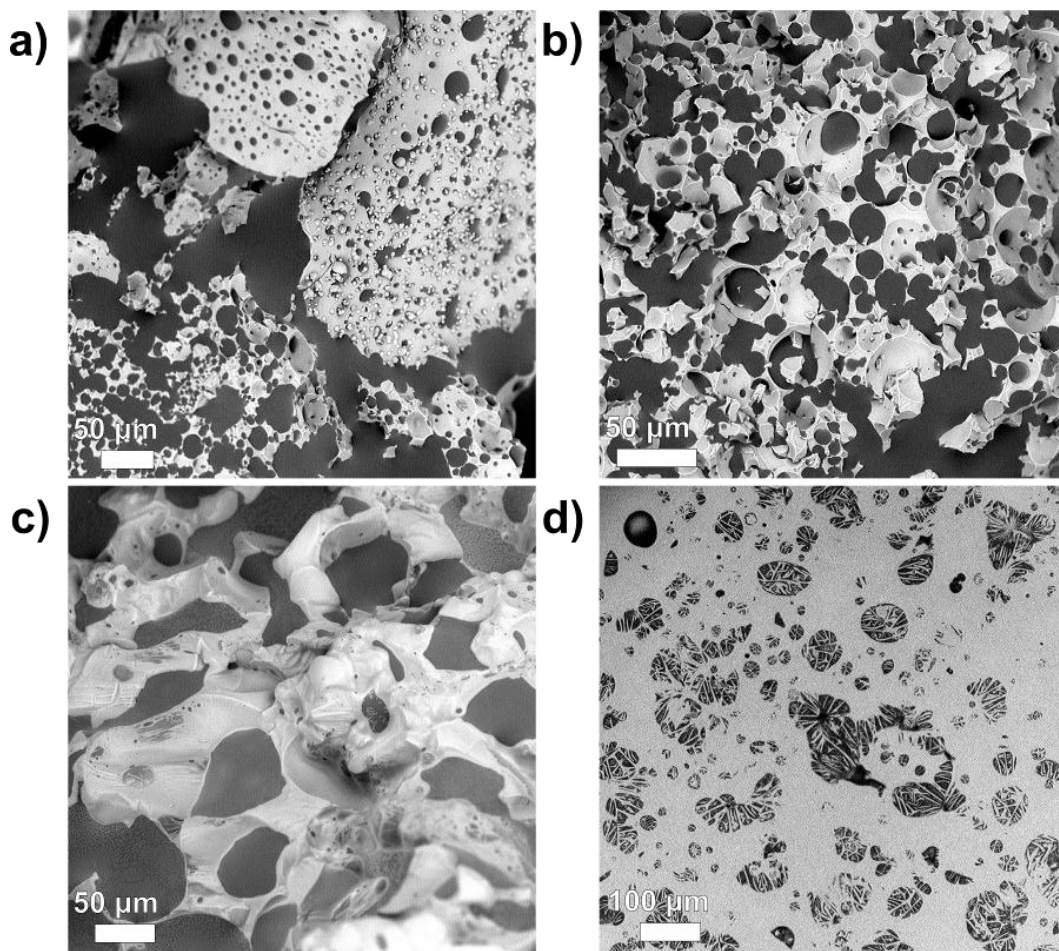


**Figure D6.** SEM images of samples made using various reactive formulations. (a) 1:18 molar ratio of f-PDMS:FA and 50% IL by volume (1:1.8 volume ratio between f-PDMS and IL). (b) 1:18 molar ratio of f-PDMS:FA and a 1:1.6 volume ratio between the f-PDMS and IL (here the mixture is 47% IL by volume). This formulation results in an ionogel with a similar structure to that described in the main text. (c) 1:9 molar ratio of f-PDMS:FA and 50% IL by volume. (d) The viscous material (not a free-standing gel) obtained using methoxy-terminated f-PDMS (only one reactive group per oligomer chain end).

Reducing the FA content is generally undesirable, as it mainly has the effect of slowing the reaction and requiring longer processing times. A formulation with a 1:9 molar ratio of f-PDMS to FA and 50% IL by volume was prepared, which required a 1.25 hour stir time before producing a resin and solidifying into an ionogel with a similar structure to that described in the main text (Figure D6c). Further reduction of the f-PDMS to FA ratio to 1:6 increased the stir time to ~6 hours, while a 1:3 ratio leads to a formulation that will not form a resin even after 24 hours.

The formulation can also be altered to increase the amount of PDMS in the final ionogel. As expected, increasing the PDMS content of ionogels increases the elastic modulus and decreases the ionic conductivity. Ionogels with 50% IL loading by weight can be prepared from a precursor solution consisting of 45% EMI TCB by volume, with a 1:6 molar ratio of f-PDMS to formic acid. The ionic conductivity of the resulting ionogel was only 0.1 mS/cm, displaying an elastic modulus of 0.5 MPa. For comparison, the elastic modulus of the as-prepared pure PDMS was 1 MPa.

Finally, ionogels were prepared using methoxy-terminated f-PDMS, with one reactive group per oligomer end. Using the synthetic strategy described here with methoxy-terminated f-PDMS produces an extremely viscous single-phase substance. With no crosslinks in the scaffold, this substance is not free-standing and cannot properly be termed a gel. A SEM image of the sample shows a flat PDMS film with encapsulated droplets of IL (Figure D6d). However, it is stable and does not phase-separate over time.

### **D3 Lithium-Containing Ionogels**

Ionic liquid-based electrolytes are of interest for lithium and lithium-ion battery applications as they may mitigate one of the major safety concerns posed by traditional electrolytes, namely volatility/flammability.<sup>6,7</sup> Computational studies have shown that tetracyanoborate-based ILs are of particular interest for these applications, since the TCB anion only weakly coordinates the lithium cation, leading to a higher concentration of active charge carriers.<sup>8,9</sup> As described above, ionogels containing lithium ions dissolved in EMI TCB have been achieved using the synthetic strategy introduced in this work. The ionic conductivity of these ionogels is 2.2 mS/cm at room temperature, as measured using EIS. This value is lower than the conductivity of ionogels containing only EMI TCB due to the well-known increase in viscosity of  $\text{Li}^+$ -in-IL solutions as compared to neat ILs.<sup>7,10</sup> This increase in viscosity leads to a decrease in ionic conductivity. However, the conductivity of  $\text{Li}^+$ -containing PDMS-supported ionogels synthesized here remains above the 1 mS/cm benchmark desired for electrochemical devices<sup>11</sup> and is expected to improve with further optimization.

#### D4 References


1. Flory, P. J. & Rehner, J. Statistical Mechanics of Cross-Linked Polymer Networks II. Swelling. *J. Chem. Phys.* **11**, 521 (1943).
2. Mark, J. E. *Physical properties of polymer handbook*. (Springer, 2006).
3. Lötters, J. C., Olthuis, W., Veltink, P. H. & Bergveld, P. The mechanical properties of the rubber elastic polymer polydimethylsiloxane for sensor applications. *J. Micromechanics Microengineering* **7**, 145–147 (1997).
4. Launer, P. J. Infrared analysis of organosilicon compounds: spectra-structure correlations. *Silicone Compd. Regist. Rev.* 100–103 (1987).
5. Sharp, K. G. A two-component, non-aqueous route to silica gel. *J. Sol-Gel Sci. Technol.* **2**, 35–41 (1994).
6. Lewandowski, A. & Świdarska-Mocek, A. Ionic liquids as electrolytes for Li-ion batteries—An overview of electrochemical studies. *J. Power Sources* **194**, 601–609 (2009).
7. Le Bideau, J., Viau, L. & Vioux, A. Ionogels, ionic liquid based hybrid materials. *Chem. Soc. Rev.* **40**, 907–925 (2011).
8. Scheers, J., Johansson, P. & Jacobsson, P. Anions for Lithium Battery Electrolytes: A Spectroscopic and Theoretical Study of the  $\text{B}(\text{CN})_4^-$  Anion of the Ionic Liquid  $\text{C}_2\text{mimB}(\text{CN})_4$ . *J. Electrochem. Soc.* **155**, A628 (2008).
9. Angenendt, K. & Johansson, P. Ionic Liquid Based Lithium Battery Electrolytes: Charge Carriers and Interactions Derived by Density Functional Theory Calculations. *J. Phys. Chem. B* **115**, 7808–7813 (2011).


10. Garcia, B., Lavallée, S., Perron, G., Michot, C. & Armand, M. Room temperature molten salts as lithium battery electrolyte. *Electrochimica Acta* **49**, 4583–4588 (2004).
11. Schulze, M. W., McIntosh, L. D., Hillmyer, M. A. & Lodge, T. P. High-Modulus, High-Conductivity Nanostructured Polymer Electrolyte Membranes via Polymerization-Induced Phase Separation. *Nano Lett.* **14**, 122–126 (2014).

## Appendix E: How to Capture Stress/Strain Data with the DMA

- 1) Prepare samples.

Appropriate samples should be approximately 0.25"/6.35 mm in diameter (for an area of 0.316 cm<sup>2</sup>) and 0.125"/3.175 mm thick. This enables the instrument to capture accurate data.


- 2) Load the smallest "parallel plate" attachments onto the instrument. Start the instrument software and turn on the motor (). Place your sample on the bottom stage, making sure it's centered. These steps should be covered in the general instrument training.

- 3) Making sure that the gap between the top and bottom stage is larger than the height of the sample using the Gap/Instrument Control window () and set the force to zero (Figure E1). It may sometimes be necessary to re-zero the stage height as well; you will have to do this if the stage gap at the end of the next step reads a value significantly different than your sample thickness from step 1.



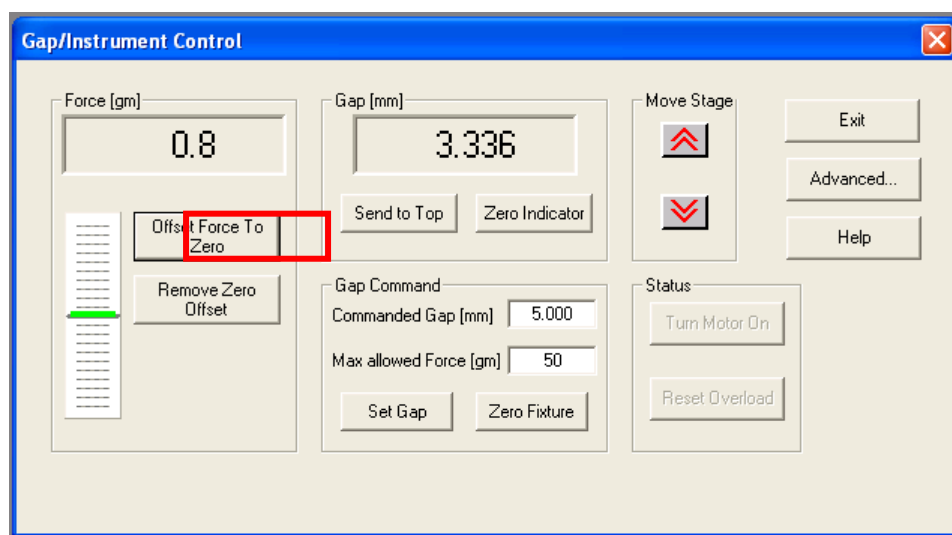


**Figure E1.** The Gap/Instrument Control window.

- 4) Bring the top stage down until it is almost in contact with the sample, using the stage control window (Figure E1). Then, SLOWLY bring the top stage into gentle contact with the sample. Apply a preload of 1 gram of force to ensure the top stage is in contact with the sample. (It may be necessary to reduce the preload for very soft samples.)
- 5) Setup the test () using the Edit/Start Instrument Test window (Figure E2). Enter a desired filename (title/folder), making sure you're saving data in your directory.

**Edit / Start Instrument Test**

Experiment

Title: 60mb 0% #1 Save As

Folder: \\tsclient\c\Users\RSALIII\Desktop\Joe B\Glycerol Foams\ -20C Slow 9-23\9 Edit Notes

Operator: Administrator ☒ AutoSave Experiment at end of test

Test Notes:

Sample Geometry

☒ Predefined Geometries ☐ Stored Geometries Browse

Geometry: [Tens Cyl] Cylindrical Tension/Compression Geometry Edit Geometry

Test Setup

☒ Predefined Test Setups ☐ Stored Test Setups Browse

Test Setup: [MultiExt] Multiple Extension Mode Test Edit Test

Test Type: ☒ Strain-Controlled

Measurement Type: ☐ Dynamic ☒ Transient

Begin Test Help Exit

**Figure E2.** The Edit/Start Instrument Test window.

6) Set the sample geometry.

In general: select “[Tens Cyln] Cylindrical Tension/Compression Geometry”, and then press the “Edit Geometry” button. Enter the area of your sample in the appropriate units and make sure the “read test fixture gap at beginning of test” option is selected.

If you are running a large number of samples with the same area, you can store this and then use the “Stored Geometries” option.

7) Select the test.

Stress/strain data is captured using the “[MultiExt] Multiple Extension Mode Test”, which is a strain-controlled, transient test. This test will not appear as an option if you have “Dynamic” selected as the measurement type.

8) Setup and run the test.

Press the “Edit Test” button in the Edit/Start Instrument Test window. This will bring you to the test options window (Figure E3). You do not need to change the temperature if the instrument is setup correctly (i.e., temperature/environmental control is off). For good data resolution, maintain the Points Per Zone at 350.

In order to subject the sample to one load/unload cycle:

- a) Make sure the Extension Mode is set to “Rate [mm/s]”.

- b) Set the Extension Value to -0.015 for Zone 1 and 0.015 for Zone 2. This will bring the upper stage downwards at a rate of 0.015 mm/s (loading) and then upwards at the same rate (unloading). This strain rate may need to be adjusted for very soft or very hard samples.
- c) Decide on a desired strain; 30% is a common value for our sample.
- d) Calculate the zone time necessary as  $(\text{strain} \times \text{sample thickness}) / \text{extension rate}$ . The zone time should be the same for Zones 1 and 2.
- e) In order to apply a second load/unload cycle, fill in the appropriate values for Zones 3 and 4. Using a longer zone time for these steps will produce an increased strain for the second cycle.
- f) Once the test is setup, click Ok and then Begin Test.

**Multiple Extension Mode Test** [?] [X]

Temperature ..... 28.0 [°C] Max=600.0°C Min=-155.0°C  
 Points Per Zone 350 [ ] Max=350 Min=20

Zone Number	1	2	3	4
Zone Time ..... [s or h:m:s]	112	112	0	0
Extension Value [See Mode for Units]	-0.0167	0.0167	0.0	0.0
Extension Mode .....	Rate [mm/s]	Rate [mm/s]	Rate [mm/s]	Rate [mm/s]

Options: Delay:Off RateGain:Off

Ok Options End of Test Save As Help Cancel

**Figure E3.** The multiple extension mode test options window.